Fall 2021

Characterization of UAV-based Wireless Channels With Diverse Antenna Configurations

Mahmoud Badi
Southern Methodist University, mbadi@smu.edu

CHARACTERIZATION OF UAV-BASED WIRELESS CHANNELS WITH DIVERSE ANTENNA CONFIGURATIONS

Approved by:

Joseph Camp
Electrical and Computer Engineering
Dissertation Committee Chairperson

Dinesh Rajan
Electrical and Computer Engineering

Mitchel Thornton
Electrical and Computer Engineering

Jennifer Dworak
Electrical and Computer Engineering

Eric Larson
Computer Science

CHARACTERIZATION OF UAV-BASED WIRELESS CHANNELS WITH DIVERSE ANTENNA CONFIGURATIONS

A Dissertation Presented to the Graduate Faculty of the

Lyle School of Engineering

Southern Methodist University

in

Partial Fulfillment of the Requirements

for the degree of

Doctor of Philosophy

with a

Major in Electrical and Computer Engineering

by

Mahmoud Badi

M.S., Telecommunications and Network Engineering, Southern Methodist University, 2017
B.S., Electrical and Electronic Engineering, University of Tripoli, 2012

December 18, 2021

ACKNOWLEDGMENTS

First, my infinite gratitude goes to my wife, Areej. It is only due to her limitless and constant support I was able to venture on this long journey and accomplish this work.

Second, I would like to thank Dr. Joseph Camp, to whom I owe a lot, for his guidance and unwavering support. Dr. Camp provided me with the support needed to professionally grow, provide for my family, and reshape the way I think of problems and execute research. His impact on my personal and professional life will never fade. Furthermore, Dr. Dinesh Rajan was key in my growth as a researcher. Having been co-advised by him is a priceless merit of being a member of our research group. His feedback and advice have always been crucial to my professional development and preparedness for the future.

Third, I would like to thank my family (mother, father and sisters) who I haven't seen in more than four years, for their encouragement, understanding, and putting up with my being away. I miss them immensely and it is a relief knowing that I will see them soon.

Fourth, I would like to express my gratitude to my colleagues who helped me in accomplishing this work. My appreciation goes to Cameron Matson for collaborating with me in the work presented in Chapter 5, Sabya Gupta for contributing to the work discussed in Chapter 4, and John Wensowitch for helping me with the work presented in Chapter 3.

I'm also extremely grateful for my friends, especially Mahdi Heidarizad and Mamdouh Mubarak who helped me get through a lot throughout this journey. They were (and still are) the brothers I never had. My appreciation also goes to my colleagues Yan Shi, Rita Enami, and Yazeed Alkhrijah for our fun and productive conversations.

Last but not least, I would like to thank Dr. Mitchell Thornton, Dr. Eric Larson, and Dr. Jennifer Dworak for being in my committee and providing me with insightful feedback and comments that helped in improving my work.

This work was supported in part by the NSF via grants CNS-1823304 and CNS-1909381 and in part by the Air Force Office of Scientific Research via grant FA9550-19-1-0375.

Badi, Mahmoud M.S., Telecommunications and Network Engineering, Southern Methodist University, 2017
B.S., Electrical and Electronic Engineering, University of Tripoli, 2012

Characterization of UAV-based Wireless Channels With Diverse Antenna Configurations

Advisor: Joseph Camp

Doctor of Philosophy conferred December 18, 2021

Dissertation completed November 15, 2021

In the next wave of swarm-based applications, unmanned aerial vehicles (UAVs) need to communicate with peer drones in any direction of a three-dimensional (3D) space. On a given drone and across drones, various antenna positions and orientations are possible. We know that, in free space, high levels of signal loss are expected if the transmitting and receiving antennas are cross polarized. However, increasing the reflective and scattering objects in the channel between a transmitter and receiver can cause the received polarization to become completely independent from the transmitted polarization, making the cross-polarization of antennas insignificant. Usually, these effects are studied in the context of cellular and terrestrial networks and have not been analyzed when those objects are the actual bodies of the communicating drones that can take different relative directions or move at various elevations. In this work, we show that the body of the drone can affect the received power across various antenna orientations and positions and act as a local scatterer that increases channel depolarization, reducing the cross-polarization discrimination (XPD).

In addition to communicating with other UAVs in a swarm, UAVs can also serve users on the ground. For example, at ultra-low altitudes, an unmanned aerial vehicle (UAV) can act as a personal base station where it communicates only with one or two users on the ground. The communication device used by a user can be in their pocket, held by hand, or attached to their bodies. In these scenarios, the wireless channel can go through different fading levels, depending on the UAV's location, user orientation, the location of the UE near the

user's body, and the frequency of the transmitted signal. The extent to which these factors can affect Air-to-Ground channels at ultra-low altitudes is studied in this work. We answer questions regarding how the human body and different use-cases of holding a communication device on the ground can affect the quality of the wireless channel and the optimal UAV hovering location. Furthermore, we demonstrate how the observed effects can be leveraged to our advantage and increase the physical layer security of UAV-assisted networks relying on the human-induced effects.

Finally, in situations where a UAV swarm needs to communicate with a target that is far or surrounded by undesired receivers, beamforming can be an attractive solution. With beamforming, the transmitted signal becomes shaped towards a certain direction confining its spatial signature and increasing the received signal-to-noise-ratio (SNR) at the receiver. However, phase synchronization across the swarm is difficult to achieve and there will always exist some degree of phase incoherency across the transmitted signals from the distributed UAVs. Phase differences between the distributed nodes would result in signals arriving at different times and their phases might not align with each other resulting in reductions in beamforming gain. Hence, a method to increase phase coherency at the receiver with limited channel overhead is desired. To this end, we propose a UAV rotation-based method through which the UAV, relying on its heterogeneous body structure, can alter the phase of the incoming signals and increase the beamformed signal level.

TABLE OF CONTENTS

LIST OF FIGURES

LIST OF TABLES

This work is dedicated to my family.

Chapter 1

Introduction

Due to many attractive features, such as low cost, ease of on-demand deployment, and ability to maintain position or move in any direction, investment in unmanned aerial vehicles (UAVs) has surged in recent years resulting in a diversified array of applications such as smart agriculture [1, 2], delivery of commercial products as well as life-saving equipment [3], inspection, entertainment, 3D imaging, and responding to natural disasters. However, most of these (and other) applications make use of a single drone that usually communicates with or senses a signal arriving from a node that is not mobile in 3D space (*e.g.,* cellular base station). Drone swarms and related research is still in its infancy. Currently, even if a group of drones could appear to be coordinating, this coordination is pre-planned and non-adaptive. For example, festivals and exhibitions that demonstrate drone swarms forming different shapes through lights, such as Intel's 1825 drones fleet in Tokyo Olympics (2021), leverages pre-planned flights that do not necessary require communication across the drone swarm.

The next wave of applications will be the use of UAV swarms to achieve certain tasks. For example, in a search and rescue mission, a swarm of UAVs could cover a larger area compared to a single drone, thus resulting in a faster and a higher probability of mission success. One key limitation of UAV swarms, however, is the communication channel between the drones. In a swarm, drones can have any arbitrary heading direction and exist at various relative elevation angles from each others. Moreover, the antennas mounted on these drones can be of different types, have different orientations, and be mounted on different positions.

In addition to cooperating in a swarm, UAVs can simultaneously serve nodes on the ground using multiple mounted antennas. The ground node could be a fixed base station, a person holding a device, or a moving target. In these cases, factors such as the surrounding environment or the body-induced effects from the human holding the device could add to the

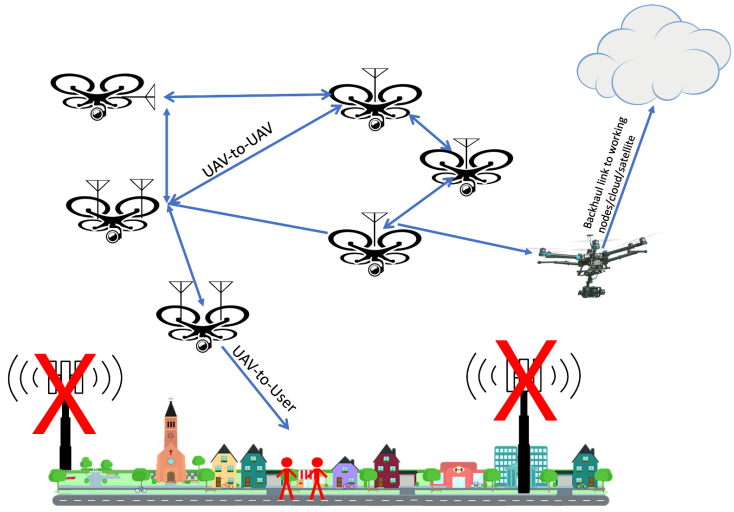

Figure 1.1: Scenarios for UAV swarms.

complexity of the wireless channel resulting in potentially different channel effects compared to aerial nodes. Fig. 1.1 illustrates an example of a disaster recovery scenario where a swarm of UAVs provide communication services to an area that lost its communication infrastructure. In such scenario, UAVs communicate with each other, with fixed ground nodes, and with moving objects on the ground such as humans and vehicles. The wireless links in such scenario are exposed to the various above-mentioned factors and studying the interaction bet'ween them is necessary.

One issue with current UAV literature is that the majority of it is still theoretical. If we were to lookup the proceedings of a venue that targets UAV communications, we will find that most of the works presented are theoretical contributions that, while valuable, need to be experimentally verified. (An example of this claim can be found in the UAV-related workshops at the International Conference on Communications (ICC), IEEE's Flagship conference; for example, in 2019 only 8% of the UAV-related papers were experimental.) Optimization models that target optimal deployments and trajectories constitute the majority of drone-related works. Unfortunately, these works make many assumptions and neglect important factors (discovered or emphasized in this work) that could lead to misleading results. Grounding these studies to reality, through extensive and careful experimentation, is essential. This is

one contribution of this work.

Measurement based studies that characterizes UAV-based channels have recently emerged and became more common. These studies, however, mostly target air-to-ground channels. The focus on air-to-ground channel might be due to the fact that less efforts are needed in terms of experiment design and automation compared to UAV-to-UAV channels. Therefore, there is a need for studies that investigate air-to-air channels in 2D and 3D space. Lastly, even in the air-to-ground literature, the ground nodes are either cellular base stations, such as the LTE eNB station [4], cars [5], or tripod-mounted nodes above the ground [6]. The role of the human body on such channels, with the exception of a few recent works [7], have been mostly disregarded in literature. Therefore, studies that target the above-mentioned issues, and contribute to understanding them, are necessary.

1.1 Summary of Thesis Contributions

UAVs within a swarm can communicate with each other to accomplish a certain task (*e.g.*, find a missing person or deliver data to remote area), communicate with a ground base station in scenarios of natural disasters, or work as a personal base station to communicate with only one or a handful of users/soldiers on the ground. An illustration of these use cases is shown in Fig. 1.1.

In such scenarios, the antenna position on the UAV, its orientation, radiation pattern, and polarization could have a considerable impact on the wireless channel as we shall see in this work. Furthermore, as the location of the drone changes, these effects can vary accordingly. For example, When a UAV changes its heading direction, its body can become an obstacle in the signal path affecting both, the magnitude and phase of the waves arriving at the antenna. In addition, when communicating with humans on the ground, the body of the human can influence the wireless channel in a way that depends on their orientation relative to the flying drone and the location of the device near their body.

Our work addresses these aforementioned issues and can be summarized as follows. First, we understand the fundamental effects of the UAV body on the radiation pattern and polarization (direction of the electric field) of UAV-mounted systems. In doing so, we conduct several anechoic chamber experiments and evaluate the radiation pattern of vertically and

horizontally mounted antennas while rotating the antennas 360°. The experiments are conducted first without the drone body and then with the drone body to directly compare and evaluate the UAV body effect. The obtained findings from this work can be useful when designing UAV swarms, for in a swarm topology, UAVs will ultimately be at different directions from each other and their bodies should be taken into account.

Second, we conduct several experiments to understand UAV-to-UAV channels in 2D and 3D space. In doing so, we design several flight paths where UAVs visit different waypoints resulting in either partial or full obstruction of the mounted antennas by their bodies. We analyze channel fading, both large-scale and small-scale, shadowing induced by the drone body, and the impact of having different antenna orientations on the drone on the wireless channel performance. Six different single-input-multiple-output (SIMO) setups/antenna configurations at the receiver are investigated. The role of elevation angle is of particular interest and is thoroughly analyzed in terms of received signal strength (RSS) and signal-to-noise-ratio (SNR) improvements that are achievable due to having multiple antennas. We analyze small-scale fading in UAV-to-UAV channels for co-polarized and cross-polarized antenna setups. Specifically, we analyze the Rician K-factor – which is the ratio of the power of the main LOS component to multipath components and a measure of channel fading severity – across all antenna orientations and elevation angles and draw important insight that has not been provided by any other work regarding how the K-factor for co-polarized and cross-polarized links behave across the different UAV elevation angles.

Third, to understand the ground effects on UAV-based channels and decouple them from antenna/body effects, we conduct UAV-to-Ground experiments with the same setup for the previous experiments and compare the results. We also calculate and analyze how the envelope correlation coefficient of our drone-based multiple antenna system might be affected by the elevation angle, antenna orientation, and spacing decision.

Finally, to complete the picture and understand how humans can possibly influence UAV-to-ground channels, we conduct several experiments that span three different use cases of holding a device, eighteen UAV hovering positions, and two carrier frequencies. We first start with free-space experiments and compare the results to when there exists a human body. Then, for the same human subject we investigate how their orientation and near-

body location of the communication device can affect the channel. Analysis is conducted in terms of shadowing, multipath, and the Rician K-factor. Insight is then drawn regarding the optimal UAV hovering position based on the observed use case. Then we conclude with possible applications highlighting the impact of our findings on air-to-ground channels that seek including the human body into such channels, as opposed to the majority of related work which do not consider such factor.

1.2 Thesis Overview

This thesis is structured as follows. In Chapter 2, we present the background needed to understand this work. We start with the theory and fundamentals of wireless communications, then we discuss the hardware and software setup. In Chapter 3, we analyze the impact of the UAV body on radiation pattern and XPD and quantify the effect of azimuth and elevation angle and antenna spacing on the performance of UAV-to-UAV channels in 2D and 3D space. In Chapter 4, we investigate UAV-to-ground channels for various antenna setups without the involvement of humans on the ground. In Chapter 5, the impact of the human body is quantified for different use-cases of holding a device on the ground across various UAV hovering positions and carrier frequencies. We then conclude in Chapter 6 and discuss possible future work.

Chapter 2

Background

The objective of this work is to better understand UAV-based channels under different contexts and application scenarios. Before we tackle these issues, however, it is important to explain some of the underlying concepts.

2.1 Radiation Pattern

The energy flux density and the direction of propagation of an electromagnetic wave is the result of the cross-product of two fields, the electric field and the magnetic field. The intensity of the radiated power is usually described by a certain radiation pattern model that represents the power radiated in the elevation and azimuth planes. An isotropic antenna, which is an idealistic view of how radiation occurs, radiates electromagnetic energy equally in all directions. Omni-directional antennas, on the other hand, radiates equal energy in the azimuth plane (*i.e.,* across all ϕ) while the magnitude of radiation in the elevation plane is a function of the elevation angle, θ. A vertically oriented dipole antenna for example, has a radiation pattern that can be described as [8]:

$$U(\theta, \phi) = \cos^n(\theta) \tag{2.1}$$

With n determining the directionality of the radiation pattern. The larger the n the narrower the radiation pattern beam in the elevation plane and consequently the more directivity. Since omni-directional antennas radiate equal amount of energy across all ϕ values, its value is only dependent on θ.

2.1.1 Antenna Radiation Pattern Modeling for Different Orientations

The antennas used in our work are linearly-polarized omnidirectional dipole antennas (VERT2450) [9]. To explain how we model the radiation pattern of this antenna, we show a

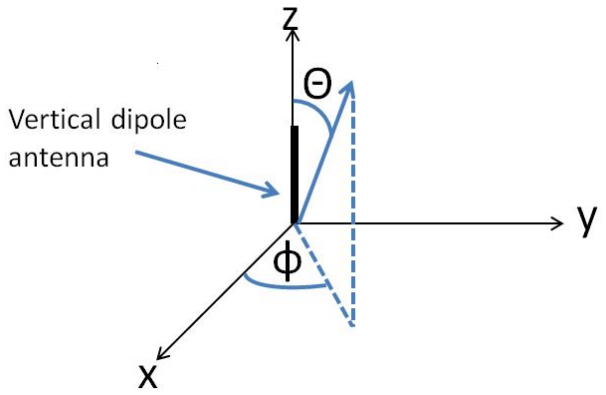

Figure 2.1: Vertically oriented dipole antenna.

vertically-oriented dipole antenna along the z direction in Fig. 2.1. The radiation pattern in the elevation plane is measured from the vertical (z) direction and described in the spherical coordinate system in terms of Θ. Conversely, the horizontal (azimuth) plane is described in terms of Φ. In the case of a vertically-mounted dipole, the radiation pattern[1] is given by [8]: $G_z = \sin\Theta$, with no azimuth variation. Note that this assumption of no azimuth variation for omnidirectional antennas will be proven here to no longer hold true when the antenna is mounted on a drone.

If mounted horizontally (*i.e.*, over the x-y plane), the pattern becomes: $G_y = -\cos\Theta\sin\Phi$. We use the notation of G_{VV} to indicate the gain product of vertical Tx-Rx antennas (VV link), whereas G_{VH} is used to indicate the gain product of a vertical Tx and a horizontal Rx antenna (VH link). Note that we are interested in the elevation angle θ from the xy plane, which is computed as $\theta = \frac{\pi}{2} - \Theta$. In our experiments, this elevation angle, θ, can be calculated using $\theta = \arctan(l/d_h)$, where l is the altitude of one drone relative to the other node, and d_h is the horizontal separation distance between the two nodes. Given these models, the gain product for a VV link becomes $|G_{VV}| = cos^2(\theta)$. For a VH link, the gain product becomes $|G_{VH}| = cos(\theta)sin(\theta)\sin\phi$. With the horizontal dipole mounted in the y direction, $\sin\phi = \sin\frac{\pi}{2} = 1$, and we are left with $|G_{VH}| = \cos(\theta)\sin(\theta)$. If we use these models and compare them to the manufacturer's datasheet [9], we find that the average difference between the two methods across the considered elevation angles is 1.14 dB with a

[1]Radiation pattern and gain are used interchangeably in this work.

standard deviation of 2.25 dB. Using this model allows us to study elevation dependencies with relatively low errors.

2.2 Polarization

Polarization is defined by the direction of the electric field [8]. In an ideal case, if two identical, linearly polarized (LP) antennas are oriented the same and used to communicate with each other, there should be no loss due to polarization mismatch. However, if an LP antenna is oriented with a tilt angle that is different from the angle of the incident wave, there will be a resultant loss which is only a function of the relative difference between the antenna's tilt angle and the incidence angle of the incoming wave. Cross-polarization discrimination (XPD), describes how well the two orthogonal polarization components (vertical and horizontal) can be separated by the antenna. This XPD is calculated as the ratio of the amount of power received in the co-polarized versus cross-polarized directions [10]:

$$XPD = P_{copol}/P_{xpol} \tag{2.2}$$

Here, P_{copol} can represent P_{VV} or P_{HH} and P_{xpol} can represent P_{VH} or P_{HV} where the first and second index represent the transmit and receive antenna orientations, respectively. The subscripts V and H denote vertical and horizontal antenna orientations, respectively.

Strong XPD values indicate strong separation of the two polarizations and that distinguishing between the two orthogonal components by the antenna is possible. Low XPD values indicate strong mixing between the two orthogonal components resulting in very little distinction between the two components. From the perspective of the wireless environment, strong LOS channels with minimal reflections can lead to strong XPD values while environments rich with scattering and reflecting components result in low XPD values. Hence, XPD in multiple antenna systems is directly related to the ability to perform spatial multiplexing and diversity. While low XPD values mean the two polarizations are strongly mixed and potentially resulting in no multiplexing gains, they can indicate a rich scattering environment with high diversity gains [11].

Impact of XPD on MIMO Capacity: To appreciate the influence of XPD variations on the capacity of multiple-input-multiple-output (MIMO) systems, we briefly discuss a 2×2 MIMO

system. We demonstrate the effect of XPD at different SNR regimes on the channel capacity of a 2×2 cross-polarized MIMO system. If we assume that we have a high K-factor that results in an approximately deterministic channel, mimicking an anechoic chamber setup, the channel can then be represented as:

$$\mathbf{H} = \begin{bmatrix} 1 & \sqrt{\eta} \\ \sqrt{\eta} & 1 \end{bmatrix}$$

where $0 \leq \eta \leq 1$ indicates the level of XPD. Very poor discrimination between the two orthogonal components would result in a high η, reaching approximately a value of 1, whereas perfect discrimination (very high XPD), would result in an almost zero value for η. The channel capacity at perfect XPD ($\eta \approx 0$) can be described as $C_{\eta=0} = 2\log_2(1+\frac{\gamma}{2})$, while at poor XPD ($\eta \approx 1$) it can be given as $C_{\eta=1} = \log_2(1+2\gamma)$. If SNR is high, then, $C_{\eta=0}$ can be approximated to $C_{\eta=0} \approx 2\log_2(\frac{\gamma}{2})$ and , $C_{\eta=1} \approx 1+\log_2(\gamma)$. At low SNR ($\gamma << 1$), and using the approximation, $\log_2(1+a) = a\log_2(e)$, the channel capacity at perfect XPD becomes $C_{\eta=0} \approx \gamma\log_2(e)$, while at poor XPD the capacity becomes $C_{\eta=1} \approx 2\gamma\log_2(e)$. Therefore, it is clear that at high SNR values, high XPD can provide substantial improvements in channel capacity. However, at low SNR values, high XPD results in no increase in channel capacity. Very poor XPD can indicate a richness in scattering in the environment and therefore, diversity gains can be achieved. This of course, relates to how relative direction and/or the rotation of a drone can affect SNR and consequently the achieved capacity given a certain XPD in a drone-based MIMO channel. A numerical example is given in Fig. 2.2. It is clear that at high SNR regions, low XPD values can lead to significant degradation in the capacity achieved by a MIMO system. At low SNR, however, the impact of XPD on spatial multiplexing and achieved capacity is negligible.

2.3 Signal Model

In our work, the transmitted signal can be represented by [12]:

$$s(t) = \Re\{m(t)e^{j(2\pi f_c t+\phi_o)}\} = \Re\{m(t)\}\cos(2\pi f_c t+\phi_o) + \Im\{m(t)\}\sin(2\pi f_c t+\phi_o) \quad (2.3)$$

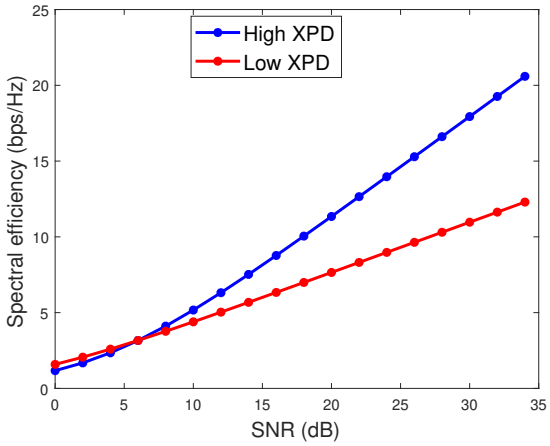

Figure 2.2: Impact of XPD on the capacity of a 2×2 MIMO system.

Here, $m(t)$ is the message signal and f_c is the carrier frequency generated by the local oscillator with a phase offset of ϕ_o. When the transmitted signal passes through the wireless channel, which can be considered as a linear time-invariant (LTI) system, the received signal will be a scaled and phase-shifted version of the transmitted signal. Due to multipath reflection, multiple components will have to add up at the receiver, giving rise to constructive and destructive interference. Hence, the received signal can be represented by:

$$r(t) = \Re\{\sum_{n=0}^{N(t)} \alpha_n(t) m(t - \tau_n(t)) e^{(j2\pi(f_c(t-\tau_n(t))+\phi_{D_n}+\phi_o))}\} \tag{2.4}$$

Where $N(t)$ is the number of multipath components, τ_n is the propagation delay of component n which is equal to $r_n(t)/c$ with $r_n(t)$ and c being the path length in meters and c the speed of light; $\alpha_n(t)$ is the amplitude of the n^{th} multipath component, and ϕ_{D_n} is the phase shift due to Doppler shift. Since our work is mainly with narrowband channels, multipath components are non-resolvable because the time difference between, say two components is not much greater than the inverse of the bandwidth [12].

If an unmodulated continuous wave (CW) transmission is used, the transmitted signal is

$s(t) = \cos(2\pi f_c t)$ and the received signal can be written as:

$$r(t) = \Re\{[\sum_{n=0}^{N(t)} \alpha_n(t) e^{-j\Phi_n(t)}] e^{j2\pi f_c t}\} \tag{2.5}$$

Where we have collected the phase terms in Φ. That is, $\Phi_n(t) = 2\pi f_c \tau_n(t) - \phi_{D_n} - \phi_o$. The received signal can be written as:

$$r(t) = r_I(t)\cos(2\pi f_c t) + r_Q(t)\sin(2\pi f_c t) \tag{2.6}$$

Where $r_I(t) = \sum_{n=0}^{N(t)} \alpha_n(t)\cos\Phi_n(t)$ is the in-phase, and $r_Q(t) = \sum_{n=0}^{N(t)} \alpha_n(t)\sin\Phi_n(t)$ is the quadrature component. After quadrature demodulation and low-pass filtering, and assuming there is no carrier frequency offset (CFO), the received signal at baseband (which is used for actual processing) has the complex magnitude of:

$$\hat{r}(t) = |r(t)| = \sqrt{r_I^2(t) + r_Q^2(t)} \tag{2.7}$$

2.4 Fading and Pathloss

The stochastic nature of the wireless channel makes it best described in terms of statistical distributions. The random fluctuation in the attenuation of the wireless signal as it propagates through the medium is called fading. Fading can be measured and modeled on a small-scale of time and space (on the order of a wavelength) or on a larger scale usually as an average over many meters of distance or large scales of time. In this section, we describe how to model small-scale and large-scale fading of UAV-based channel.

2.4.1 Small-scale fading

Depending on the nature of the multipath environment, the statistical distribution of the received signal envelope will change. If there exists no LOS component (NLOS), then the in-phase and quadrature components can be modeled as two zero mean Gaussian random variables and the envelope will be Rayleigh distributed. On the other hand, if there exists a strong/dominant LOS in addition to the multipath components, then, the in-phase and

quadrature components are not zero mean and the complex envelope has a magnitude that can be better represented by a Rician distribution. The Rician probability density function is given by [12]:

$$f(r) = \frac{\hat{r}}{\sigma^2} \exp(-\frac{\hat{r}^2 + a^2}{2\sigma^2}) I_o(\frac{\hat{r}a}{\sigma^2}), r \geq 0 \tag{2.8}$$

where a represents the amplitude of the direct component and $2\sigma^2$ is the average power of the multipath components. The ratio of power in the main LOS component to that obtained by the rest of multipath components is an important indicator of channel fading severity and is conventionally known as the Rician K-factor. The Rician K-factor in (dB) is given by:

$$K(dB) = 10 \log_{10}[\frac{a^2}{2\sigma^2}] \tag{2.9}$$

In this work, we will model the channel, investigate the hypothesis that it is a Rician channel when experiments are conducted in LOS, and then we will analyze small-scale fading in terms of the Rician K-factor. Specifically, we will study the impact of UAV body, antenna orientation, ground reflection, and the human body on the K-factor.

It is important to understand how the K-factor can affect the actual performance of digital communication systems. Not only the K-factor is an indicator of fading severity and how deterministic the channel is, but it can be directly related to the bit-error-rate (BER) of wireless communication systems. To realize the impact of these K variations on system performance, we simulate a 64-QAM Rician fading channel with different K values. The results are shown in Fig. 2.3. We can see that a reduction of K from 20 dB to 3 dB can, at an SNR of 18 dB, increase the bit error rate (BER) by three orders of magnitude.

2.4.2 Large-scale Fading and The Pathloss Model

In the previous subsection we discussed multipath effects and how the channel can be modeled as a function of the multipath nature in the environment. Signal fluctuations in the previous section are on a small-scale of space (at the order of a wavelength or smaller) and time (depending on the symbol/signal duration of interest). In many times, we find ourselves interested in understanding the average wireless link performance when changes occur on a larger scale of distance and/or time. For example, how does the received signal varies as the

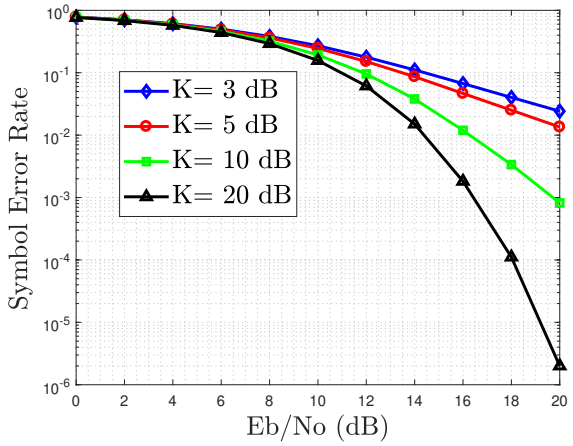

Figure 2.3: The impact of K-factor variations on symbol error rate for a 64-QAM system in a Rician fading channel.

transmitter-receiver distance changes by 40 or 100 meters? In such scenario, we are only interested in what is conventionally known as the large-scale fading nature of the channel. Such large-scale changes in distance usually mean changes in the surrounding environment and nature of obstacles around. When large-scale fading is considered, pathloss models are usually used to predict the received signal power at further distances. A pathloss model uses measurements to model the relationship between distance and received power or pathloss. The reduction in received power due to distance can be described by the log-distance pathloss model [12]. In particular:

$$PL(d) = PL(d_{ref}) + 10n \log \frac{d}{d_{ref}} + \chi_{\sigma_s} \tag{2.10}$$

where $PL(d)$ is the pathloss at a distance d, χ_{σ_s} is the shadowing parameter, which is usually modeled as a zero mean Gaussian random variable, $PL(d_{ref})$ is the pathloss at a reference distance, and n is the pathloss exponent. Using the reference pathloss at a known distance (usually measured or referred to from a known environment) one can predict the received signal power at further distances. However, in aerial communications, due to the 3D nature of the channel which is a function of the location of the UAV and its mounted antennas' 3D radiation pattern, such models can fall short due to excluding how the radiation pattern in

one plane can be very different at other elevation/hovering angles. Hence, angle-dependent models are more suitable for UAV-based channels [4, 13].

2.4.3 Angle-dependent Models for UAV Channels

In this section, we demonstrate the reason behind the need for angle-dependent models for UAV communications. In free-space, and assuming a deterministic channel, *i.e.,* no random channel fading, the received power can be described by the Friis formula where the received power is a function of deterministic factors. Specifically, the received power is a function of the transmitted power P_t, Transmit/Receive (Tx/Rx) antenna radiation patterns (G_T and G_R), carrier wavelength λ, distance d, and polarization loss factor ψ. It can be described by the Friis formula [8]:

$$P_r(\theta, \phi) = P_t G_T(\theta, \phi) G_R(\theta, \phi) (\frac{\lambda}{4\pi d})^2 \psi \tag{2.11}$$

In co-polarized links, the polarization of the incident electric field matches the polarization of the receiving antenna, and no losses are incurred. On the other hand, in a cross-polarized link, due to the mismatch between the direction of the incoming electric field and the receiving antenna orientation, the received signal is reduced.

For a polarization-matched link, the free-space received power is given by:

$$P_r(dBm) = P_t(dBm) + 10\log(G_{T,R}) + 20\log(\frac{\lambda}{4\pi d}) \tag{2.12}$$

Here, $G_{T,R} = G_T G_R$ is the transmit-receive antenna radiation pattern product discussed above. To account for shadowing caused by objects in the Tx-Rx path, equation (2.12) should include a shadowing term ξ_s, which is usually modeled as a normally-distributed random variable with zero mean and a standard deviation of σ_s (*i.e.*, $\mathcal{N}(0, \sigma_s)$). Finally, as the drone can rotate in any direction while hovering at a fixed altitude, we find that the average RSS can be reduced due to drone body blockage. As a result of this body blockage, the received power will be reduced by a term denoted here as $\Gamma_\phi(\theta)$ which is specific to the drone body. The dependency of $\Gamma_\phi(\theta)$ on elevation angle will be discussed in Section 3.4.2.

When the shadowing and body-induced losses are added to equation (2.12), it becomes:

$$P_r^{VV} = P_t + 10\log(\cos^2\theta) + 20\log(\frac{\lambda}{4\pi d}) - \xi_s - \Gamma_\phi(\theta) \tag{2.13}$$

For the VH link, the received power becomes:

$$P_r^{VH} = P_t + 10\log(\cos\theta\sin\theta) + 20\log(\frac{\lambda}{4\pi d}) - \xi_s - \Gamma_\phi(\theta) \tag{2.14}$$

Angle-dependent vs. Distance-dependent Loss: It is important to understand that in some scenarios, angle-dependent models are more convenient and help to accurately characterize the behavior of drone-based links over conventional, distance-based models. This observation was mentioned in other works such as [4, 13], but no examples were given to quantify the effect. Here, we provide an example scenario where angle-based models greatly outperform distance-based models. In this example, a ground node communicates with a hovering drone with a fixed horizontal distance of $d_h = 20$ m. The drone moves from an altitude of $l = 10$ m to l =30 m in 10-m increments. The elevation angles created are, respectively, 26.5°, 45°, and 56.3°. If we exclude the radiation pattern effects, the reduction in power due to the increase in the separation distance from $d = \sqrt{(}20^2 + 10^2) = 22.3$ m to $d = \sqrt{(}20^2 + 30^2) = 36$ m is approximately 4 dB. If we model the elevation pattern of each of the Tx/Rx antennas as $\cos^2(\theta)$, the loss just due to the antenna pattern misalignment would be $10\log(\cos^4(\theta)) = 10\log(\cos(\tan^{-1}(\frac{l}{d_h}))^4)$ =10 dB. Hence, by excluding the radiation pattern in this scenario, the received power would be overestimated by 6 dB. Conventional pathloss models that relies on taking a reference pathloss measurement in a certain direction can result in underestimating pathloss in 3D aerial communications due to different azimuth and elevation radiation pattern values in different directions.

In an ideal scenario, the transmitter and receiver antenna are perfectly aligned (*i.e.*, $\theta = 0°$), and the loss is 0 dB. The antenna gain product for the three altitudes and horizontal distances of up to 80 m is shown in Fig. 2.4. We can see that the effect of the gain product is greatest at small horizontal distances with high drone elevations (*i.e.*, large elevation angles). As the horizontal distance increases for a fixed altitude, the elevation angle becomes smaller, resulting in a small antenna gain misalignment loss compared to losses due to the increasing

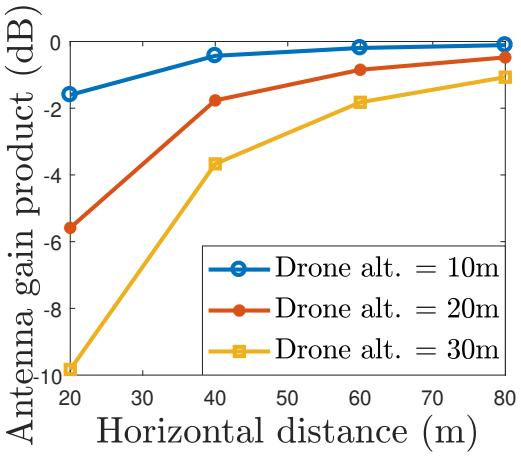

Figure 2.4: Tx-Rx antenna gain product for omnidirectional dipole antennas at different elevation scenarios. At some angles, losses caused by radiation pattern misalignment can be greater than distance-based losses.

distance. In our 3D experiments we will include the radiation pattern effect according to (2.13) and (2.14). Given that $d_h = d\cos\theta$, $|G_{VV}| = cos^2(\theta)$, $|G_{VH}| = cos(\theta)sin(\theta)\sin\phi$, which at $\phi = \frac{\pi}{2}$ becomes $|G_{VH}| = cos(\theta)sin(\theta)$, and by subtracting P_r from P_t, the angle-dependent loss for the VV and VH links, after some manipulation, respectively, becomes:

$$L_{VV}(\theta) = 20\log\left(\frac{4\pi d_h}{\lambda\cos(\theta)^2}\right) + \xi_s + \Gamma_\phi(\theta) \tag{2.15}$$

$$L_{VH}(\theta) = 20\log\left(\frac{4\pi d_h}{\lambda}\right) + 10\log\left(\frac{1}{\cos(\theta)^3\sin(\theta)}\right) + \xi_s + \Gamma_\phi(\theta) \tag{2.16}$$

2.5 Software-Defined Radios, Signal Generation, and Logging

Software defined radios (SDRs) are radio equipment that contain RF front-ends and baseband units which are fully controllable and programmable. Their architecture allows for easy deployments and adaptability to changing requirements. For these reasons, SDRs have recently become a ubiquitous wireless experimentation tool. In this section we briefly describe the software and hardware used in this work.

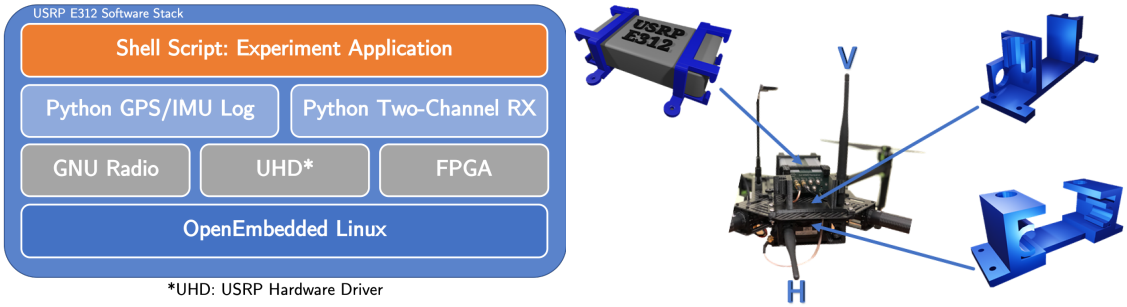

(a) (b)

Figure 2.5: (a) Experiment software stack using SDRs. (b) Illustration of 3D printing of antenna mounts.

2.5.1 Hardware and Software Design

In all experiments, two of the Universal Software Radio Peripheral (USRP) E312s from Ettus Research™ are configured for collecting measurements. The antennas are directly connected to the TxRX or Rx port using an SMB to SMA adapter. When mounting on the UAV body, which is a DJI Matrice 100, the radios are mounted to the top center of the body using a specially designed 3D printed bracket (see Fig. 2.5). Multiple antennas can be mounted on the drone body. We are able to mount the following configurations of two antennas: VV, VH, HH, HV, DD, and HV with V, H and D indicating, respectively, vertical up, horizontal and vertical down antenna orientations.

The USRP E312 runs a Linux distribution based on OpenEmbedded with driver support for interfacing with the radio hardware using Ettus' USRP Hardware Driver (UHD). The GNU Radio Companion (GRC) is used on a host machine to develop signal processing flowgraphs. UHD is leveraged within the flowgraphs to interface with the RF front end on both radios via the FPGA fabric. In most experiments a modulated/unmodulated carrier is sent at different frequencies (2.5 GHz and 900 MHz) at 32kS/s, 64kS/s or 1.25MS/s. The receiver, sampling at the same rate, is configured to write the received IQ samples to a binary data file as complex floats. Then, from the IQ samples, we calculate the complex magnitude of the received signal according to . Large-scale and small-scale fading analysis is then conducted according to the aforementioned methods.

Drone Description: The body and frame of the Matrice 100 is made up of various

lightweight materials including carbon fiber, aluminum, plastic, and steel. The frame is braced with aluminum brackets and held together with steel screws. The majority of the frame, including the top and bottom plate as well as the propeller arms, is constructed out of epoxy hardened carbon fiber weave. Carbon fiber is known to shield radio frequencies but the degree of shielding largely depends on various characteristics of how the carbon fiber is manufactured. The exact characteristics of the carbon fiber used by DJI are unknown to us and this limits our ability to fully model its effects. While not the focus of this investigation, our anechoic chamber experiments should capture the behavior that this particular drone body presents.

Experiment Control and Data Logging: The experiments' software is mostly designed and written using flowgraphs that are compiled into a python script within the GRC environment and the resultant python code is transferred to the USRP E312 to be executed in the embedded environment. An additional python script is then developed in order to log the output from the GPS receiver and inertial measurement unit (IMU) internal to the USRP E312. Time, location, altitude and orientation data are logged to a text file every half-second. To maintain efficiency while performing experiments, a controlling shell script is written to automate the execution of the two python files. In addition, the shell script also logs an additional timestamp of when the python scripts are executed for more precise offline synchronization of location data. An experiment that has two simultaneously receiving antenna generates 4 data files: shell script log, GPS/IMU log, and two files for each channel of received IQ samples. Received power is calculated offline at each point of interest. In order to take repeated drone-based measurements at the defined 3D points of interest, the flight controller is programmed with a GPS based waypoint mission. The software stack of our system is shown in Fig. 2.5.

Chapter 3

Characterization of UAV-to-UAV and UAV-to-Ground Channels in 3D Space

In this chapter, we study the role of the UAV body and different antenna positions and orientations on the large-scale and small-scale fading of UAV-to-UAV and UAV-to-Ground channels. Through systematic in-field experimentation, we prove that the drone body can significantly change the radiation pattern of mounted antennas and the polarization of the electromagnetic wave resulting in significant degradation of XPD. We minimize environmental effects by conducting a series of line-of-sight (LOS) experiments in an almost building-free environment in Taos, New Mexico. We address how the orientation and location of drone-mounted antennas can affect the fading nature of drone-based channels. We show that the drone body can increase the standard deviation of the shadowing parameter for polarization-matched vertical links. We also show that when the antenna is mounted on the opposite side of the receiving drone from the transmitter, the extra losses induced by the drone body need to be included in conventional models for more accurate predictions. We do that by analyzing and modeling the impact of the drone rotation on the average channel gain/loss and show improvements of up to 85% in prediction accuracy with rotational aspects taken into account.

Then, we move to characterizing the small-scale fading of these drone-based channels in terms of the Rician K-factor. We show that the K-factor is strongly dependent on elevation for polarization-matched vertical links, while it is approximately flat for cross-polarized links. To isolate the impact of position and orientation of the drone-mounted antennas and not confuse that with fading caused by the ground, we compare results of the Ground-to-Drone (GtG) experiments to those obtained by another set of Drone-to-Drone (DtD) experiments and find that ground reflections can reduce the K-factor by approximately 10 dB. However, as we move to higher altitudes, the K-factor observed by both experiments becomes approximately the same, indicating less of a role for the ground compared to the actual antenna

location and orientation. To the best of our knowledge, this is the first study to provide a systematic and comprehensive understanding of these fundamental drone-related issues.

The contributions of this paper are summarized as follows:

- We quantify, via anechoic chamber measurements, the effect of the drone body on the azimuth radiation pattern of omnidirectional antennas and find that, while the measured azimuth pattern is approximately constant for antennas in isolated mode (not mounted on a drone), it can vary by up to 10.25 dB when the same antennas are mounted on a drone. This finding proves that the assumption of a constant azimuth radiation pattern when dealing with drone-mounted antennas is no longer valid.

- We measure the co-polarized and cross-polarized radiation pattern of various antenna placements on the drone and show that the drone body can significantly impact channel depolarization and reduce XPD by an average of 15 dB compared to the XPD of an isolated antenna in the absence of a drone body.

- We show that there is an additional loss term caused by the drone body that needs to be accounted for unless the antennas on the transmitter and receiver are mounted on sides that face each other. This body-induced loss is found to be elevation-dependent for polarization-matched vertical links. We propose a model that describes this rotational loss and show that our model can be 85% more accurate than conventional models that neglect this body-induced effect.

- To understand how the orientation and location of drone-mounted antennas can affect small-scale fading, we characterize the Rician K-factor of the GtD channel and find that polarization-matched vertical links exhibit strong dependency on elevation, while cross-polarized channels result in an approximately flat behavior when elevation changes are considered. Then, by comparing a set of DtD experiments to our GtD experiments, we find that ground reflections can cause a degradation in the K-factor by up to 10 dB.

- Even though all of our experiments are conducted in LOS, we show that an antenna spacing of 0.67λ results in a correlation coefficient of less than 0.7 regardless of antenna

orientation. In terms of diversity, this indicates achievable diversity gains in the range of 9.5 to 11.5 dB with basic selection or maximal ratio combining techniques.

We first start with reviewing related literature then move to the experimental frame work, results and analysis.

3.1 Related Work

Broadly speaking, literature related to drone communications can be classified into two main areas: (*i.*) models that cover optimal placement, efficient deployment, and simulations that test different scenarios of trajectory and user mobility [14–16], and (*ii.*) measurement-based studies that investigate the wireless channel in the uplink or downlink direction between a flying drone and a fixed or a moving node on the ground or in the air. The wireless channel in these measurement studies can be categorized as an air-to-ground (AtG), ground-to-air (GtA) or air-to-air (AtA) channel, depending on the nature of the target node.[1]

AtG channels. Many works have investigated the wireless channel between a hovering drone and a ground user with emphasis on how distance and antenna orientation can affect the received power or throughput at the ground node [6,17–19]. The AtG channel at ultra-low drone altitudes was characterized with different settings of user equipment (UE) locations [7]. The AtG channel was studied after building a MIMO system that supports instantaneous measurements at different receiver locations on the ground as well as beamforming from the drone transmitting antennas [20, 21]. Shadowing was measured at diverse frequencies, and a modification to the conventional path loss model was made to account for the obtained frequency-dependent variations [22].

GtA channels. Due to its unique body structure, continuous movement, and limited space on board, in addition to being envisioned in scenarios where multiple antennas on the drone are receiving packets from ground sensors or users, the receiving channel characteristics of multiple drone-mounted antennas have been of interest. For example, the channel between a ground transmitter and an aircraft flying at speeds around 120 km/hour was studied, and it was concluded that placing two antennas one above and another below the aircraft body can result in throughput improvements [23]. Correlation coefficients and diversity gains

[1]While we would consider GtD/DtD a subset of GtA/AtA, we specifically use the former in this work to emphasize on the impact of the drone body on the wireless channel.

were studied for various antenna positions on a fixed wing structure and packet delivery improvements of up to 32% were achieved [24]. An array of multiple antennas at the ground was used to sound the channel in a forest environment, where a fixed wing UAV flew at different altitudes and with co-polarized and cross-polarized links, and measurements of the cross-polarization discrimination were made at those altitudes with some emphasis on the achieved gains using different antenna orientations [25]. In the same context of GtA channels, the work by Akram et. al. has resulted in an angle-dependent model for cellular-to-UAV channels, where the received power and the shadowing parameter can change based on the depression angle [4].

AtA channels. The channel in a drone-to-drone LOS scenario was studied at different altitudes, and an extension of the Rician model was developed, where the variance of the received power, which describes multipath components, was modeled as a function of the drone altitude [26]. The throughput of a two-hop network was studied under different scenarios of mobility [19]. While all of the above mentioned studies target important issues that can help in understanding drone communications, none of them consider how signal reception on a drone with multiple antennas can be affected by the drone body and its rotation. In addition, the environments in which the above mentioned experiments took place and the scenarios involved make it difficult to isolate the impact of the antennas and the drone body on the presented results. In contrast, this work focuses on the impact of the drone body and drone-mounted antennas via carefully-designed experiments.

3.2 The Impact of UAV Body Radiation Pattern and Polarization

Due to its unique structure and the various possible locations for antenna mounting, the drone body can affect the radiation pattern of the mounted antennas. With the exception of few works such as [7], most studies that present the radiation pattern of the antennas used in their UAV-related experiments disregard this impact [4, 6, 27]. In this work, we will show that the UAV can significantly alter both, the magnitude and phase of the arriving signal.

To quantify the impact of the drone body and antenna placement on the radiation pattern and polarization, we conduct multiple controlled anechoic chamber and in-field experiments. We show that placing antennas on drones is a nontrivial task due to the interaction of the

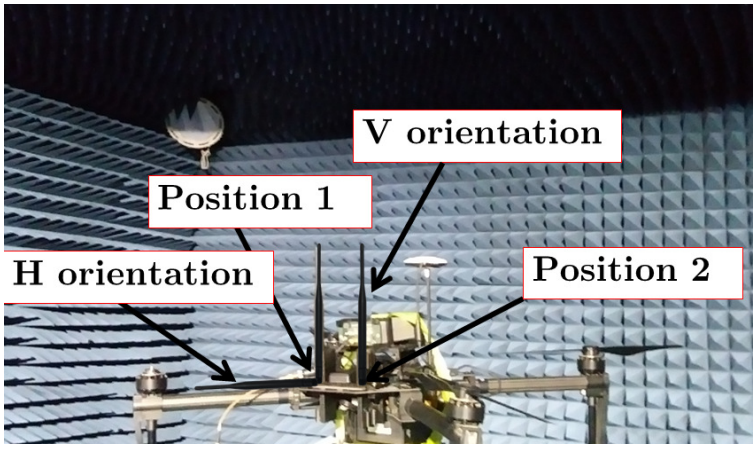

Figure 3.1: Anechoic chamber setup. The two antenna positions/locations are shown on the drone body.

drone body with mounted antennas.

The drone with the two antenna locations in the chamber is shown in Fig. 3.1. Note that to mimic the structure of the drone in our in-field experiments, the same experiment's hardware is mounted on the drone and explained in Section 3.4.1. In the isolated case, only the antenna is mounted at the receiving end of the chamber, and its radiation pattern is measured. Then, in the antenna-on-drone scenario, we place the antenna on the drone according to the positions shown in Fig. 3.1 and study the resulting radiation pattern. The transmitting antenna is fixed and vertically-oriented while the vertically-receiving antenna automatically rotates over the azimuth plane (ϕ) in 1.8° increments as the received power is being recorded.

The results of the anechoic chamber experiment are shown in Fig. 3.2. In this figure, "simulated" indicates a constant-azimuth radiation pattern, which is the general assumption made in most drone-related literature. The antenna-only measurements represent the measured values using the antenna in isolated mode, meaning only the antenna exists in the chamber. We see, as expected, strong symmetry and the radiation pattern follows closely the constant-azimuth pattern assumption made in literature. If we mount the antenna on the drone, however, the results become significantly different, and the constant-azimuth pattern is no longer valid. This variation can be clearly seen in the blue and red lines that

Table 3.1: Impact of Drone Body on Co-Polar Radiation Pattern Values

Experiment	**Average Loss**	**Maximum Loss**
Antenna on Drone (position 1)	2.57 dB	8.34 dB
Antenna on Drone (position 2)	3.27 dB	10.25dB

indicate the measured power values of the drone-mounted antennas, where differences from the isolated (antenna-only) scenario can reach up to 10.2 dB. In addition, there is also a difference in radiation pattern due to different antenna positions on the drone (see Fig. 3.1 for antenna positions). This difference can be seen by inspecting the red and blue lines in Fig. 3.2(a), which correspond to antenna position 1 and 2, respectively. In this figure, we point to an angle where we can see a difference of 6.5 dB, which is the maximum difference in radiation pattern due to different antenna locations on this drone. One might ask the question why such differences exist even though the antenna positions look symmetrical on the drone body. The answer is as follows: when the drone body starts to rotate, each Rx antenna sees a slightly a different signal level because each position exhibits a different part of the drone body (*i.e.*, obstacle). This difference is clear if we look at the difference in received power – by the two antennas – for the whole 360 degrees azimuth plane (shown in Fig. 3.3). As we can see in the figure, at 0 degrees (Facing tx antenna) there is approximately no difference. As the drone rotates, however, differences in rx power manifest and cause the values of received power to slightly differ. In this figure (Fig. 3.3), $|\Delta_p(\phi)|$ is the absolute difference in received power between the two mounted antennas at positions 1 and 2, respectively.

The average and maximum reductions in radiation pattern for the two antenna positions are summarized in Table 3.1. These average and maximum losses are taken over the whole azimuth (ϕ) plane. The loss is simply the difference between the azimuth power in the isolated (antenna-only) scenario and the drone-mounted antenna scenario. We see that these losses can reach up to 10 dB, with an average of up to 3.3 dB. It is important to note that while this reduction might not seem significant, on average, reductions of more than 5 dB appear multiple times over the whole azimuth plane for a fixed antenna position. We conclude from these controlled experiments that antenna placement decisions on drones, trivial as

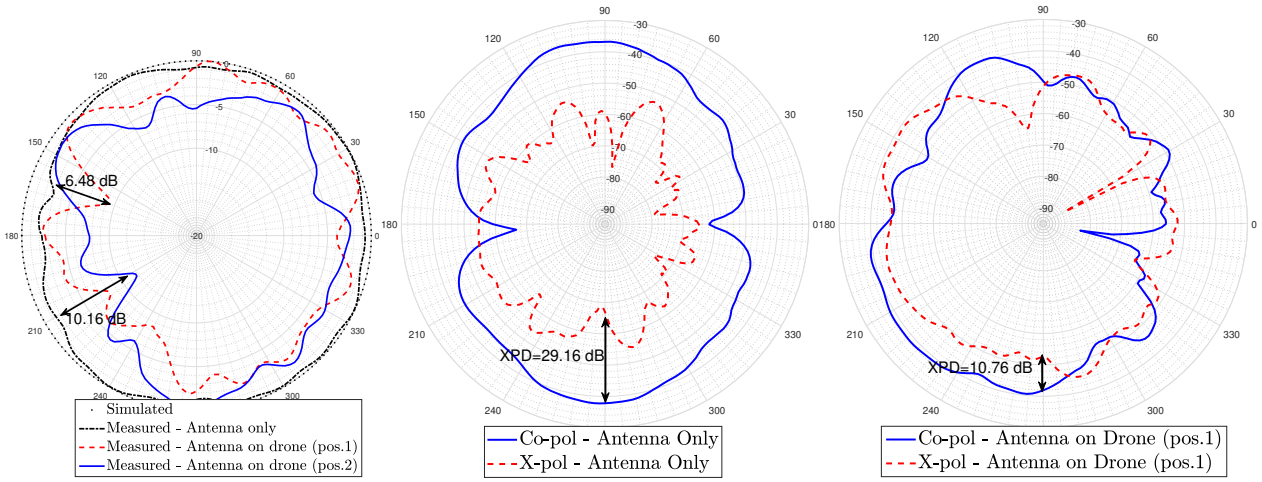

(a) Azimuth radiation pattern (b) co-pol/x-pol Antenna only (c) co-pol/x-pol Antenna position 1

Figure 3.2: (a) Azimuth radiation pattern for the simulated, antenna only (measured), and antenna on drone for two positions (measured). (b) The HH/VH co-polarized/cross-polarized radiation pattern for the antenna only setup: clear distinction between the two orthogonal polarizations exists. (c) The HH/VH co-polarized/cross-polarized radiation pattern for the antenna on drone setup (position 1): high polarization mixing exists due to the drone body.

they might seem, can considerably impact wireless channels in drone-based networks, where rotating a drone or switching to a nearby antenna on the same drone, can lead to significantly stronger channels.

3.2.1 Anechoic Chamber Cross-polarization Discrimination (XPD)

After realizing the impact of the drone body on the azimuth radiation pattern, a natural question comes to mind: Is the local scattering caused by the drone body strong enough to cause polarization mixing? If so, by how much? Here, we answer these questions.

The results of the measured co-polarized and cross-polarized channels for the antenna-only and antenna-on-drone (position 1) scenarios are shown in Fig. 3.2(b)-3.2(c). Through a quick visual inspection, we can see that there is a clear distinction between the co-polarized and cross-polarized received powers in the isolated (antenna-only) scenario. This distinction, however, becomes almost nonexistent for the antenna-on-drone scenario. The disappearance of this distinction is due to higher polarization mixing between the vertical and horizontal components, caused solely by the drone body. This polarization mixing, according to the

geometrical theory of channel depolarization [28], can be attributed to the local scattering and reflection caused by the drone body.

While there is an abundance of works on XPD and how it is affected by scattering objects [10, 29–31], none have investigated the drone body as the only source of polarization mixing, except for one other work [32] that was published around the same time as our work [11]. Here, we show that the drone body *by itself* can act as a source of scattering and reflection, demonstrated by significant reductions in XPD. For example, if we look at XPD at $\phi = 270°$, we can see that in the isolated scenario, XPD is 29.16 dB. In the drone-mounted scenario at the same angle, it is 10.76 dB for antenna position 1 and 11.25 dB at antenna position 2 (not shown here). Over all rotational angles, the average XPD for the isolated (antenna-only) scenario is $\overline{XPD}_{isolated} = 17.33$ dB. In contrast, the average XPD for antenna positions 1 and 2 is $\overline{XPD}_{pos.1} = 2.33$ dB $\overline{XPD}_{pos.2} = 4.71$ dB, respectively. A similar (around 10 dB) degradation in XPD due to mounting antennas on the UAV were measrued in [32].

We believe that these are significant findings due to the impact that XPD can have on achievable capacity and diversity gains in MIMO applications that leverage cross-polarized channels [33]. For example, an average XPD value of 0 dB means that the spatial multiplexing gain is limited. On the other hand, the same 0 dB value can indicate a richness of scatterers in the multipath environment, which leads to a low correlation coefficient and high diversity gains [34]. While it can be argued that these results are specific to this drone (DJI Matrice 100), the insight we gain from this study can be valuable for drone swarm designers [35] or researchers who aim to model drone-based polarized MIMO channels. In addition, simulation tools, such as [36] can incorporate these findings through an *effective* antenna pattern and XPD lookup tables rather than treating the antennas as point objects, which is proven here to be highly inaccurate.

3.2.2 In-field XPD

We now evaluate the impact of different drone relative directions on the measured XPD from a set of experiments conducted in the field. The experiment set is conducted with two drones at an altitude of 60 m above the ground. While the Rx drone is continuously

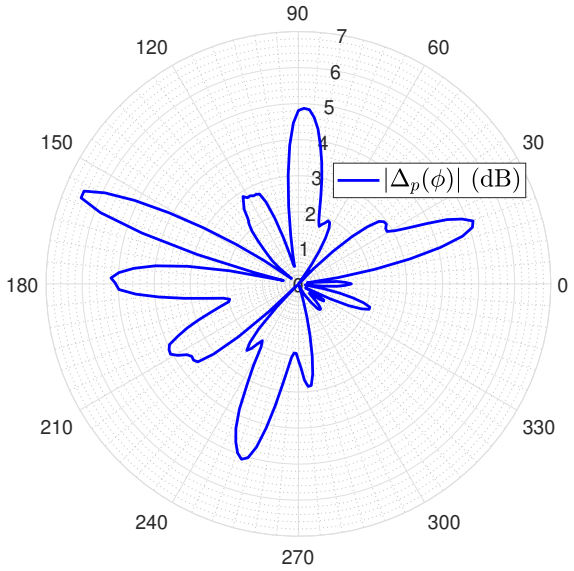

Figure 3.3: Difference in received power by the two vertically mounted antennas on position 1 and 2 in the anechoic chamber.

hovering at a fixed location, the Tx drone moves in 20 m increments from one location to another until it reaches 100 m of separation distance. This Tx drone movement takes place in each of the four cardinal directions (North, South, East, and West). See Fig. 3.4(a). The Tx drone has one vertically-oriented (V) antenna, while the Rx drone is equipped with one vertical and one horizontal antenna that are connected to the same USRP and fed from the same local oscillator. (For more details regarding the setup, refer to [11].) Both drones face North throughout all experiments. The Rx vertical (V) antenna is mounted in position 1 in Fig. 3.1, while the horizontal antenna (H) is mounted in position 2, creating two links denoted as VV and VH from the transmitter to receiver. We can view the receiver as a dual-polarized system and use our measurements for the VV and VH channels to predict the in-field XPD at the receiver. We follow [10, 30] and calculate XPD as the difference in co-polarized and cross-polarized pathloss (*i.e.*,, $XPD = PL_{VV} - PL_{VH}$) and investigate how diverse Tx directions from the Rx can affect polarization mixing at the receiver. XPD is calculated for each hovering location, and the results are summarized in Table 3.2.

We see that XPD can considerably change if the transmit drone takes different relative directions from the receiving drone. For example, we see that the strongest measured XPD

Table 3.2: XPD for Different Relative Directions in DtD Channels

Direction	**20m**	**40m**	**60m**	**80m**	**100m**	**Avg.**
XPD_{North}	1.29	1.55	2.64	2.1	3.53	2.22
XPD_{South}	5.67	3.45	7.61	6.01	5.2	5.58
XPD_{East}	4.56	10.1	11.61	8.0	8.32	8.51
XPD_{West}	4.2	9.83	11.24	10.6	8.43	8.86

values are when the transmit drone is on the side (East or West), while the lowest value is when the transmit drone is North of the receiving drone (shown in Fig. 3.4(b)). On average, the North XPD value is 6 dB less than that in the East or West and 3.3 dB less than in the South experiment. This result suggests that if the Tx drone is facing-away from the receiving drone, the transmitted polarization becomes almost independent from the received polarization. It is important to note that, while they fall approximately in the same range, the measured XPD values here are slightly different from the anechoic chamber results since the transmitter is actually mounted on a drone as opposed to just the antenna in the chamber. In addition, XPD here is measured using two antennas mounted on the Rx drone. In the chamber, we changed the orientation of the Tx antenna to get the cross-polar radiation pattern with the Rx antenna fixed. However, the focus here is not on replicating the chamber measurements in the field but to demonstrate the influence of different relative drone directions on XPD, which is found to vary by up to 10 dB (from 1.29 to 11.61 dB).

3.3 UAV-to-UAV Channels in 3D Space

After creating a baseine understanding of how the UAV body can affect the radiation pattern of antennas and the polarization of the arriving/departing waves, it is now convenient to move to characterizing the performance of UAV-to-UAV links with various antenna configurations and movement in 3D space.

It is well established in literature that the performance of MIMO systems highly depends on the spatial correlation of the channel matrix. This spatial correlation is found to vary according to changes in the channel induced by different antenna radiation patterns, spacing, orientation, polarization, and elevation and azimuth angle of arrivals [34,37,38]. In addition, recent studies, such as [39], found that, in drone swarm applications, if all ground station

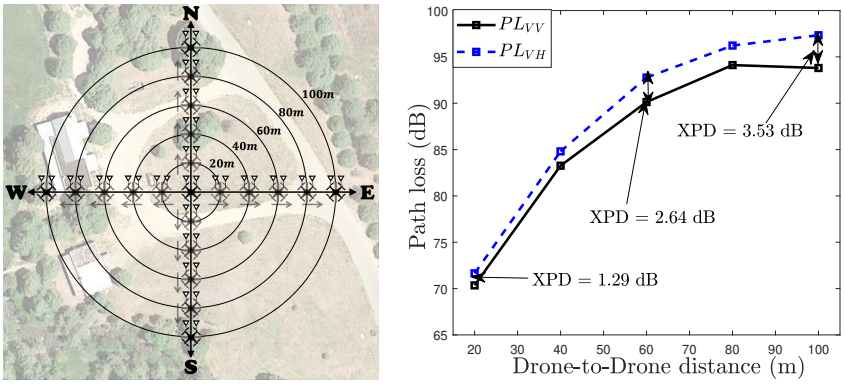

(a) (b)

Figure 3.4: (a) Illustration of the 2D Drone-to-Drone experiments. (b) Measured XPD values for the North scenario.

antennas are identically oriented and a UAV is moving at different elevation angles, the received signal can be effectively lost due to polarization mismatch. This motivates us to experimentally investigate the effects of elevation angle on the RSS with various antenna orientations at the receiver drone in a 1×2 receive diversity system. First, we discuss the experiment procedure. Then, the effect of the elevation angle on RSS for different antenna orientations is analyzed. After that, we discuss antenna spacing and correlation and conclude the section with SNR gains due to diversity and their dependence on antenna orientation and elevation.

3.3.1 Experiment Procedure

In this set of experiments, the transmitting UAV is hovering at an altitude of 80 m with its transmitting antenna oriented vertically upward (VU), facing the receiving drone which moves around the transmitting UAV in a predefined sequence of hovering locations, creating a 3D shape (Fig. 3.5). Diversity is implemented at the receiving UAV which flies in an automated, repeatable fashion using waypoints and resulting in four distinct (negative) angles below the transmitter and four (positive) angles above the transmitter. The below and above points are separated by an elevation angle of $\theta_{elev.} = 0°$. The horizontal distance (d_h) between the Tx and Rx drones is 20 m at $\theta_{elev.} = 0°$ and the angle-specific distance

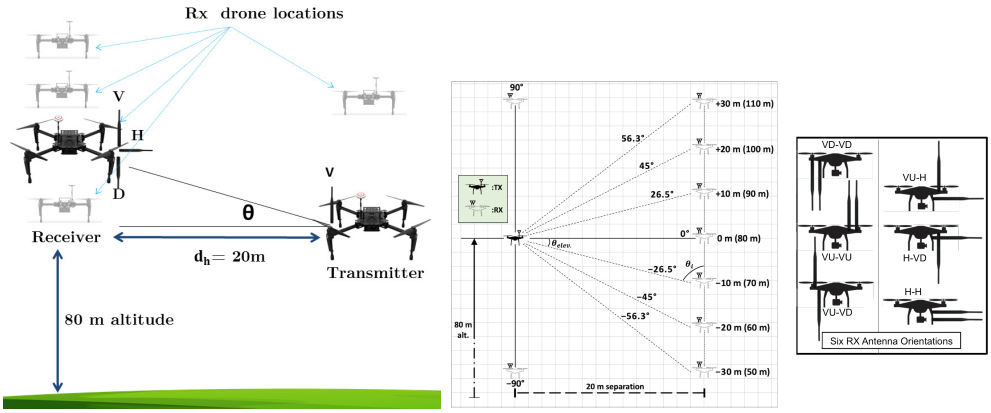

(a) (b)

Figure 3.5: (a) Illustration of Drone-to-Drone experiments. (b) Illustration of the experiments' elevation angles with with 6 Rx antenna orientation combinations in the 1×2 diversity system.

is $d_{\theta_{elev.}} = \sqrt{d_h^2 + d_v^2}$, where d_v is the vertical distance, which varies from -30 m (*i.e.*, 50 m above ground) to +30 m (*i.e.*, 110 m above ground) in 10-m increments. The different elevation angles made (in sequence) are: $-90°$, $-56.3°$, $-45°$, $-26.5°$, $0°$, $+26.5°$, $+45°$, $+56.3°$ and $+90°$ and can be calculated as $\theta_{elev.} = \arctan(d_v/d_h)$.

Experiments are carried out for six different antenna orientation combinations (VU-VU, VU-VD, VU-H, VD-VD, H-H and H-VD) where VU, VD, and H represents vertical-up, vertical-down, and horizontal antenna orientations, respectively. See Fig. 3.5. The received signal strength (RSS) is recorded at each hovering location for 30 s at a sampling rate of 32k samples/s and averaged over 10 seconds. The two UAVs are in a perfect LOS condition at a carrier frequency of 2.5 GHz and a measured average noise floor of -110 dBm.

The average RSS values are fitted using a second-order polynomial in the range $\theta_{elev.} = -56°$ to $+56°$, and the results are plotted and analyzed.

3.3.2 Effect of Elevation Angle on UAV-to-UAV Channels

In this section, we study the dependence of RSS on the elevation angle between two drones for different antenna orientations. In general, if we look at Figs. 3.6(a) and 3.6(b), we observe an expected trend where the average RSS follows an arch-like shape in all vertically-oriented antennas in the range $\theta_{elev.} = -56°$ to $+56°$, with the strongest average RSS recorded at an

elevation angle of $\theta_{elev.} = 0°$; this is where the two drones exhibit perfect LOS at the same altitude. As the receiving drone starts moving up (to 110 m) or down (to 50 m), reductions in the signal level start to appear. These reductions are mainly caused by polarization mismatch and the elevation profile of the radiation pattern, which we characterized in the anechoic chamber for isolated (no drone, antenna only) and drone-mounted scenarios.

We first analyze results from the vertically-oriented receivers (VD-VD) (Fig. 3.6(b)) to understand the effect of elevation on RSS between two UAVs when the antennas used are identical with matched orientations (vertical). We can see that the two receiving antennas undergo the same behavior versus the elevation angle. The received signal level increases from around -87 dBm to -67 dBm (20 dB increase) when the receiving drone moves from $-56.3°$ to $0°$ elevation angle. Then, as the drone moves higher (from $0°$ to $+56°$ elevation), the received signal level decreases from -67 dBm to -85 dBm (18 dB decrease), until it reaches around -91 dBm as it reaches exactly above the transmitting drone ($+90°$). When this receiving drone moves to the $-90°$ elevation location (right below the Tx drone), an average RSS level of -97 dBm is reported. This trend is observed for all vertically-oriented receivers.

We conclude here that in an air-to-air links where two drones have the same antenna types and orientation, *movement of the receiving drone at different elevation angles can reduce the signal level by up to 30 dB.* This 30 dB difference in RSS can be crucial when designing algorithms for optimal drone placement [40]. Similar findings in cellular to UAV and air-to-ground scenarios were reported in [4,6]. However, in addition to not covering air-to-air links, the proximity of the receiver or transmitter to the ground in both studies makes it difficult to isolate the elevation factor from multipath and the surrounding environment.

Furthermore, the nature of drone movement in 3D space and the low RSS levels measured by vertical antennas at $\theta_{elev.} = |90|°$ motivate us to employ polarization diversity [41] that is represented by using two co-located orthogonally-oriented antennas. If we look at Fig. 3.6, where we implement a horizontally-oriented (H) receive antenna in addition to a vertically-oriented (VD) antenna, we can see that although VD results in higher RSS values throughout most elevation angles, around $+56°$ the RSS for the H receiver starts to increase, where lower RSS values for the VD receiver are measured. For example, at exactly $+90°$, H is reported to

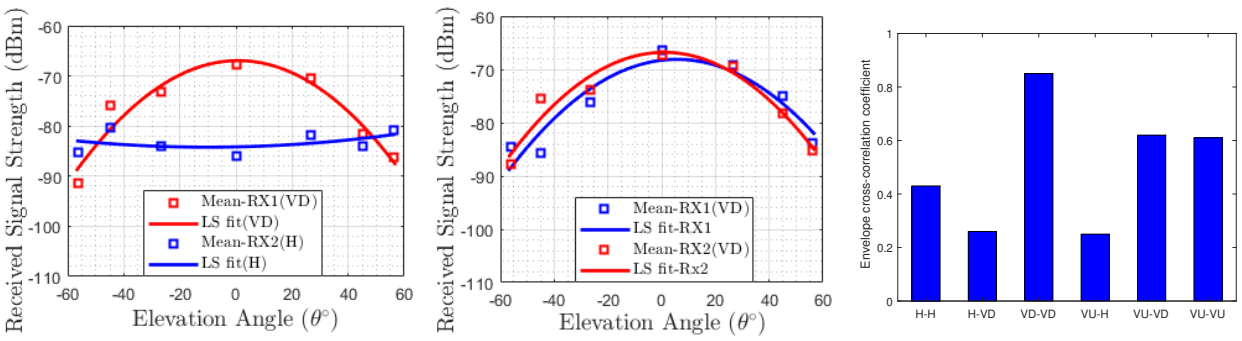

(a) (b) (c)

Figure 3.6: Average RSS vs. elevation angle for two different antenna orientation combinations: (a) H-VD and (b) VD-VD. Correlation coefficient for the received signal envelope in the 1×2 drone-based system with different antenna orientations (c).

measure an average RSS value of -85.8 dBm, where VD results in an average RSS of -98 dBm (approx. 12 dB higher RSS at H). In another example (VU-H experiment) the H antenna captures 20 dB higher average RSS compared to the VU antenna.

3.3.3 Antenna Placement, Orientation and Correlation

Since the orientation and spacing of two co-located receiving antennas can greatly affect the correlation and consequently the capacity of a MIMO system, we analyze the cross-correlation coefficient of the received signal at the two receiving branches in all of our six experiments. Since reasonable diversity gains can be achieved in multiple antenna systems that have a correlation coefficient less than or equal to 0.7 [34], it is useful to analyze the correlation between the two receiving antenna elements in all of the six different antenna orientation combinations. In doing so, we see how our antenna spacing decision of $\frac{2}{3}\lambda$ compares against what has been studied in literature and provide recommendations on antenna placement and polarization decisions. The correlation coefficient between the two received signal envelopes is calculated according to [34]:

$$\rho_{i,j} = \frac{\sum_{n=1}^{N}(r_i - \overline{r_i})(r_j - \overline{r_j})}{\sqrt{\sum_{n=1}^{N}(r_i - \overline{r_i})^2}\sqrt{\sum_{n=1}^{N}(r_j - \overline{r_j})^2}} \tag{3.1}$$

Here, N is the total number of samples, and $\overline{r_i}$ is the mean value of the fast-fading signal

envelope r_i, which corresponds to the first antenna orientation. The term r_j corresponds to the second receiver's antenna orientation. For example, $\rho_{h,vd}$ is the correlation coefficient between the signal envelopes of the H and VD antennas in the H-VD experiment. We calculate this correlation coefficient for the signal envelopes received throughout the flight path mentioned above and find that, except for one antenna orientation combination (VD-VD), the correlation coefficient is found to always be less than 0.7. For example, the VU-VU and VU-VD experiments result in $\rho_{vu,vu} = 0.61$ and $\rho_{vu,vd} = 0.62$. Furthermore, the orthogonal antenna orientations (H-VD and VU-H) result in the lowest correlation coefficients (around 0.2) among all experiments, which can offer greater diversity gains. The correlation coefficient for the six antenna orientation combinations are shown in Fig. 3.6(c). *Using these results and based on the objective (diversity or multiplexing gains), researchers can make informed decisions when selecting antenna orientation and spacing for drone communications.* For example, if diversity gains are required, our results suggest that an antenna spacing of $\frac{2}{3}\lambda$ on drones using VU-H, H-VD, VU-VD, H-H, and VU-VU antenna orientation might be sufficient for reasonable gains in UAV-to-UAV networks .

3.3.4 Elevation Impact on SNR Improvements for Different Antenna Orientations

We now analyze the effect of elevation on the SNR improvements that can be achieved by selection diversity in all of the six experiments. The SNR improvement over a reference branch i at an elevation angle θ is defined here (in dB) as the expected value of the difference between the selected (maximum) SNR in the 1×2 setup over the reference branch. It is given by:

$$\gamma_i^\theta = \mathbb{E}[SNR_{1\times 2}^\theta - SNR_i^\theta] \tag{3.2}$$

The results of SNR improvements in the VU-H experiment are plotted in 3.7. In this figure, γ_H and γ_{VU} are the SNR improvements over the H and VU antenna orientations, respectively. We can see that a higher SNR of 20 dB can be achieved around 0° elevation due to the VU antenna orientation (γ_H is higher) which matches the orientation of the transmit antenna. In contrast, around 18.5 dB SNR improvement can be achieved around +90° elevation by the H orientated antenna (γ_{VU} is higher) due to its radiation pattern main lobe being directed toward the transmit antenna as opposed to the null created by the

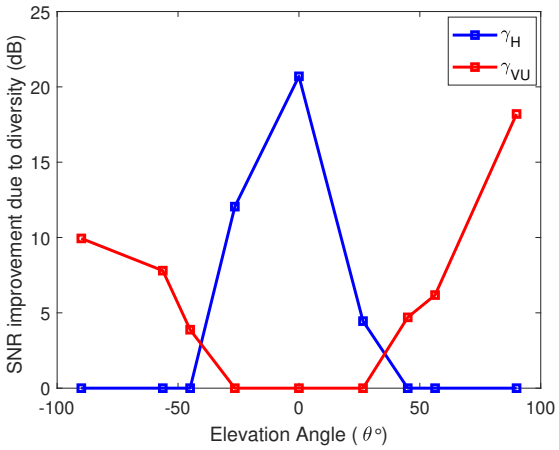

Figure 3.7: SNR improvement due to diversity in VU-H setup.

Table 3.3: SNR improvement (in dB) due to diversity: improvement is with respect to branch 1 (γ_1) and branch 2 (γ_2)

γ_i(dB)	**VU-VU**	**VD-VD**	**VU-VD**	**H-H**	**H-VD**	**VU-H**
$\gamma_1(max)$	2.1	6.3	4.0	8.8	16.1	18.2
$\gamma_1(avg)$	2.1	1.1	1.7	4.3	4.5	5.6
$\gamma_2(max)$	9.6	8.5	8.7	0.3	11.5	20.7
$\gamma_2(avg)$	5.5	1.90	2.4	0.3	2.18	4.13

vertical antenna.

The SNR improvement over the first and second branch in each experiment are summarized in Table 3.3. We can clearly see that SNR improvements vary according to the different antenna orientations and that cross-polarized setups result in larger overall gains.

From these results, we conclude that having cross-polarized antennas when drones move in three dimensions is important, especially at angles above/below 45° because of polarization mismatch losses. Measured improvements in SNR values of 20 dB can be achieved using cross-polarized receiving antennas.

3.4 Ground-to-UAV Channels in 3D Space

In addition to communicating with other aerial vehicles, UAVs might simultaneously communicate with or serve users/nodes on the ground. To further enhance our understanding

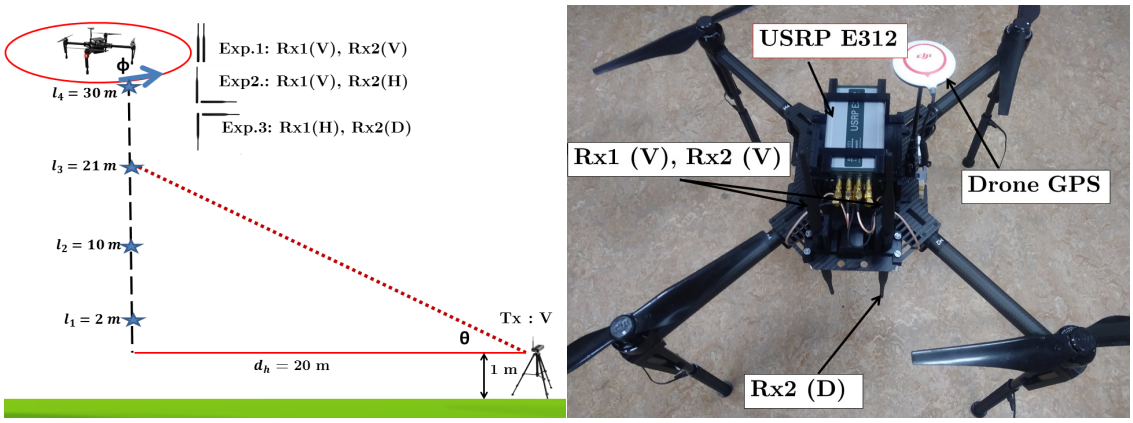

(a) (b)

Figure 3.8: (a) GtD Experiment setup and hovering locations for the Rx drone. (b) Rx drone structure and the mounted V and D antennas.

of the role of antenna orientation, UAV body, and elevation angle, in UAV-based channels, we conduct another set of experiments and investigate how these factors can impact UAV-to-ground channels at ultra low altitudes (around 30 m). We then model the impact of the UAV body as a function elevation and azimuth angles and show that prediction of angle-dependent loss in UAV-to-ground links becomes more accurate with the proposed model. Finally, we analyze small-scale fading for both UAV-to-UAV and UAV-to-Ground channels to first isolate the ground impact and focus on how antenna orientation can affect such channels.

3.4.1 Experiment Procedure

The experiment procedure is illustrated in Fig. 3.8. The transmitter is located on the tripod at a height of 1 m above ground level. The receiving drone is positioned at a fixed horizontal distance of $d_h = 20$ m. The drone navigates to each point of interest and hovers there while directly facing towards (and away from) the transmitter. The drone maintains a stable hovering position at each location for 20 seconds per heading direction. As the drone ascends in altitude, different elevation angles are realized by $\theta = \arctan(l/d_h)$, where l is the altitude of the drone with respect to the transmitter.

At each hovering location, I/Q samples are collected for both RF chains for the facing

and facing-away directions. By leveraging the log files generated by the shell and python scripts that we implemented on the USRPs, we are able to accurately match the timestamps of the received data to the location and direction of the drone. Sensor measurements are used in the offline processing of the received samples, where we splice the dataset according to time, altitude, heading direction, and GPS location. Three (3) experiments are carried out: V-VV, V-VH, and V-HD. The first letter is the transmitter's antenna orientation, and the second two letters are, respectively, the orientations of the first (antenna position 1) and second (antenna position 2) receiving antennas. V, H, and D are, respectively, vertical up, horizontal, and vertical down. Fig. 3.8 depicts the antenna setup at the receiver for the V and D orientations. The H orientation is shown in Fig. 3.1. In the V-VH experiment, H is in position 2. In the V-HD experiment, H is in position 1. We refer to a Tx-Rx link in an experiment as VX where V is the transmitter orientation (which is always V), and X is the receiver orientation.

3.4.2 Effect of Elevation Angle on Ground-to-UAV Channels

Before we characterize the impact of drone rotation at different elevation angles (*i.e.*, θ), we first investigate the impact of elevation on the received signal for vertical and horizontal antenna orientations. Using the developed angle-dependent models, with $|G_{VV}| = cos^2(\theta)$ and $|G_{VH}| = cos(\theta)sin(\theta)$, we analyze the measured and predicted values of this loss as the drone hovers at different elevation angles from the ground.

The angle-dependent loss for V-VH and V-VV experiments is shown in Fig 3.9. We notice that experiment results closely follow our analytical models. For the vertically-oriented antenna (VV links), loss is minimum at 3° elevation. The loss increases as the drone flies to higher altitudes. The increase in loss is due to gain misalignment of the mounted antennas in addition to the distance impact. This behavior is consistent and can be seen in all vertically-oriented receivers: see Fig. 3.9(b) and the VV loss in Fig. 3.9(a).

However, the results are different for the horizontally-receiving antenna (VH links). We see that the highest loss is recorded at 3° elevation. Then, as the drone moves to higher altitudes (30° to 45° range), this angle-dependent loss gets smaller. Then, the loss goes up again at $\theta = 55°$. This behavior can be better understood based on the analytical models

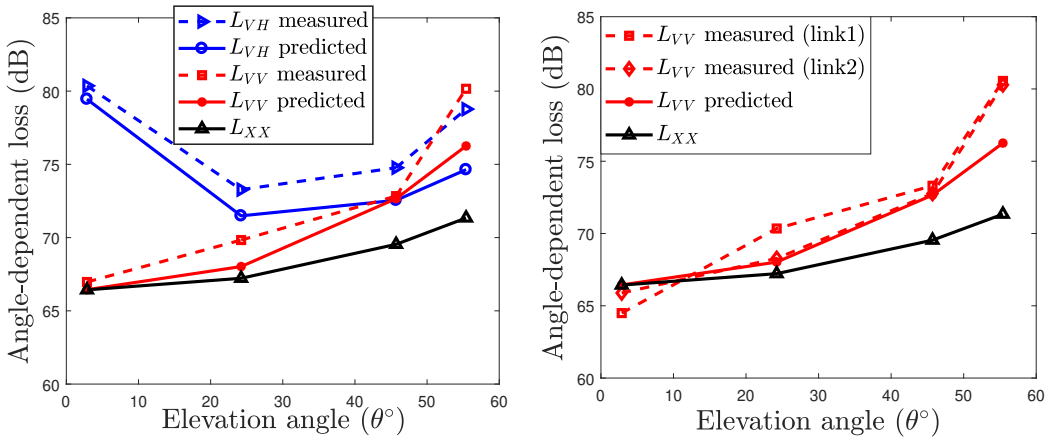

Figure 3.9: Measured and predicted values of the angle-dependent loss for the (a) V-VH and (b) V-VV experiments.

that we developed. The measured values shown in these graphs are the difference between the transmitted power and the average received power when facing the transmitter.

The facing-away scenario will be dealt with separately. The predicted values are given by L_{VV} (equation (2.13)) for the VV link and L_{VH} (equation (2.14)) for the VH link. Here, the standard deviation of the shadowing parameter is chosen to be $\sigma_s = 2$ dB. Although the exact shadowing value might vary in different situations, based on numerous experimentation over multiple years, we found that a 2 dB value to be appropriate. The body-induced loss ($\Gamma_\phi(\theta)$) is assumed to be 0 dB. This body-induced loss will be a contributing factor when the drone is facing-away from the transmitter. The assumption here is that since the antennas are mounted near the edge of the drone, the elevation radiation pattern when facing a node is unaltered and can be modeled as above. We see that the angle-dependent models, because of their inclusion of the proposed radiation pattern models, capture the measured values of the angle-dependent losses to a good extent. In contrast, predictions provided by L_{XX}, which is simply the free-space path loss in addition to shadowing, is shown to be the least accurate due to its exclusion of the important radiation pattern effects.

Another observation is that around 45° elevation, we can see that VV and VH links exhibit similar losses, although cross-polarized. This effect can be explained if we equate

G_{VV} to G_{VH} and solve for θ, which would give us an angle of $\theta = 45°$. We refer to this as the cross-over angle, the angle at which a flip occurs in antenna gain product for VV and VH links. Fig. 3.10 illustrates the antenna gain product for the two links. We see that before this angle, VV links experience higher antenna gain product. However, after this angle, VH links have the higher antenna gain product, consequently resulting in lower angle-dependent loss values. This dependency on antenna gain product explains the behavior of the measured values and shows how understanding the radiation pattern of the used antennas is of paramount importance in drone-based links since significant differences can occur with minimal distance variations. In fact, when we measure the received signal at an elevation angle of $\theta = 90°$ (*i.e.*, the Rx drone directly above the transmitter, with a vertical separation distance of 20 m), we record a stronger signal of up to 20 dB greater for VH links compared to VV links [11].

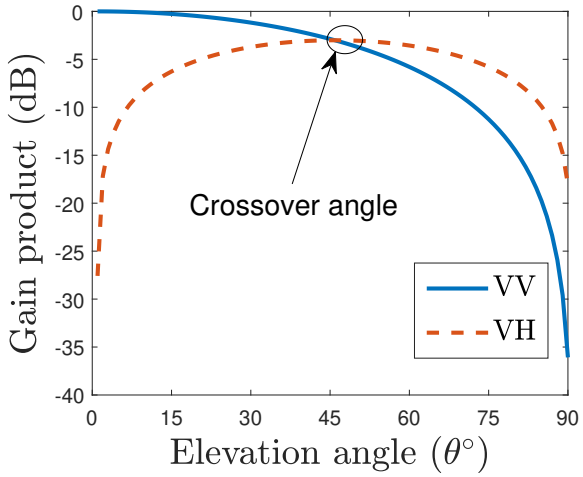

Figure 3.10: Antenna gain product for VV and VH links and the crossover angle.

3.4.3 UAV-Induced Shadowing in 3D Space

Before quantifying the losses induced by the drone body, we analyze the shadowing caused by the drone body. Shadowing describes received signal fluctuations around the mean signal as the receiver changes its location, consequently experiencing different surrounding environments and objects in the signal's path [12]. Here, the cause of shadowing is completely

different: it is exclusively due to the drone body. While many other works have investigated elevation-dependent shadowing in UAV channels [4,26,42], the emphasis was on the conventional shadowing caused by the surrounding environment. In addition, the effect of drone rotation on shadowing at various elevations is never addressed. For example, Akram *et. al* has proposed an elevation-dependent shadowing model as the UAV moves to higher altitudes away from buildings in urban environments [4]. Until now, little is known about how shadowing is affected solely by the drone body at various elevations and for different antenna orientations. Through the above explained LOS experiments, we evaluate the shadowing based on drone rotations.

The parameter that describes shadowing (*i.e.*, ξ_s) is usually modeled in empirical path loss models as a zero-mean, Gaussian random variable with a standard deviation of σ_s (*i.e.*, $\mathcal{N}(0, \sigma_s)$ [12]). The question is: if nothing else surrounding the drone is changing, does the drone body result in a different shadowing at slightly different elevation angles? We will find that the answer is yes. To analyze this drone-induced shadowing, the mean RSS per hovering location is subtracted from the instantaneous values for the two cases of facing and facing-away from the ground transmitter.

Effect of Drone Rotation with Vertical and Horizontal Antennas. First, we notice that, in general, significantly higher shadowing occurs when facing-away from the ground transmitter compared to when facing it. When facing the transmitter (*i.e.*, $\phi = 0°$) and across all elevation angles for all antenna setups, shadowing does not exceed 4 dB with a standard deviation never exceeding $\sigma_s = 2$ dB. On the other hand, when facing-away from the transmitter (*i.e.*, $\phi = 180°$), shadowing can reach up to 9 dB with a standard deviation of up to $\sigma_s = 6.36$ dB, an increase of 4.3 dB in standard deviation.

Second, we describe an interesting finding: when facing away from the ground transmitter, shadowing increases with elevation for all VV links. For VH links, however, this dependency is not observed. Fig. 3.11 shows the measured shadowing for the VV and VH links in the V-VH experiment. In Fig. 3.11(a) at 55° elevation, more shadowing (reaching up to 9.8 dB) is measured compared to 23°, at which shadowing does not exceed 2.5 dB. In Fig. 3.11(b), we find that the measured shadowing for the VH link does not change with elevation. The standard deviation of the measured shadowing parameter for facing-away ver-

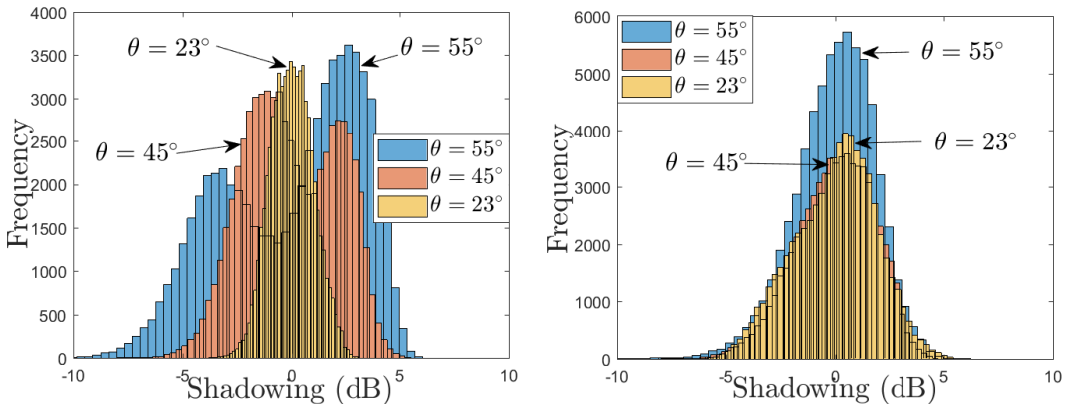

Figure 3.11: Measured shadowing for (a) VV and (b) VH links when facing-away ($\phi = 180°$). Higher elevations lead to higher body-induced shadowing in VV links.

tical and horizontal Rx antennas is shown in Fig. 3.12. For the vertically-receiving antennas, Fig. 3.12(a), we find that σ_s increases with elevation for values in the range of 1 dB at $\theta = 3°$ to approximately 6 dB at $\theta = 90°$. This phenomena can be explained by how the antennas are placed on the side of the drone body: as the drone flies to relatively higher elevations and because it is facing away from the transmitter, more of the drone body obstructs the signal's path before it reaches the receiving antennas. However, since our horizontal antennas are mounted outwards of the body (see Fig. 3.1), the blockage they experience from the body is the same regardless of elevation. This can be seen in Fig. 3.12(b), where the standard deviation barely changes with elevation.

Effect of Diverse Antenna Positions for Same Orientation. Finally, for the same antenna orientation, different locations on the drone do not change the standard deviation of the shadowing parameter. For example, in the V-VV experiment, the average standard deviation of the V antenna in position 1 is $\overline{\sigma_s} = 1.38$ dB, while the V antenna in position 2 experiences a value of $\overline{\sigma_s} = 1.40$ dB. The vertically-down (D) antenna experiences similar shadowing to the V antenna with an average standard deviation of $\overline{\sigma_s} = 1.46$ dB. Here, average refers to the mean over all elevation angles.

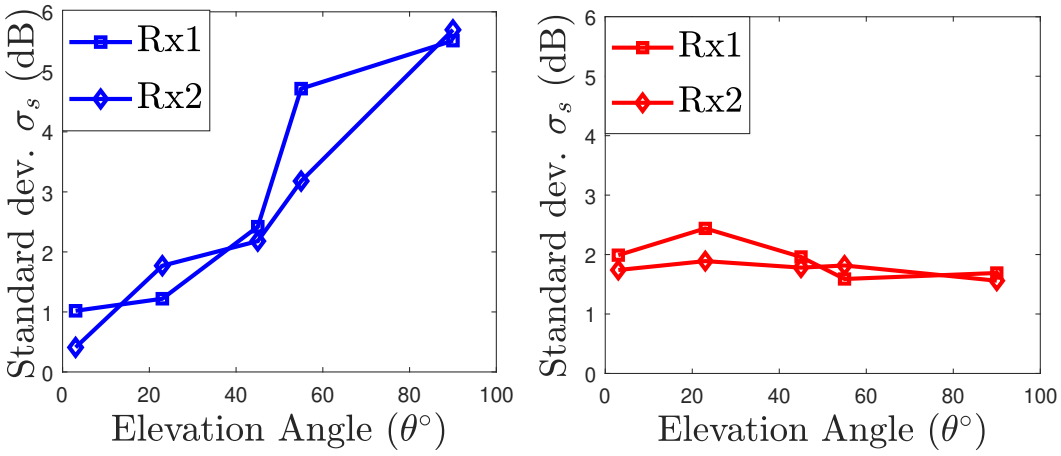

(a) Vertical Antennas

(b) Horizontal Antennas

Figure 3.12: Measured shadowing standard deviation (σ_s) at different elevations for the scenario of facing-away from the ground Tx. (a) σ_s for vertically mounted antennas. (b) σ_s for horizontally mounted antennas. Rx1 and Rx2 refer to antenna positions 1 and 2, respectively.

3.4.4 Modeling the Impact of Drone Rotation

Through our anechoic chamber measurements, we have seen that the drone body and its rotation can result in considerable variations in the azimuth radiation pattern of the mounted antennas, introducing reductions in received power of up to 10 dB at some azimuth angles. This issue is worth investigating via in-field experiments, where we can also study the impact of elevation on this rotational loss. As explained in Section 3.4.1, at each hovering location, the drone is rotated 180°, facing away from the ground transmitter, and the received I/Q samples are recorded for a period of 20 seconds. We analyze the effect of this rotation on the average RSS at every elevation angle and propose a model that captures this rotational loss. The conclusion reached is that this rotational loss is elevation-dependent for vertically-mounted antennas.

We define the average rotational loss per elevation angle per link as the difference in average RSS between the facing ($\phi = 0^\circ$) and facing-away ($\phi = 180^\circ$) measurements. The rotational loss, $\Gamma_\phi(\theta)$, can be calculated as $\overline{RSS}(\phi_0, \theta) - \overline{RSS}(\phi_{180}, \theta)$, where ϕ_0 indicates facing, and ϕ_{180} indicates the direction of facing-away from the Tx. We calculate this value

Table 3.4: Fitting parameters of the rotational loss model

Experiment	**Link**	**Rx Ant.**	μ	β	**RMSE**
V-VV	*VV*	1	0.0463	1.4768	0.814
V-VV	*VV*	2	0.0448	1.8769	0.4267
V-VH	VV	1	0.0822	1.5628	0.4195
V-HD	VD	2	0.0978	0.7583	0.9386

for all VV experiments and find that it is elevation-dependent with higher elevations leading to higher $\Gamma_\phi(\theta)$ values. This result can be explained by the same intuition described in Section 3.4.3, where more of the drone body starts to obstruct the receiving antennas at relatively higher elevations.

We plot this rotational loss for all VV links in Fig. 3.13 and see that this factor can increase from a range of 1 to 2.5 dB at $\theta = 3°$ to the range of 5 to 7.5 dB at $\theta = 55°$. A linear regression line that fits the average measured values as a function of elevation angle was created, and the results of this fitting for all VV links are shown in the same figure. In Fig. 3.13, links 1 to 4 represent the vertical links in the V-VV (twice), V-VH, and V-HD, experiments, respectively. It is not shown here, but, we additionally investigated another elevation angle where the drone is exactly above the ground transmitter (*i.e.*, $\theta = 90°$), and, intuitively, rotation seemed insignificant. In other words, no change in average RSS was observed. Moreover, no specific trend was observed for the VH links, as the rotational loss is approximately constant with a value around 2 dB across the investigated elevation angles.

For the VV links, the model that describes the elevation-dependent rotational loss Γ (in dB) as a function of the elevation angle, θ, can be described as:

$$\Gamma_\phi(\theta) = \mu\theta + \beta \tag{3.3}$$

Here, μ is the slope of the straight line, β is the intercept, and θ is the elevation angle between the ground Tx and the drone Rx. The values of these parameters for all vertical-to-vertical links are summarized in Table 3.4.

We now quantify the benefit of including this rotational term in predicting the angle-dependent loss. The results of the measured and predicted values for L_{VV} of the VV link in

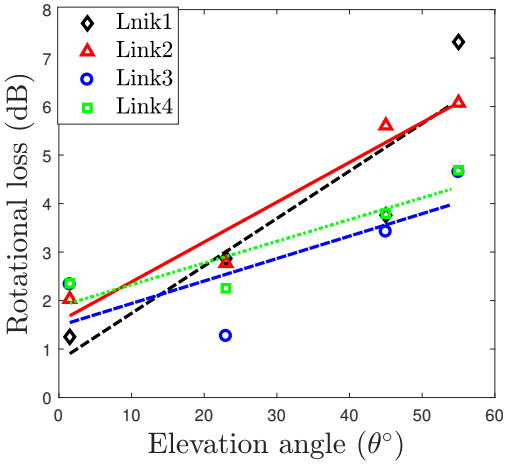

Figure 3.13: Rotational loss and its linear fit representation $\Gamma_\phi(\theta)$.

the V-VH experiment are shown in Fig. 3.14. In this figure, we have 4 results: (*i.*) L_{VV} is measured at $\phi = 0°$, which is simply the average measured loss (difference between transmit power and average received power for 20 s) at the corresponding elevation angle when the Rx drone is facing the ground Tx. (*ii.*) L_{VV} is measured at $\phi = 180°$ with the drone facing-away from the Tx, which is clearly larger due to the drone body. (*iii.*) A prediction is produced by using L_{VV} excluding $\Gamma_\phi(\theta)$), which is the result of predicting this angle-dependent loss using equation (2.15) but without the above-modeled rotational loss. In other words, it excludes the rotational loss (*i.e.*, $\Gamma_\phi(\theta) = 0$ dB). (*iv.*) Finally, we have the prediction using L_{VV} including the average value of the rotational loss, $\Gamma_\phi(\theta)$, which is predicted using the above model (equation (3.3)).

First, we can see that only using the elevation radiation pattern provides good prediction when facing the Tx. However, to predict the angle-dependent loss when facing-away from the Tx, a significant underestimation in the link budget of up to 11 dB can occur. An example of this error can be seen at an elevation angle of 55°, where we predict 75 dB of average link loss, but it is actually 86 dB. This error is due to the fact that this model, as in many other drone-related works [6,18], neglects drone rotation and antenna placement effects. Therefore, we recommend including this body-induced rotational factor when predicting drone-based links that involve drone rotation at different elevation angles.

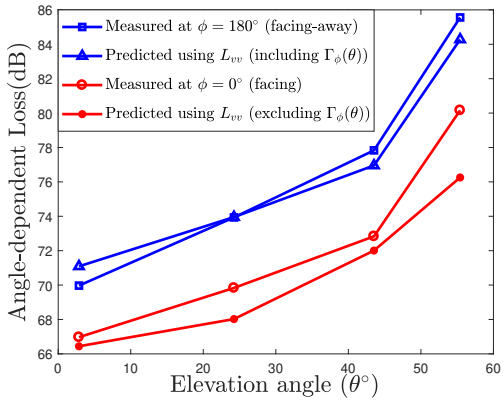

Figure 3.14: Impact of using $\Gamma_\phi(\theta)$ on predicting the angle-dependent loss when a drone is rotated 180° at different elevation angles.

Introducing the body-induced rotational factor into predicting angle-dependent losses would result in a more accurate capturing of the average (large-scale) behavior of drone-based links. For example, in the above discussed link, the average absolute error of our prediction is 0.89 dB. However, if we use a conventional model that excludes the rotational loss, the average error is 6.11 dB. As a result, our model is 85% more accurate because of the drone-body inclusion. The limitation of this model, however, is that it is only valid for the case of LOS ground-to-drone channels with no surrounding buildings, where the impact of the body is prominent. However, many applications can find this model useful including but not limited to smart agriculture systems, where ground nodes send data to a collector drone that hovers in a certain direction. In such a scenario, the transmit power can be carefully designed to compensate for the above Γ_ϕ effects.

3.5 Small-Scale Fading For UAV-based Channels in 3D Space

In this section, we study how the orientation of multiple drone-mounted antennas can affect small-scale fading severity. The effects are measured in terms of the Rician K-factor and are investigated for polarization-matched and cross-polarized GtD links. Furthermore, to focus on the role of the mounted antennas and not confuse it with that of ground-induced fluctuations, we quantify the impact of ground reflection on the Rician K-factor via another set of DtD experiments at high altitude, where the effect of ground reflections are minimal.

We then compare the Rician K-factor values to those obtained in the GtD experiments. Lastly, to determine the impact of our antenna placement decisions on possible diversity gains, we analyze the correlation coefficient at all elevation angles for both heading direction scenarios (facing and facing-away) and make recommendations that could lead to the efficient design of drone-based networks.

3.5.1 K-factor in 3D Ground-to-Drone Channels

We analyze the instantaneous received signal envelope recorded at both RF chains for three GtD experiments. We include a unique elevation angle, where the receiving drone hovers above the ground transmitter at an angle of 90° with a vertical distance of 10 m. This angle was examined to demonstrate the impact of extreme elevation as opposed to the $\theta = 3°$ angle. An example of how the measured LOS channel follows a Rician distribution is shown in Fig. 3.15, where a histogram of 3000 samples (a time period of 93.7 ms) of the instantaneous received signal is plotted. Then, a Rician distribution is fitted to the measurements using the maximum-likelihood estimate (MLE). In this figure, we can see that higher K values (17.7 and 9.6 dB) are obtained for VV links compared to the VH links (6.5 and 3.6 dB) at 3° and 23° elevations, respectively. It is worth mentioning that the Kolmogorov–Smirnov test was performed to compare our measurements to the fitted Rician distribution. The results of this comparison indicated that we accept the null hypothesis that the two sample vectors (measurements and fitted distribution samples) come from the same distribution. This is true for the investigated elevation angles of 3°, 23°, 45°, and 55°.

In general, our results indicate that the K-factor is strongly dependent on the elevation angle for polarization-matched VV links since it can change by as much as 15 dB, whereas it is approximately flat for the VH link across all elevation angles. For example, refer the GtD results in Fig. 3.16(b), where each point (indicated by blue squares) represents the average of six values of the K-factor of the VV link. We see that the strongest K values are recorded at 3° with a range of 13-15 dB. However, after this angle, as the drones moves to higher altitudes, the K-factor starts to decrease, reaching approximately 4 to 5 dB at $\theta = 55°$. This reduction can be explained by the analytical models developed above, where the radiation pattern product becomes weaker as the receiving drone moves to higher elevations. At 90°

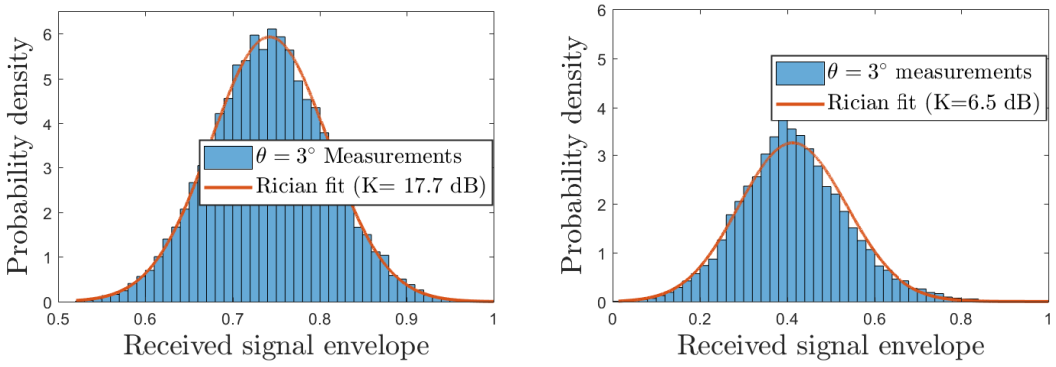

(a) VV at $\theta = 3°$

(b) VH at $\theta = 3°$

(c) VV at $\theta = 23°$

(d) VH at $\theta = 23°$

Figure 3.15: Measured received signal envelope for VV and VH Ground-to-Drone links and its Rician fitting.

elevation (*i.e.*, the Rx drone hovers above the ground Tx), the K factor becomes almost 0 dB, indicating an extremely weak LOS component.

For the VH link (Fig. 3.16(a)), this strong elevation dependency is not observed. The K-factor is nearly constant because of the low variation in the radiation pattern product over a wide range of elevation angles (shown in Fig. 3.10). However, since our GtD experiments are conducted close to the ground, the impact of fluctuations caused by the ground needs to be understood so that we can isolate the impact of drone-mounted antenna position/orientation on small-scale fading. To quantify these ground effects, we analyze another set of results from DtD experiments that we carried out in the same geographical location but at altitudes where no surrounding objects exist, and the ground is at least 80 m below the drone (*i.e.*, the effect of ground reflections is weak).

3.5.2 Ground-to-Drone vs. Drone-to-Drone K-factor

To investigate the impact of the ground on the Rician K-factor, we conduct a set of DtD experiments that matches the GtD experiments. We then calculate the K-factor at the same elevation angles. The experiments are conducted at 80 to 110 m altitude, where the environment is free of reflecting objects, and the two drones are facing each other. The DtD experiment is shown in Fig. 3.5(a). The Tx drone is fixed at its hovering location at 80-m altitude, where the Rx drone is automated to fly at locations that would result in approximately the same elevation angles as in the GtD experiments. Similar to Section 3.5.1, we conduct three experiments: V-VV, V-VH, and V-HD.

We calculate the K-factor and report this finding. At 3° and 23° elevation angles, the K values from the DtD experiments are always stronger than those obtained from the GtD experiments. For example, in Fig. 3.16(b), we see at 3° to 23° elevation, the DtD K-factor can reach values of up to 24 dB, which is 10 dB higher than that of the GtD experiments. As the elevation angle increases, however, this difference starts to diminish, indicating a lesser role of the ground than that of the actual hovering drone and its mounted antennas. To further understand the impact of the ground on the K-factor, consider Fig. 3.16(c)-3.16(d) as an example. Here, the CDF of measured σ, the parameter that describes the reflected/scattered components is plotted. We can see that it is definitely higher in the GtD experiments than

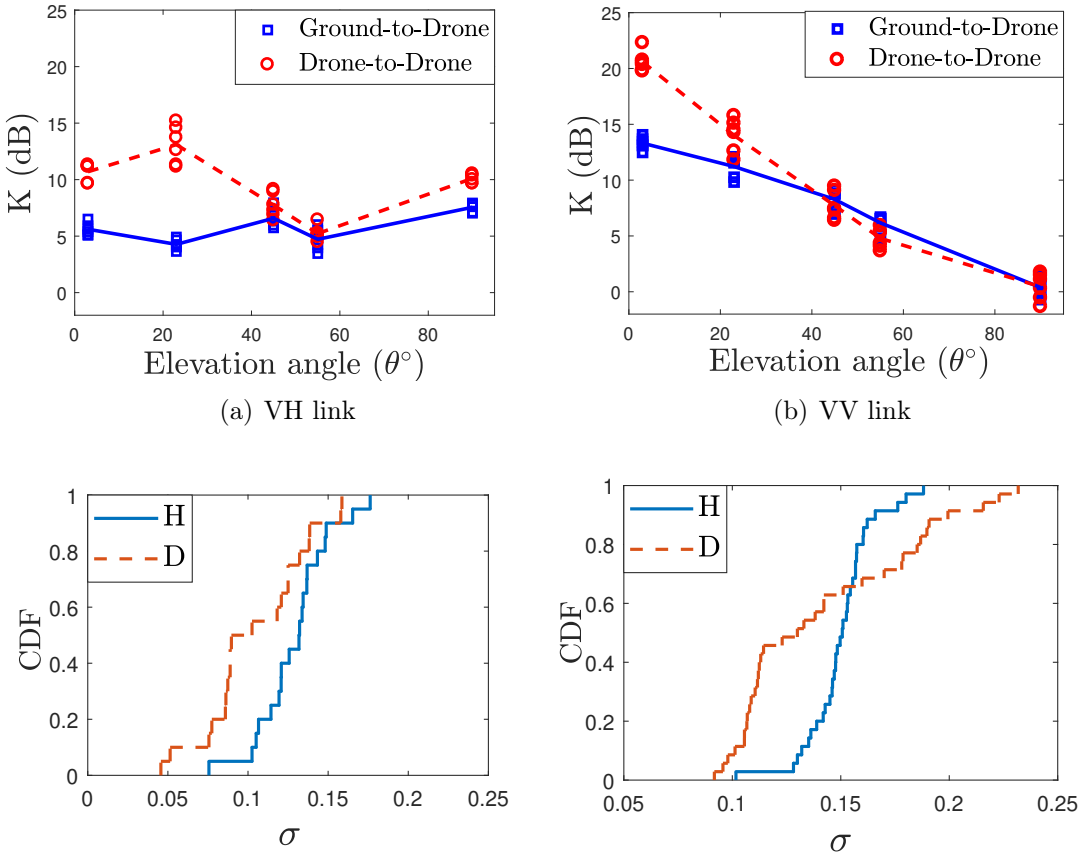

(a) VH link

(b) VV link

(c) DtD scattering parameter

(d) GtD scattering parameter

Figure 3.16: (a) The K-values for the VH link. (b) The K values for the VV link. The empirical CDF of σ for the V-HD experiment in the GtD and DtD scenarios is shown in (c) and (d), respectively.

Table 3.5: Rician K-factor For VV and VH Links in GtD and DtD Experiments

Ground-to-Drone K (dB)					
Link	$\theta = 3°$	$\theta = 23°$	$\theta = 45°$	$\theta = 55°$	$\theta = 90°$
VV	13.31	11.21	8.27	6.16	0.37
VH	5.61	4.27	6.58	4.71	7.55
Drone-to-Drone K (dB)					
Link	$\theta = 3°$	$\theta = 23°$	$\theta = 45°$	$\theta = 55°$	$\theta = 90°$
VV	20.60	14.03	7.75	4.78	0.45
VH	10.69	13.09	7.75	5.22	10.10

in the DtD experiments. For example, 40% of measured values are greater than 0.15 in the GtD experiment, as opposed to 20% in the DtD experiment. If we assume a fixed-LOS component, a higher σ results in a lower K, as is happening at altitudes close to the ground. The measured K-factor values for VV and VH links in the GtD and DtD experiments are summarized in Table 3.5.

It is worth mentioning that while previous works have analyzed the Rician K-factor variations with drone height [26, 43], the nature of the environment in those experiments makes it difficult to isolate radiation pattern and antenna orientation effects from the impact of the actual obstructions and reflectors in the signal's path. In this study, these K variations are solely due to the antenna location/orientation and drone proximity to the ground, not induced by the surrounding environment (*e.g.*, buildings, trees, and cars).

3.5.3 Correlation and Diversity Gains in 3D GtD Channels

As future drones might be expected to carry large number of antennas for a variety of applications, a thorough analysis of the impact of antenna orientation, spacing, and 3D placement on correlation and diversity gains is critical. Here we calculate the correlation coefficient between the two received signal envelopes of each antenna setup and analyze the results, which are summarized in Table 3.6.

First, we notice that the envelope correlation coefficient between the two receiving antennas in the facing Tx scenario is highest at 3° elevation, even for the cross-polarized setup. Then, correlation decreases as the elevation angle increases. At 55° and 90°, correlation becomes slightly negative for the cross-polarized setups, indicating the increase of the re-

Table 3.6: Correlation Coefficient Vs. Elevation Angle

Facing Tx ($\phi = 0°$)			
θ	$\rho_{v,h}$	$\rho_{v,v}$	$\rho_{h,d}$
3°	0.45	0.43	0.63
23°	0.32	0.35	0.25
45°	0.3	0.21	0.19
55°	-0.22	0.1	-0.15
90°	-0.08	0.1	-0.3
Facing-way from Tx ($\phi = 180°$)			
θ	$\rho_{v,h}$	$\rho_{v,v}$	$\rho_{h,d}$
3°	0.34	0.33	0.43
23°	0.08	0.19	0.16
45°	0.5	0.06	0.45
55°	0.14	0.02	0.1
90°	0.22	0.14	0.06

ceived signal envelope (horizontal), while the other (vertical) decreases. When the drone is facing away from the transmitter, $\phi = 180°$, no specific trend is observed. Interestingly, even though our experiments are in perfect LOS, we report that for all antenna setups, at all elevation angles and for both azimuth directions, the correlation coefficient never exceeds 0.7. As a result, diversity gains can be achieved in the 9.5 to 11.5 dB range using Maximal Ratio Combiner (MRC) or Selection Combining (SC) in Rayleigh and Rician fading channels at an outage probability of 0.01. This is an important result due to the fact that diversity gains for a fixed outage probability would fall more rapidly at correlation values higher than 0.7 [44]. Given this result and our previous findings, we can conclude that in LOS Ground-to-Drone and Drone-to-Drone channels, an antenna spacing of 0.67λ (8 cm in this case) is a good design choice if diversity gains are of interest, regardless of antenna orientation.

Chapter 4

Characterization of The Human-induced Effects in UAV-to-Ground Line-of-Sight Channels

In many applications, UAVs might need to communicate with a device that is either being held or attached to a person at altitudes close to the ground. A person can be holding user equipment (UE) near their chest or in their pocket while downloading or uploading data. Moreover, the direction of the user relative to the UAVs can take on any arbitrary value. For example, a user could be texting (holding the UE near their chest with both hands) while facing the UAV or facing-away from it. Because of these different use cases, the wireless channel might go through dramatic changes [45, 46]. Consequently, the optimal placement decision of the UAVs, which targets, say, the highest achievable throughput or minimum energy consumption, could depend on the near-body location (near chest or in pocket) or user direction (facing or facing-away). Moreover, due to user-antenna interaction and the near-field coupling effects, antenna radiation patterns can be altered [7, 47], and significant variations in the received signal can be experienced by the user [48]. Similar effects can be observed in the case of facing a transmitter while holding a receiver with different grips and/or postures [49].

While the role of the human body and its effects on terrestrial wireless channels has been the focus of many works, the impact of the user-induced effects on UAV-to-ground[1] channels has been mostly disregarded in literature. The uniqueness of this case study comes from the ability of UAVs to adjust their position in 3D space based on the observed use case. Factors such as UE location and user orientation along with the UAV's 3D location and its antenna radiation pattern will have a considerable impact on the wireless channel, as we shall see in this work. In addition, simulation and optimization models, which constitute the majority of UAV-related work, do not consider such human-related factors. Therefore, measurement campaigns that target this issue are necessary.

[1] We use Air-to-ground and UAV-to-ground interchangeably

In this work, we investigate how three different use cases of holding a communication device, namely, near-chest facing (NCF), in-pocket facing (IPF), and near-chest facing-away (NCFA), can affect the UAV-to-ground channel at ultra-low altitudes (less than 30 m altitude). We measure and analyze how the average received signal strength (RSS), shadowing, and small-scale fading can be affected by the UAV hovering location, user orientation, and the UE near-body location. We target two carrier frequencies, 900 MHz and 2.5 GHz, both of which have many narrowband Internet-of-Things (IoT) based applications such as the IEEE 802.15.4 technology as well as broadband services. This is, to the best of our knowledge, the first study that measures and quantifies how the human body and user behavior can impact the UAV-to-ground channel at various drone locations. The conclusions presented here are the results of the thorough analysis of 108 dataset files spanning 18 different drone hovering locations, three different use cases, and two carrier frequencies. Our findings could help the aforementioned research efforts establish more realistic UAV-to-ground channel models that consider users on the ground. Adaptive algorithms, for example, that are designed to optimize drone mobility and network performance when communicating with ground UEs, such as [50], could find our work insightful.

The contributions of this chapter can be summarized as follows.

- We show that, compared to a baseline user-free (free-space) scenario, the existence of the human body near a UE can result in increased or decreased RSS levels, depending on the user's orientation. These user-induced "gains", or "losses" are found to depend on the frequency used and the UAV's hovering position.

- We demonstrate how the UAV's hovering position and user orientation can affect shadowing and multipath in ultra-low LOS UAV-to-Ground channels. We quantify their effect and show that, except for one drone hovering position at which the UAV's body dominates influence on the channel, shadowing, mutipath and the Rician K-factor strongly depend on the user body orientation, not the UAV's body nor its location.

- We show that, while moving the UE from near the chest to inside the pocket could lead to some degradation in channel quality, improvements could be achieved by simply readjusting the drone's hovering altitude. For example, if the transmitting UAV

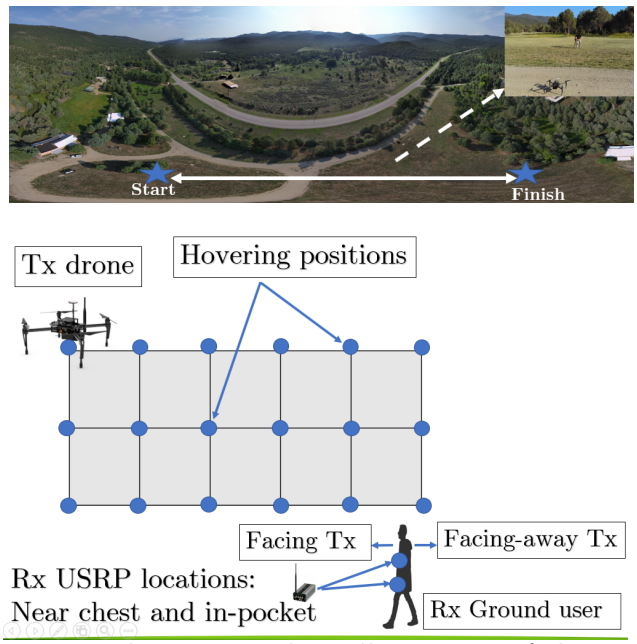

Figure 4.1: The experiment location and an illustration of the investigated use cases.

descends from 30 m to 10 m altitude after the UE is placed inside the pocket, the received signal level is improved by 7.5 dB on average. We explain how these improvements relate to the elevation radiation pattern of the antenna, traveled distance, and clearance from the UAV body.

- We address the time-varying nature of the K-factor as a result of UAV hovering and relative direction of the user. Then, we show that, except for one drone hovering position, the user's body could lead to significant degradation in the K-factor causing an average and a maximum reduction of 6.8 and 15 dB, respectively. Frequency comparison is then performed revealing that the K-factor at 900 MHz is stronger than 2.5 GHz across all use-cases.

- To highlight the impact of our findings, we propose two applications in which the obtained insight could be valuable for the case of a UAV-assisted soldier.

First, we allude briefly into the basic mechanisms of signal propagation through the human body. Then, we discuss literature related to the two main topics involved in this work.

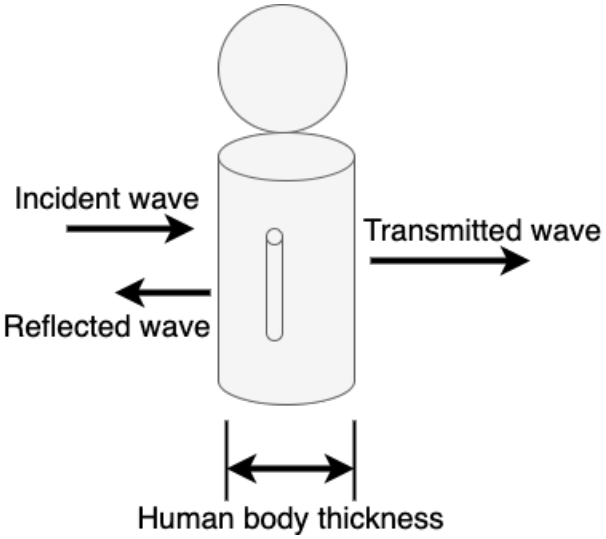

Figure 4.2: Illustration of how the body can affect signal propagation.

4.1 Propagation Through The Human body:

The human body absorbs and reflects electromagnetic energy. At the air-human interface, some energy will be reflected, depending on the refraction index or the intrinsic impedance, both of which are a function of the permeability and permittivity of the the human body tissues [51] which in turn are frequency dependent. Another part of the signal will penetrate through the body's multiple layers experiencing attenuation mainly due to absorption and multipath reflections within the tissues. Attenuation due to absorption and propagating through the human body is exponential with respect to the thickness of the body and has been shown to be the main contributor to electromagnetic energy loss with values reaching up to 35 dB [52]. The amount of attenuation due to absorption has been shown to considerably vary with frequency and the tissue thickness [51, 53], with visceral fat being the dominant tissue type in determining the loss. Finally, and after many reflections/transmissions within the body's many layers, the remaining part of the signal will leave the human body and propagates back into the air. A high level illustration of the propagation mechanics is shown in Fig. 4.2.

4.2 Related Work

We breakdown related literature into two main bodies of work. The first deals with human-based communications while the second studies UAV air-to-ground channels at low or ultra-low altitudes. *Human-Induced Effects*: The impact of the human body on the wireless channel has been the focus of many studies in literature. The human body as an antenna was investigated in [54] and the results showed that the human body could increase signal reception and that the reflection coefficient could be improved by different human body postures. The human body interaction with devices and its use as an antenna was leveraged in [55] into building a system that can recognize gestures. [48] Showed that the human body can significantly alter the effective radiation pattern of the antenna at 2.4 GHz. In addition, losses of up to 25 dB were found due to blockage from the human body. A similar finding of 21 dB loss at the same frequency was reported in [56]. In [45] an average loss of 20 dB was recorded due to covering a mobile device antenna by the hand. In [49], it was shown that the body of the user, when facing a transmitter at millimeter wave frequencies, can actually contribute to the radiation of the antenna and result in higher received signal levels compared to free-space scenarios. Similar finding was reported in [46] where four different frequencies were investigated for a user facing and facing-away from a ground transmitter. Variations in RF losses within the human body at two frequencies (403 MHz and 923 MHz) were investigated in [51]. The work in [53] investigated the impact of three different human body types on radiated power at 17 different frequencies. It was shown that at high frequencies gains, compared to free space, could be achieved. The work also highlighted how the radiated and absorbed power could vary with body type. It was shown that the RF transmission loss within the human body is higher at the lower frequency and that the results varied depending on the thickness of the tissues, especially the visceral fat. A study that investigates on-body communications for a wide range of frequencies (420 MHz to 2.4 GHz) and technologies was conducted in [57]. The impact of a user's head and hand on antenna radiation pattern at 880 MHz was studied in [45] and it was shown that user-antenna interaction can alters both the magnitude and phase of the antenna radiation pattern. Leveraging the strong multipath effects experienced within the body tissues, the work in [52] used signals with different frequencies to achieve beamfroming at a target placed

within the tissue of an animal. A machine learning approach that utilizes received signal strength to distinguish between different user modes at millimeter wave frequencies was proposed in [58].

UAV-to-Ground Studies: The work in [7], which targets the same issue investigated here, studies a UAV-to-Ground channel at ultra-low altitudes for three different environments and two user modes: texting and calling. Measurements and analysis were carried out for a limited drone path of 20 m with an emphasis on the impact of the environment on the channel rather than the human body. The work in [21] experimentally characterizes large-scale fading components in drone-to-ground channels where the ground node was mounted on a tripod. The work in [27] characterized the K-factor for low-altitude UAVs in urban environments crowded with buildings and spanned large horizontal distances. Channel characterization of wideband air-to-ground channels in different environments and for different frequencies was carried out in [5, 22]. Another AtG sounding method for millimeter wave channels was demonstrated in [17]. Autonomous QoS-driven UAVs in air-to-ground channels are prototyped and experimentally investigated for three ground devices, that were not held by humans, in [50]. The work in [40] demonstrated a UAV that can change its hovering location based on changes on the wireless channel that were induced by a user holding the device. However, the impact of the human body was not considered and the movement decisions were predefined.

While the above two bodies of work provide valuable insight, studies that bridge the gap between the two are still missing. This is what we attempt through our work. Specifically, our study provides an understanding of how the human body can influence such channels with various use cases and considering many UAV hovering positions and frequencies. We believe that although only considering the user and UAV might not be enough to fully understand all the intricate details of such channels, the ability to measure and characterize the relative impact is key into moving forward with more realistic channel models and algorithms that take the human body into account. Our findings can affect the design and deployment of adaptive UAV-based algorithms that target optimizing a certain wireless performance metric when actual ground users are considered. For example, in [50], if the UE was held by an actual user or placed inside their pocket, the SNR, trajectory, and likely the fairness index

might have been very different. Furthermore, the integration of the obtained user-induced effects into models that target the optimal deployment of UAVs, such as [16, 59], could lead to more realistic results. In [16], for example, where the capacity of a UAV-to-ground link is studied with two users on the ground, the near-body location of the UE and/or the user's direction relative to the broadcasting UAV could lead to altering the required transmit power from the UAV, consequently impacting its flying time and/or the network throughput. For these reasons, we believe that our findings could enhance the practical understanding of UAV-to-ground channels that consider the human body effects and help in the process of creating adaptive algorithms for drone deployments.

4.3 Experiment Setup

In this section, we present our hardware and software setup, then, we discuss the experiment procedures.

4.3.1 Hardware and Software Setup

Two of the Universal Software Radio Peripheral (USRP) E312s from Ettus Research™ are configured for collecting measurements. The transmitting radio is mounted on a tripod in the baseline ground-to-ground (GtG) experiments and on the UAV in the Air-to-Ground (AtG) experiments. The transmitting antenna is vertically mounted, oriented upward and is directly connected to the TRX port using an SMB to SMA adapter. The receiver USRP is either mounted on a tripod, such as the case in the user-free GtG and AtG experiments, or being held by the user, which is the case in the human-related experiments. Both radios utilize omni-directional, linearly-polarized antennas (Ettus VERT2450) with a radiation pattern in the azimuth and elevation planes as shown in Figs. 4.3(b) and 4.3(c). The transmitter is configured to send an unmodulated carrier at a sampling rate of 64 thousand samples/second. The receiver, sampling at the same rate, is configured to write the received IQ samples to a binary data file as complex floating point numbers. Measurements are recorded for a period of 20 seconds per hovering/Rx location. The processing and analysis is conducted over the middle 15 seconds to ensure the exclusion of the unwanted drone transition effects that might occur when the UAV is coming to or moving from the desired location. The absolute value of the complex envelope is then used for further postprocessing.

4.3.2 Measurement Environment

The experiments were held in the SMU-in-Taos campus in Taos, New Mexico. The location is shown in Fig. 4.1. The experiment path (depicted by the white arrow) is clear from any obstacles, *i.e.,* no trees, buildings, or cars. The surrounding environment, which constituted mostly of trees, was monitored to make sure that no moving objects existed throughout the experiments. The frequency spectrum was continuously monitored to make sure there was no interfering tones.

4.4 Experiments Procedure and Calibration

We conducted three sets of experiments: User-free Ground-to-Ground, User-free UAV-to-Ground, and UAV-to-Ground with different UE use cases. In the following section, we explain the procedure of each of these experiment sets.

4.4.1 User-free Ground-to-Ground Channels

To construct a baseline understanding of pathloss and the surrounding environment, we conduct Ground-to-Ground (GtG) measurements at carrier frequencies 900 MHz and 2.5 GHz. Here, the only variable is the horizontal distance between the transmitter and receiver. Both nodes are mounted on a tripod approximately 1.5 m above ground (see Fig. 4.3(d) for one tripod location) and measurements take place at six horizontal distances of d_1 =0 m (Rx next to Tx), d_2 =20 m, d_3 =40 m, d_4 =60 m, d_5 =80 m, and d_6 =100 m.

4.4.2 User-free UAV-to-Ground Channels

With the same receiver (Rx) still on the tripod, the transmitter (Tx) is now mounted on the UAV. The Tx UAV visits the same previous Tx locations (same horizontal distances) at three different altitudes from the ground: $h_1 = 10$ m, $h_2 = 20$ m, and $h_3 = 30$ m. See Fig. 4.3(d) for a depiction of the altitudes and experiment location. If we denote one location by its horizontal distance (d) and altitude (h), then to describe, for example, the Tx UAV location at the fifth horizontal distance (80 m) and third altitude (30 m), we use the notation of (d_5, h_3).

Measurement collection starts when the UAV hovers above the user at d_1 and altitude h_1. Then, the UAV changes its horizontal distance from d_1 to d_2 and measurements are

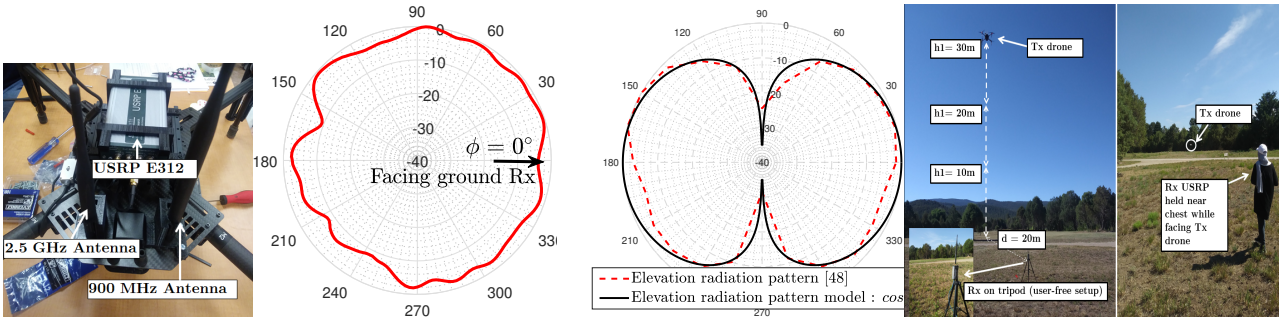

(a) (b) (c) (d)

Figure 4.3: (a) The UAV platform with the used antennas at 2.5 GHz and 900 MHz. (b) Azimuth and (c) elevation radiation pattern of the antenna at 2.5 GHz. (d) Location and setup for the UAV-to-Ground experiments. The user-free (no human body involvement) setup (left) and NCF setup (right) are shown.

collected again. The process is repeated until the UAV reaches d_6 for the same altitude, h_1. The UAV then moves to h_2 and the process is repeated until we cover the rest of hovering positions, ending with (d_6, h_3). Refer to Fig. 4.1 for the hovering positions.

4.4.3 UAV-to-Ground Channels with Different UE Use Cases

Here, we repeat the previous measurements but with a user holding the UE (Rx USRP). The wight and height of the human subject are approximately 56 kg and 164 cm. We investigate three use cases: (*i*) Near chest and facing (NCF) towards the Tx UAV, (*ii*) Near chest and facing-away (NCFA) from the Tx UAV, and (*iii*) In-pocket while facing (IPF) the Tx UAV. For each use case, we perform AtG experiments at carrier frequencies of 900 MHz and 2.5 GHz, totalling 6 experiment sets. In each of these experiment sets, we analyze how the RSS levels, shadowing, and the Rician K-factor are affected by user orientation, UE near-body location, and the drone's hovering position. An illustration of when a user is facing the Tx UAV while holding the radio device with two hands is shown in Fig. 4.3(d).

4.4.4 Power calibration with USRP E312

With software-defined radios, such as USRPs, different units can produce slightly different results when used to generate, modulate, and demodulate signals. Hence, a calibration of the transmit power at various gains is needed. The term gain here refers to the RF path gain

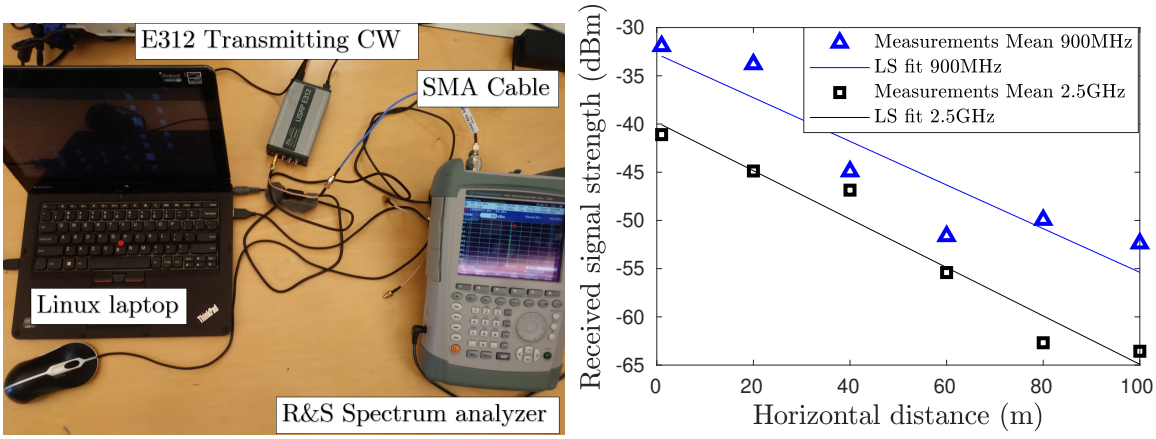

(a) (b)

Figure 4.4: (a) Power calibration setup for USRP E312. (b) User-free measurement results for the Ground-to-Ground setup at 900 MHz and 2.5 GHz.

Table 4.1: Measured Transmit Power (dBm) in USRP E312

Gain (dB)	40	45	50	55	60	65	70
f_c=2.5 GHz	-14.2	-18.8	-13.6	-8.7	-3.8	1.2	6.2
f_c=900 MHz	-24.3	-19.7	-14.4	-9.2	-4.3	-0.3	0.4

within the USRP, which comes from the power amplifier and other components within the device's circuit. The calibration setup is shown in Fig. 4.4(a). We connect our Linux-based laptop to the E312 via a serial USB cable. Then, we generate a continuous wave (CW) and measure the RMS power via a Rohde & Schwarz spectrum analyzer that was connected to the output port of the E312. The same cables E312 output port were used in our in-field experiments. We perform this calibration at 900 MHz and 2.5 GHz carrier frequencies. The results are given in Table 4.1. Cable loss was measured at 0.4 dB.

4.5 User-free Ground-to-Ground and UAV-to-Ground Channels

In this section, we briefly discuss our measurement results for the user-free GtG and AtG channels. A user-free AtG experiment is shown in Fig. 4.3(d) (left). The objective of these two experiment setups is two-fold: (i) to create a baseline understanding of the conventional ground-based channel and see how it might differ from a UAV-based link, and

(*ii*) to investigate the UAV-to-Ground channel with no user/human body involvement to directly compare to when a user is holding the UE.

4.5.1 User-free GtG Measurements Results

In this set of experiments, both the Tx and Rx are mounted on tripods about 1.5 m above the ground. Keep in mind that there is no human near or holding the receiving USRP. The received signal is averaged over 15 seconds per Rx location. The average RSS levels with their first-order, least-squares fit are plotted in Fig. 4.4(b) for both carrier frequencies.

We see that the results follow the expected behavior of terrestrial networks, where the received signal is reduced by increasing the separation distance. This reduction can be described by the log-distance pathloss model. In particular, $PL(d) = PL(d_{ref}) + 10n \log \frac{d}{d_{ref}} + \chi_{\sigma_s}$, where $PL(d)$ is the pathloss at a distance d, χ_{σ_s} is the shadowing parameter, $PL(d_{ref})$ is the pathloss at a reference distance, and n is the pathloss exponent. If we take $d_{ref} = 20$ m as our reference distance measurement, a value of $n = 2.53$ can be obtained, which is quite common for LOS experiments in this environment [46]. Moreover, the standard deviation of the shadowing parameter, σ_s, is estimated as 3.2 dB.

4.5.2 User-free UAV-to-Ground Measurement Results

Let us now examine the AtG channel with the same Rx still mounted on the tripod but with the Tx being mounted on the UAV (see Fig. 4.3(a)). As explained in Section III, the Tx UAV visits six locations per altitude while the ground Rx records the received signal.

Average RSS: The mean values of the obtained RSS levels at 900 MHz and 2.5 GHz are shown in Fig. 4.6 as dashed lines. First, we can clearly see the distinction between the AtG and GtG channels. The AtG channel results follow a curve instead of the expected straight line obtained by the GtG experiments. This curved behavior is explained here. At $d = 0$ m (*i.e.*, when the Tx UAV is directly above the Rx), low RSS levels are experienced. These results are due to two factors: the antenna elevation radiation pattern (Fig. 4.3(c)) and the UAV body. Since the Tx and Rx antennas are vertically-mounted, omni-directional antennas, the radiated power is at the minimum value in the vertical direction (*i.e.*, $\theta = \arctan(\frac{h}{d}) = 90°$). As a result, we expect to see lower RSS levels at this location compared to other distances/altitudes with angles less than 90°. Furthermore, due to the antenna being

mounted on the UAV body, the transmitted signal is partly blocked (and shadowed) by the UAV body, especially when seen from a below node. As the Tx UAV moves to the next locations, the Rx starts to experience a stronger received signal due to more alignment of the radiation pattern and less drone body obstruction. The mean RSS reaches its maximum value between 20 m and 40 m horizontal distance for all altitudes. Then, mainly due to its inverse relationship to distance, the received power starts to decrease in a way that is similar to the conventional terrestrial links. It is interesting to see that for a fixed UAV altitude, the RSS can vary by as much as 20 dB as the UAV moves from one location (above the ground Rx) to another, only 20 m away from the ground Rx. This significant change in RSS is attributed to the elevation radiation pattern of the antennas.

Shadowing: Shadowing here is exclusively caused by either the drone body or the user's body or a combination of both. As the body becomes an obstacle in the signal path, shadowing will occur and it will be a function of how much of the obstacle is obstructing the receiver path. We calculate shadowing by subtracting the received power from its average value [27] and analyze its distribution. First, we observe that the measured shadowing for all investigated cases definitely be modeled as a zero mean Gaussian random variable with its standard deviation (in dB) changing depending on the investigated scenario. Second, we find that the UAV-based channel, except for the directly above hovering position, results in less shadowing compared to the ground-based channel. We can see an example of this effect in Fig. 4.5(a) where we we plot the shadowing at 900 MHz and location (d_3, h_1). Third, compared to the user-free experiments, we find that user orientation can significantly alter the spread/standard deviation of the shadowing parameter. This can be seen in Fig.4.5(b) where shadowing is plotted for the three use cases. We can see that while the NCF and IPF are close to the user-free AtG result, the NCFA shadowing is characterized by a larger spread and standard deviation. We will elaborate on shadowing standard deviation for all use cases in the next section.

4.6 User Impact: Average Gain/Loss, Shadowing and Multipath

In this section, we investigate how different use cases of holding a UE can affect: (i) average RSS levels, (ii) shadowing, (iii) multipath characteristics, and (iv) the Rician K-

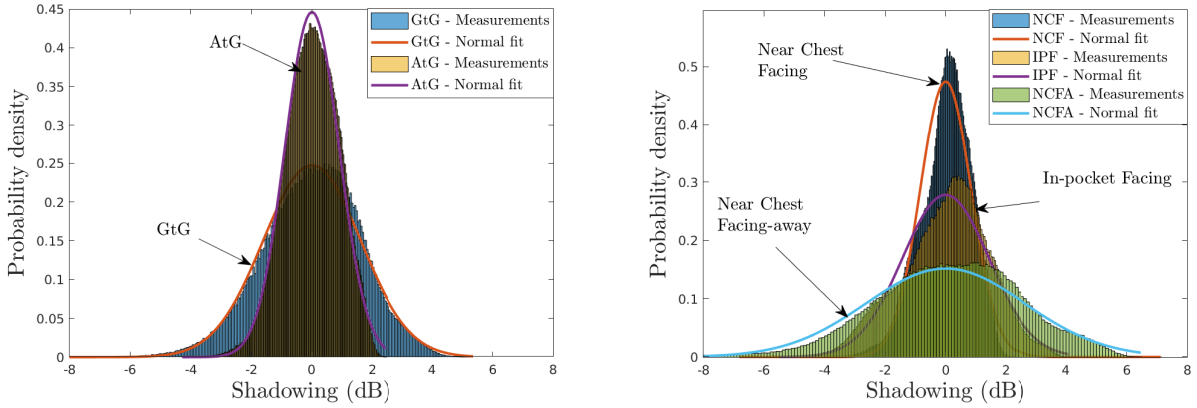

(a) (b)

Figure 4.5: Shadowing at 900 MHz for the (a) user-free GtG and AtG experiments, and (b) the three use cases in AtG channels.

factor of an AtG channel at various drone altitudes, locations, and carrier frequencies. In doing so, we consider the relative impact of user versus UAV properties on the resulting wireless channel characteristics at ultra-low drone altitudes.

4.6.1 Average RSS and User-induced Loss/Gain

Here, we define user-induced loss/gain as the difference in RSS between the baseline (User-free) scenario and the facing and facing-away scenarios when the user holds the UE close to the chest. Fig. 4.6 shows the average RSS for these three scenarios (user-free, NCF, and NCFA) at both frequencies.

User-Induced Gain Compared to Free Space. To investigate how the existence of the human body can affect the UAV-to-ground channel, we first compare the results of the Near Chest Facing (NCF) scenario to those obtained in the user-free experiment. Visually, this comparison could be made by inspecting Fig. 4.6. We find that the body of the user when facing the transmit UAV can actually result in *increased* RSS levels. For example, while the mean RSS level at (d_5, h_1) is -46.2 dBm in the user-free setup, it is -40.3 dBm when the user holds the UE facing the transmit UAV (*i.e.,* NCF), a 5.8 dB increase in the mean RSS. At the location of (d_2, h_3) a 7.6 dB increase in the mean RSS level is experienced due to the existence of the user body. Similar results are found when the UE is inside the

user's pocket. We have previously observed this effect in a GtG channel [46], where the user's body was found to result in 14% increase in throughput over a reference, user-free setup. However, it is worth noting here that the above finding depends on the UAV hovering position. For example, at 0 m horizontal distance (*i.e.*, when the UAV is directly above the user), the existence of the user's body and orientation becomes almost irrelevant to the average RSS changes as the gain/loss compared to the baseline are minimal (less than a standard deviation). Other works have also shown that the human body can increase the radiation of the antennas and additional gains of 15 dB were measured compared to free space [49]. We conclude that, compared to a user-free scenario, there exists a user-induced *gain* that yields increases in RSS levels when the UE is facing a transmitting, in-flight drone when a free-space path exists from sender to receiver. This *gain* can reach an average and a maximum value (across all locations at 2.5 GHz) of 3.4 dB and 12.05 dB, respectively. Finally, we report that with the exception of three hovering positions, average user-induced gains compared to free space at 900 MHz were insignificant, *i.e.*, less than the standard deviation of the measured signal. This might be due to the fact that the human body absorbs more power at low frequencies compared to higher frequencies at which it can reflect more power [51]. A similar effect is shown in [53] where three different human bodies were studied at 17 different frequencies. It was concluded that the radiated and attenuated power (P_{rad} and P_{loss}) across frequencies can vary according to the human body type, and that gains with respect to free-space were achieved at higher frequencies while at low frequencies, absorption resulted in no recorded gains.

User-Induced Loss Compared to Free Space. Next, we seek to understand the role of the human body on the channel when the user's orientation changes (*i.e.*, the whole body is in the path of the signal). To do so, we compare the measured RSS samples in the Near Chest Facing-away (NCFA) scenario to those obtained in the baseline (User-free) setup. We find that the user's body indeed causes reductions in the average RSS, which is is clear via visual inspection of Fig. 4.6. In particular, if we exclude the strictly-vertical UAV position at which the user's orientation is virtually irrelevant, the user's body is found to considerably reduce the average RSS. At 2.5 GHz, an average reduction of 13.2 dB and a maximum reduction of 23.1 dB across all drone hovering positions is experienced. An example of this

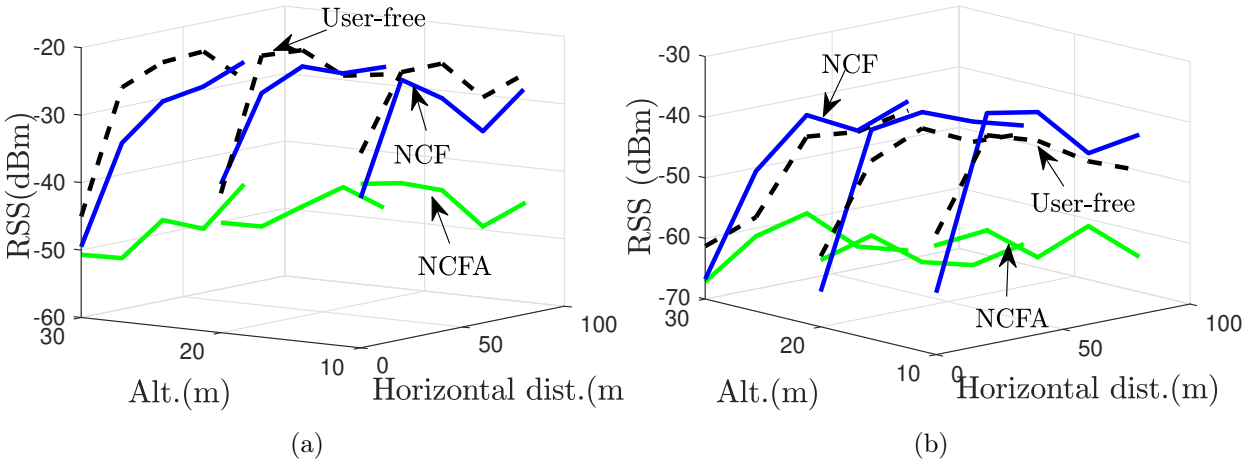

Figure 4.6: Average RSS levels for the user-free, NCF, and NCFA scenarios for all UAV hovering positions at (a) 900 MHz and (b) 2.5 GHz

loss at 2.5 GHz for location (d_2, h_2) is shown in Fig. 4.7(a) with an average value of 12.3 dB. Higher loss is measured at 900 MHz, with an average and maximum reduction of 17.5 dB and 26.3 dB, respectively. An example of this loss at 900 MHz is shown in Fig.4.7(b). This result is inline with the finding above as the human body involved in this study is found to result in more attenuation (most likely through absorption) at this frequency than 2.5 GHz. Similar values of human-induced losses compared to free-space can be found in literature [56].

Impact of User Orientation. Now that we understand how the user's body can affect the channel compared to a free-space baseline, it is interesting to compare, for the same person, how their orientation and near-body location of the UE can affect the UAV-to-ground channel. First, we compare the NCFA measurements to those obtained in the NCF (Near Chest Facing) scenario. This corresponds to comparing the top and bottom solid lines/curves in Fig. 4.6. We see that,for both frequencies, the human body results in signal blockage significantly reducing the average RSS. These losses can reach about 25 dB at 2.5 GHz, and 21 dB at 900 MHz (Fig. 4.8). Interestingly, this observation does not apply to the strictly-vertical location, as the user's orientation is arbitrary relative to the UAV and the difference between the two cases is minimal. The effect of this UAV hovering

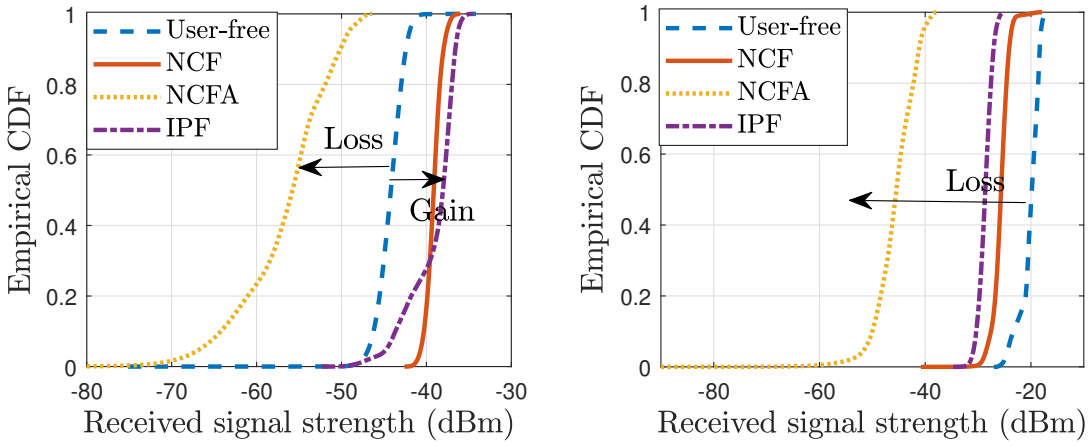

Figure 4.7: Comparing the RSS in three use cases to the free-space scenario at (a) 2.5 GHz and (b) 900 MHz for UAV hovering position (d_2, h_2). User-induced gains are recorded at 2.5 GHz where at 900 MHz, only losses are experienced.

position can be clearly seen in Fig. 4.8 where the first horizontal distance has both, negative and positive average values of the investigated impact. As we move to the next hovering positions, however, the human body blockage starts to be quite consistent ranging between 15 dB and 21 dB across all locations. Similar reductions due to user blockage can be found in [49, 56, 57].

Impact of Near-Body Location for a Fixed User Orientation. For the same drone hovering location and the same user orientation of facing the transmit UAV, we investigate if placing the UE near different body locations yield different received signal strengths. To do so, we calculate the difference in average RSS level in NCF and IPF scenarios and analyze the results. This difference at 900 MHz is plotted (as grey bars) in Fig. 4.8. First, we see that placing the UE inside the pocket causes reductions in average RSS levels, which is evident by the positive loss values across many hovering positions. This degradation can reach around 8.5 dB. Interestingly, we find that this difference is not constant and can change by altering drone's hovering altitude. Specifically, the difference increases as the UAV's hovering altitude increases. This trend can be seen in Fig. 4.8. For example, at 40 m distance and 10 m altitude, the average difference between the two use cases is around -2.5 dB. At a 30 m

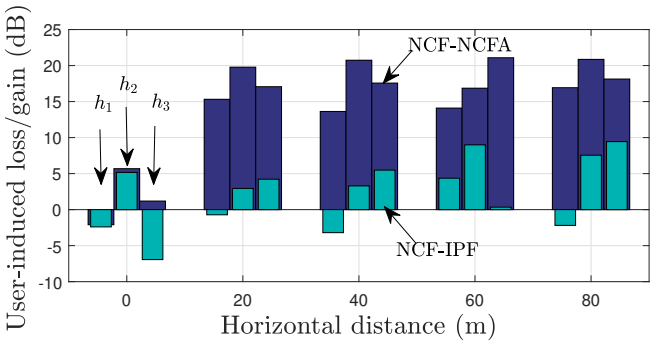

Figure 4.8: Average user-induced loss/gain for all investigated distanced and altitudes at 900 MHz.

altitude of the same horizontal distance, this difference is about +5 dB (a 7.5 dB increase in difference).This improvement (negative dB values at low altitudes) could be attributed to the fact that, as the drone hovers at lower altitudes, it starts to exhibit a stronger LOS with the UE inside the pocket, and as a result, the difference between the two use cases decreases. This finding is consistent across all but the first hovering position. We also find that this behavior (stronger RSS in IPF compared to NCF at h_1) occurs mostly at 900 MHz but not at 2.5 GHz and it diminishes as we go to higher altitudes. Fig. 4.9 shows the difference in RSS due to placing the UE inside the pocket at two frequencies, averaged over all distances for h_1 and h_3. From Fig. 4.9(a) we can see that at h_1 and 900 MHz frequency about 60% of NCF-IPF values are negative indicating stronger IPF while zero values are recorded at the same altitude for 2.5 GHz. As we move to higher altitudes the distinction between two frequencies become negligible with an almost identical CDF at h_3 (see Fig. 4.9(b)). This effect might be attributed to the longer wavelength at 900 MHz and better penetration characteristics over 2.5 GHz. However, more investigation is needed.

Recalling that the user's orientation is fixed (facing the UAV), *we conclude that there exists not only an optimal UAV position for a UAV-to-user connectivity based on their orientation, but there also exists an optimal UE location on/near their body when facing the UAV in a LOS setup.* This result could influence algorithms that adapt to different user gestures based on wireless sensor measurements.

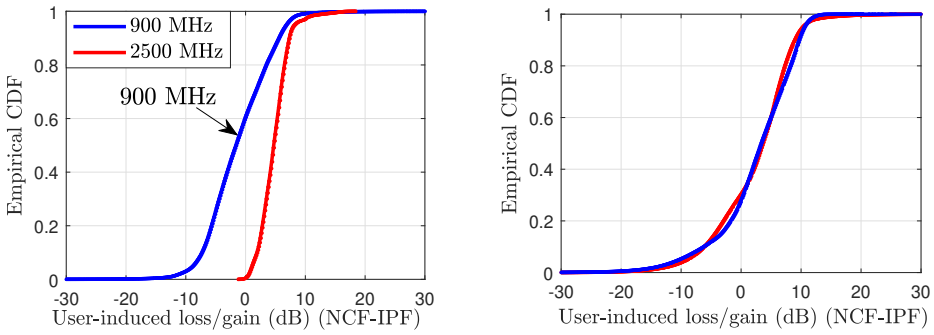

(a) (b)

Figure 4.9: User-induced loss/gain due to placing the UE inside pocket at two frequencies at drone altitudes (a) $h_1 = 10$ m and (b) $h_3 = 30$ m.

4.6.2 Shadowing and Multipath Due to UAV and User Bodies

In this section, we discuss how shadowing and multipath are affected by the UAV, its mounted antenna radiation pattern, and the human body. Specifically, we investigate how these factors can impact the shadowing standard deviation and the multipath parameter (σ in (2.9)). Fig. 4.10(a) shows the instantaneous RSS when the UAV is directly above the user (*i.e.*, at (d_1,h_1)), while Fig. 4.10(b) illustrates the RSS when the UAV is at d_2 at the same altitude (*i.e.*, at (d_2,h_1)). Fig. 4.10(c) shows the estimated multipath parameter, from measurements and the fitted Rician model, at one altitude of 20 m across all distances. There are two important observations to be made here.

Impact of the elevation radiation pattern and UAV body on shadowing standard deviation. Even though the separation distance increases from when the drone is hovering above the user (d_1, h_1) to when the UAV is at (d_2, h_1), (*i.e.*, from $d_x = \sqrt{d_1^2 + h_1^2} = \sqrt{0^2 + 10^2} = 10$ m to $d_x = \sqrt{d_2^2 + h_1^2} = \sqrt{20^2 + 10^2} = 22.36$ m), which would lead us to expect a reduction in the received power by an approximate 7 dB as a result of the inverse relationship between received power and distance, it actually increases by 28 dB in the facing scenario.

The reason behind this behavior is the increased power in the radiation pattern of the antennas along the elevation plane and the reduced UAV body shadowing. The elevation radiation pattern of the omni-directional dipole antenna, which is depicted in Fig. 4.3(c)

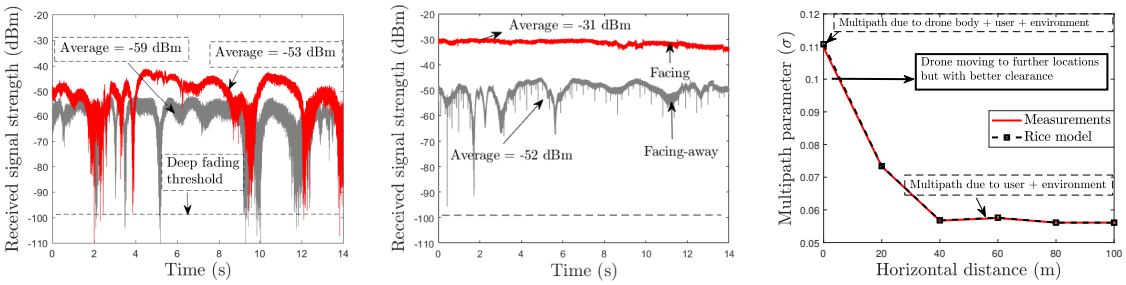

(a) UAV is directly above ground user

(b) UAV is 20 m away

(c) Rician multipath parameter at 20 m altitude.

Figure 4.10: Effect of UAV body on shadowing and multipath effects. (a) Drone is hovering directly above the user at $d_1 = 0$ m, $h_1 = 10$ m; significant multipath resulting in multiple deep fading events. (b) Drone is 20 m away resulting in less multipath effects and a more stable signal level with no deep fading events. Also, a significant increase in signal level is experienced due to better radiation pattern product and less shadowing caused by the drone body. (c) The Rician multipath parameter σ obtained from measurements and Rician fit versus drone hovering locations; it is noticeable that as the UAV moves away from the strictly above location less multipath is exhibited by the ground user.

clearly shows that at strictly-vertical links ($\theta = +/-90$) the antenna experiences significant reductions in its radiated power. This is inline with the theory that indicates zero radiated power in the vertical plane (*i.e.*, $G_{Tx}(\theta) = \cos(\theta) = \cos(90) = 0$) [8]. In addition to this, the UAV body acts as an obstruction causing shadowing (reduction in the strength of the otherwise LOS component) and an increase in multipath effects. As the UAV moves from d_1 to d_2, there becomes more clearance in the Tx-Rx path and less obstruction/shadowing caused by the drone body, and the radiation pattern product $G_{Tx}G_{Rx}$ becomes stronger. For example, the radiation pattern product at 20 m horizontal distance and 10 m altitude is $G_{Tx}G_{Rx} = \cos^2(\theta) = \cos^2(\arctan(\frac{10}{20})) = 0.8$. This value corresponds to -0.97 dB which, compared to approximately -35 dB (assuming a $\theta = 89°$), is a significant increase in received power value. This reasoning is valid for the facing scenario, regardless of the UE near-body location. When the user is facing-away, as the UAV moves to d_2, the increase in the RSS level, which was previously obtained due to the radiation pattern impact, is now negated by the impact of the user's body. That is, even though the UAV moves to a location where the elevation radiation pattern is much stronger and with a less obstructed path by the UAV

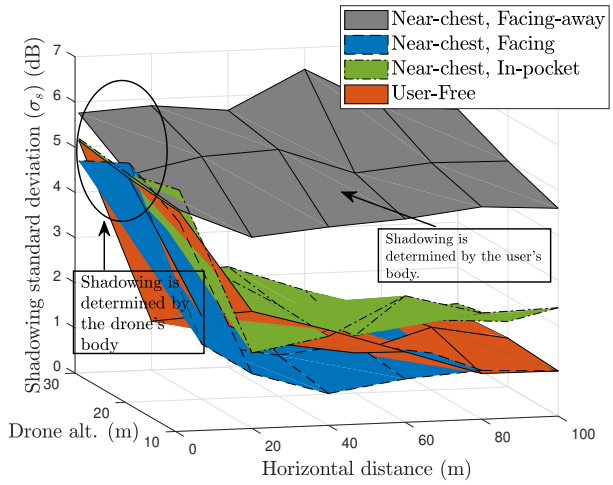

Figure 4.11: Shadowing standard deviation for the three use cases at a carrier frequency of 2.5 GHz.

body, the user's body now becomes the main obstruction, and the received signal ultimately remains approximately the same as when the drone hovers above the user (see Fig. 4.10(b)).

We have investigated the shadowing standard deviation for all experiments and found that it is greatest when the UAV is directly above the user (at d_1) with values of $\sigma_s > 4$ dB across all experiments and frequencies. Then, it gradually decreases as the UAV moves to more-distant locations that have a less obstructed Tx-Rx path. This behavior occurs in both scenarios of facing and in-pocket, and it can be clearly seen in Fig. 4.11, where we plot σ_s (shadowing standard deviation) for all UAV locations at 2.5 GHz. In this figure, we can see that shadowing is approximately the same for the three use cases when the UAV is above the user at location d_1 for all altitudes. At this UAV hovering position, shadowing is dominated by the UAV's body, not the user or their orientation. Moving away from this location, shadowing starts to decrease for the facing and in-pocket scenarios while, in the facing-away scenario, it stays approximately the same regardless of the UAV location, suggesting that shadowing becomes dominated by the user's body, not the UAV.

The shadowing standard deviation at 900 MHz is summarized in Table 4.2. Similar to the 2.5 GHz results, we notice that, while there is little difference between the facing and in-pocket scenario, differences between these two and the facing-away scenario can reach up

Table 4.2: Shadowing Standard Deviation at 900 MHz

Pos.	NCF						IPF						NCFA					
d / h	d_1	d_2	d_3	d_4	d_5	d_6	d_1	d_2	d_3	d_4	d_5	d_6	d_1	d_2	d_3	d_4	d_5	d_6
h_1	4.7	2.4	2.1	1.5	1.9	1.0	4.0	2.4	3.3	1.9	3.6	2.4	4.9	3.2	3.1	3.7	3.7	4.6
h_2	4.1	2.6	2.4	2.3	0.8	0.8	4.0	1.9	1.1	1.3	1.2	1.4	5.1	3.7	4.5	3.5	5.7	5.0
h_3	4.9	2.6	2.0	1.4	0.8	0.9	3.1	2.1	2.2	1.4	1.2	1.1	4.6	5.3	5.1	3.6	3.6	5.5

to 5.7 dB. Also, shadowing, regardless of the use case, is highest at the location of (d_1, any h) due to the above explained effect of the UAV body. *We then conclude that in LOS UAV-to-User channels there exists two regions for shadowing: one that is dependent on the UAV body and another that is mainly affected by the user's body.* This conclusion excludes any external/environmental causes. That is, the observed effects are due to either the UAV or the user, not any environmental changes. As stated in the experiment setup, the experiments were done clear of any obstacles and free of any surrounding moving objects.

Impact of the UAV body on multipath. When the UAV is flying directly above the user, the multipath experienced at the receiver is stronger than in any other UAV hovering location. This result holds true across all frequencies and use cases. We can clearly see this effect by comparing the two figures in Fig. 4.10. Let us define a deep fading event to be that at which the SNR falls to approximately 0 dB. At this value, the packet delivery ratio of many off-the-shelf IEEE 802.11 products could fall between 0% to 5% indicating the potential of a complete loss of data packets. Our measured noise floor was in the range of -100 dBm to -105 dBm. If we observe Fig. 4.10(b), which corresponds to location (d_2, h_1), we see that the received signal is characterized by no deep fading events and the strong fading events that occur still give us an SNR of at least 10 dB. However, when the UAV is hovering directly above the user (Fig. 4.10(a)), this is not the case: multiple deep fading events occur, where the received signal falls to extremely low levels, indicating strong destructive interference effects. More specifically, during a time duration of 15 seconds, more than 10 deep fading events can occur as a result of the UAV body being strictly above the user. To understand how multipath is induced by the UAV body and how it can dramatically change

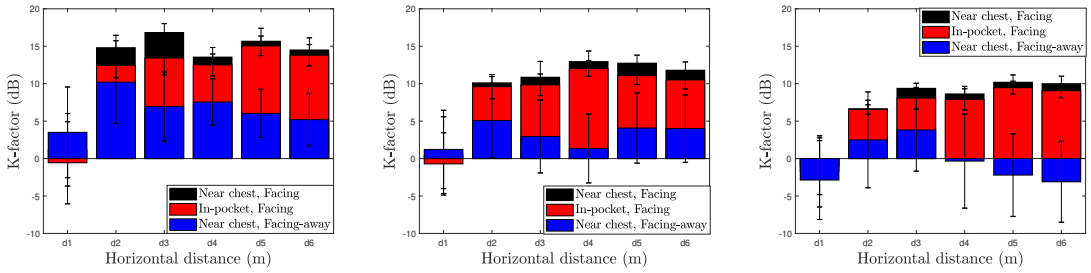

(a) (b) (c)

Figure 4.12: The average and standard deviation of the measured Rician K-factor for the three use cases of the LOS UAV-to-Ground channel at 2.5 GHz and a UAV altitude of (a) 10 m, (b) 20 m, and (c) 30 m.

depending on the drone's relative UAV location, and consequently the Tx-Rx path clearance, let us examine Fig. 4.10(c). In this figure, we plot the estimated multipath parameter (σ in equation (2.9)) across all distances for a fixed UAV altitude. Both the value obtained from measurements and that from fitting a Rician distribution are plotted. When the UAV is directly above the user, we obtain $\sigma = 0.11$. As the UAV transitions to the next location, it falls to 0.075 and then settles at around 0.055, which is a 50% decrease in multipath from when the UAV is strictly above the user. It is interesting to note that a similar curve was obtained by [26] with a model that describes how multipath decreased with increasing drone height was obtained. However, here, the altitude is fixed, and the only variable is horizontal distance, which corresponds to the Tx-Rx path clearance.

4.7 The Rician K-factor in UAV-to-Ground Channels for Different Use Cases

In this section, we present how the Rician K-factor, which is a measure of channel fading severity, can be influenced by the user's orientation, UE near-body location, and the UAV's hovering location. Before elaborating on these scenarios, the time-varying nature of the K-factor as a result of the UAV's continuous hovering is addressed.

4.7.1 Impact of UAV Hovering and User Body on The K-factor's Time Variability

The UAV's continuous movement while hovering could result in variations in the K-factor. That is, the main LOS component and/or the multipath components from one window to another, might vary. To visualize the issue, Fig. 4.13 shows the calculated K-factor for 200

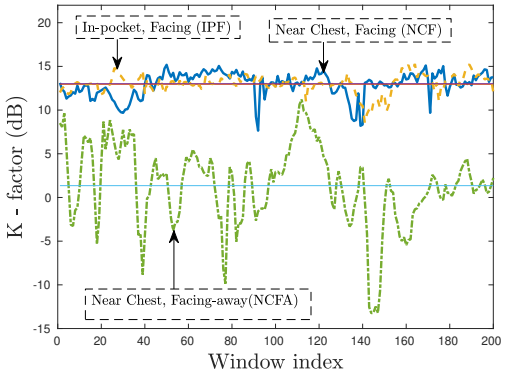

Figure 4.13: The time-varying nature of the K-factor as a function of the use case.

windows (approx. 13 seconds of hovering duration) at location (d_4, h_2). We first consider the case where the user is facing the drone (NCF or IPF). We see that the K-factor varies along a range of 10 dB to 14 dB. The average value for both cases, however, is the same. This variation in the K-factor is due to the time-varying nature of the channel, which is a result of the UAV's hovering motion. Recall that the user is fixed, and there is no moving objects in the experiment area. When the user's body is added to the equation (*i.e.*, the user is facing-away), severe fluctuations are experienced in the K-factor, and the mean value becomes unstable. This is clear in the NCFA plot in the same figure where the value of K can vary from -12 dB to 10 dB (22 dB range). After investigating the K-factor variance as a function of the user's body, we found that a worst case scenario of 20-times stronger variance is observed as a result of fluctuations induced by the user's body. These strong fluctuations could be attributed to the random nature of multipath reflections caused by propagation through the human body [60]. The time-varying nature of the K-factor has been addressed in [13], but the experiments were conducted with a high-altitude platform in an urban area; in other words, variations in the K-factor where not specifically due to a UAV's hovering state nor the user's body, but variations in the urban environment. Similarly, the work in [27] characterized the K-factor for low-altitude UAVs, but the experiments were done in an urban environment crowded with buildings and spanned large horizontal distances. The work in [60] leveraged the time-varying nature of multipath reflections within the body to

achieve incoherent beamforming using signals of different frequencies.

4.7.2 Rician K-factor When Facing Tx UAV

In this section, we analyze the Rician K-factor when the user is facing the Tx UAV. The average value and standard deviation of the Rician K-factor at 2.5 GHz for all use cases across all locations is plotted in Fig. 4.12.

First, we see that, for a fixed altitude, the Rician K-factor experiences a significant change as the UAV moves from d_1 to any other hovering location. For example, in Fig. 4.12(a), when in-pocket and at a UAV altitude of 10 m, the average K-factor can change from approximately $\overline{K} = 0$ dB when the Tx UAV is directly above the ground Rx (*i.e.*, $d_1 = 0$ m) to $\overline{K} = 12$ dB as the UAV hovers at $d_2 = 20$ m. Such a dramatic change in the K-factor is attributed to the impact of both the elevation radiation pattern of the vertically-oriented antenna and the body of the UAV. Recall that a vertically-oriented omni-directional dipole antenna theoretically does not radiate in the vertical direction. In reality, however, there will still be some radiated power at significantly-less levels. This radiation-pattern effect will impact the main LOS component of the received signal, while the body of the UAV and its induced reflections will cause a larger value of the multipath component (σ in (2.9)). The end result of this effect is the significant reduction in the K-factor, which we observed at d_1 at all altitudes and both carrier frequencies. The same observation can be made for the near-chest scenario with slightly higher K values at the same distances.

The K-factor also, for the same horizontal distance, decreases when increasing the drone altitude. For example, if we examine the results of the K-factor at d_3 for the near-chest scenario, we see that it decreases from around $K = 17$ dB at $h_1 = 10$ m to $K = 11$ dB at $h_2 = 20$ m to approximately $K = 9.5$ dB at $h_3 = 30$ m. This reduction in value is mainly due to increases in distance and the radiation pattern misalignment loss, both of which will cause reductions in the strength of the main LOS component. This behavior (reduction in K-factor with increased altitude) has been previously analyzed by our research team in UAV-to-UAV channels.

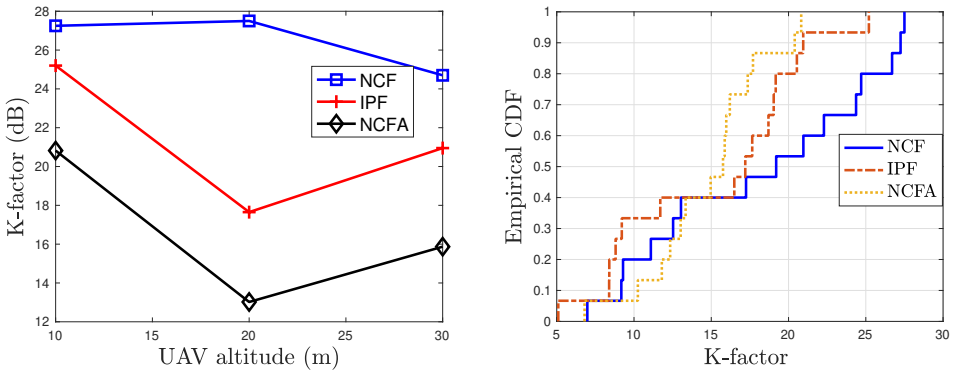

(a) (b)

Figure 4.14: (a) Average K-factor for the three use cases at one horizontal distance and different UAV altitudes at 900 MHz. (b) The empirical CDF of the average K-factor across all locations and use cases at 900 MHz.

Table 4.3: Average K-factor at 10 m drone altitude for 900 MHz and 2.5 GHz in the three use cases.

Frequency	NCF	IPF	NCFA
900 MHz	20.65	13.41	17.92
2.5 GHz	12.6	11.2	6.63

4.7.3 Rician K-factor When Facing-Away from Tx UAV

In the previous section, we saw how the Rician K-factor can vary with UAV altitude and its location relative to a ground user that is facing the drone. If the user is facing-away from the transmitting UAV, the question becomes about how severe is the user's impact on the channel and the Rician K-factor and whether or not it turns into a Rayleigh channel ($K = -\infty$ dB).

We find that in all but one location, where the Tx UAV hovers directly above the ground user, the K-factor experiences great reductions as the user faces-away from the flying UAV. This is clear in the results plotted in Fig. 4.12. At h_1, for example, the difference in K-factor between the facing and facing-away for the same body position (near chest) can reach up to 11 dB and an average value across all locations of 6.18 dB. As the UAV moves to

Table 4.4: Parameters of the LOS UAV-to-user channel in NCF setup

	Measured		Rician Fit		Error	
dist.	a	σ	a	σ	$RMSE_a$	$RMSE_\sigma$
d_1	0.643	0.1097	0.633	0.1107	0.01	9.41E-04
d_2	0.7877	0.0733	0.7843	0.0734	0.0035	1.61E-04
d_3	0.8462	0.0567	0.8443	0.0568	0.0019	6.38E-05
d_4	0.8552	0.0575	0.8533	0.0561	0.0019	6.07E-05
d_5	0.8029	0.0561	0.8008	0.0576	0.0021	4.57E-05
d_6	0.798	0.063	0.7958	0.0631	0.0025	9.77E-05

higher altitudes and the general trend of the K-factor tends to result in weaker values for all scenarios, the user's body blockage starts to result in negative values (in dB) at h_3, suggesting an extremely weak LOS component and an increase in multipath effects.

4.7.4 Frequency Impact on K-factor:

To investigate how carrier frequency can affect channel fading severity measured by the K-factor, we compared the average values of the K-factor at both frequencies across all three use cases. We found that across most measurements, the K-factor at 900 Mhz was higher than the 2.5 GHz results. Comparison results at h_1 are given in Table 4.3. The stronger K-factor at 900 MHz is evident across all three use cases reaching an average and maximum difference of 7.18 dB and 11.3 dB respectively. However, slightly larger variance in the K-factor is observed at 900 MHz. Due to stronger K-factor values at 900 MHz, the values obtained when facing-away are positive dB values, indicating a stronger ratio of LOS to scattered/multipath power than that at 2.5 GHz. An example of the 900 MHz K-factor is given in Fig. 4.14. To the left (Fig. 4.14(a) the average value at (d_5, h_2) for the three cases is shown. If we compare those to the values obtained at the same location but at 2.5 GHz (Fig. 4.12(b)), we can see that the NCFA K-factor at 900 MHz is about 8 dB stronger. As a result, the NCFA K-factor at 900 MHz is approximately the same as the NCF K-factor at 2.5 GHz. To further investigate this frequency dependence, we compare all average values of the K-factor at 900 MHz (Fig. 4.14(b)) to those obtained at 2.5 GHz (Fig. 4.12). We can first notice that while there exists no negative (in dB) values of the K-factor at

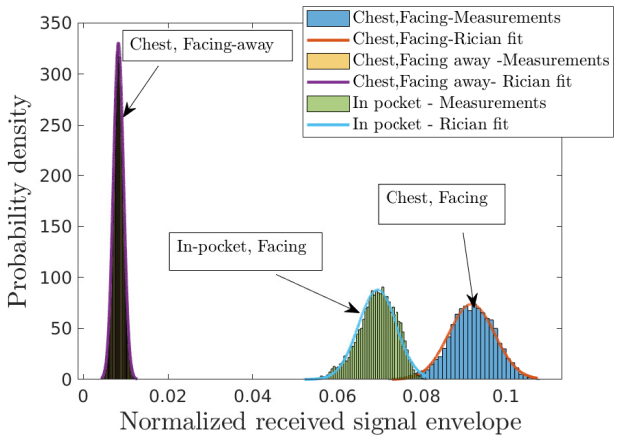

Figure 4.15: Histogram of the measured values of the normalized received signal envelope and its fitted Rician distribution at a drone altitude of 20 m.

900 MHz, at 2.5 GHz and a UAV altitude of 30 m, many instances result in negative K-factor values. Moreover, we can see that about 50% of the values at 900 MHz exceeds 17 dB for NCF and IPF while no values reach that level at 2.5 GHz. The above discussion reveals that using lower frequencies might result in a more deterministic behavior of UAV-based fading channels. This finding might be attributed to the fact that lower frequencies has a longer wavelength and therefore less sensitivity to UAV hovering jitter/fluctuations error. Designers of UAV-based air-to-ground channels should expect about 7 dB degradation in K-factor values as they move from 900 MHz to somewhere near 2.5 GHz, and plans, in terms of adaptive power control and required SNR – to meet certain bit error rates – should change accordingly.

4.7.5 Is Rician Distribution a Good Fit for All Three Cases?

While it might be expected that the channel follows a Rician distribution in NCF and IPF scenarios, it is interesting to see if this assumption still holds when facing-away from the UAV. Therefore, to test the assumption of the Rician channel for all three scenarios at both frequencies, we fit a Rician distribution using the Maximum Likelihood Estimate (MLE) to the measured values of the normalized received signal envelope for various time durations and compare the obtained fit to the measurements. The comparison shows that the Rice model can adequately represent the channel for all three scenarios with an average RMSE error of

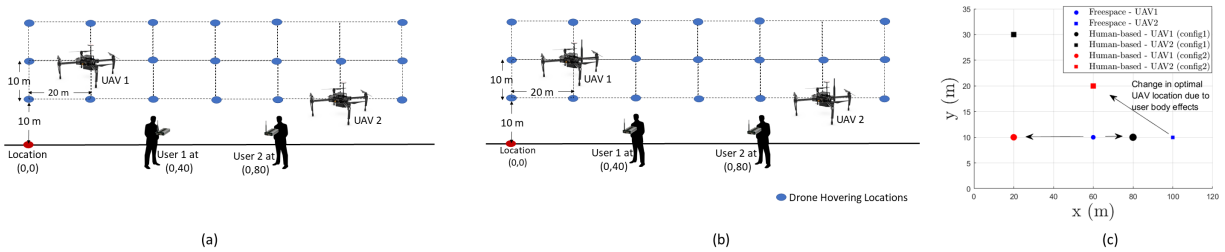

Figure 4.16: Illustration of human-based physical layer security for UAV-assisted networks. (a) User 1 faces east and User 2 faces west, (b) Both Users face west. (c) Impact of including the human-induced effects on optimal location of UAVs for maximum secrecy, where marker size is proportional to secrecy rate.

4.99E-03 and 4.16E-04 in a and σ (of equation (2.9)), respectively. This result indicates that even though the main LOS component was shadowed by the human body in the NCFA case, there still exists some dominant component compared to the multipath/scattered component captured within that time period. A summary of the obtained parameter values through measurements and the Rician fit for a UAV altitude of $h_2 = 20$ m in the NCF scenario are given in Table 4.4. We see that the Rician model is a good fit for all UAV positions, even d_1 (drone directly above user). An example of the measured normalized received signal envelope and its Rician fit when the UAV is 80 away at h_2 is shown in Fig. 4.15. We see a close proximity between the histogram of measured data and the Rician fit. In addition, the impact of the user's body on the measurements is clear; the measurements are distributed, from lowest to highest, in the following order: near chest facing-away (NCFA), in-pocket facing (IPF), and near-chest facing (NCF). We note that even though the signal path is obstructed by the user's body, the received signal envelope still follows a Rician distribution in the facing-away scenario, indicating that there still exists a dominant signal component, however, at significantly lower level compared to the other two scenarios.

4.8 Applications: Human-based Deployment of UAVs for Optimal Secrecy

The obtained insight from this work can find various applications. The focus here is on physical layer security and secrecy maximization based on the orientation of ground users relative to ultra-low UAVs.

Physical layer security has been recently proposed for UAV-based communication sys-

tems [61–63]. However, none of these works consider the human-body effect, its orientation, and the UAV-body impact on wireless channels to understand real-world physical layer security performance. Here, based on the collected experimental measurements of UAV-to-user channel for different UAV positions and human body orientations, we show that the average secrecy performance of UAV-based wireless communication systems for different low-altitude UAV positions and human body orientation is significantly different compared to the theoretical analysis on physical layer secrecy performance that do not consider user and drone body effects [61–63].

Consider a UAV-assisted wireless communication system with two UAVs and two users as shown in Fig. 4.16. The location $(0, 0)$ is shown with a 'red dot' in Figs. 4.16 (a) and (b), and users 1 and 2 are located at $(0, 40)$ m and $(0, 80)$ m, *i.e.*, 40 m apart from each other. Each UAV can move to one of the locations $(i \times 10, j \times 20)$ m where $i \in \{1, 2, 3\}, j \in \{0, .., 6\}$, as marked with 'blue dot's in Figs. 4.16(a) and (b). The UAVs 1 and 2 aim to send confidential messages to users 1 and 2, respectively, and interference can be avoided by using two separate carrier frequencies, 2.5 GHz and 900 MHz for signals intended for users 1 and 2, respectively. Each user i tries to overhear the signal intended for the other user j which is transmitted from UAV j $(i, j \in \{1, 2\}, j \neq i)$. We investigate the secrecy performance for such a network with two different user orientation configurations; (1) User 1 is facing east while user 2 is facing west, as shown in Fig. 4.16(a), and (2) Both users are facing west, as shown in Fig. 4.16(b). We measure secrecy performance for each user for a given configuration in terms of ergodic secrecy rate. For a given location l of UAV i, the instantaneous secrecy rate for user i at time slot n can be defined according to [64]:

$$r^l(n) = \left[\log_2\left(1 + \gamma_i^l(n)\right) - \log_2\left(1 + \gamma_j^l(n)\right)\right]^+ \tag{4.1}$$

Here, $\gamma_i^l(n)$ and $\gamma_j^l(n)$ are the SNR for UAV i to user i and UAV i to user j at time n $(i, j \in \{1, 2\}, j \neq i)$, respectively, and $[x]^+ = \max(x, 0)$. Then, the ergodic secrecy rate can be obtained as follows:

$$\mathcal{R}^l = \frac{1}{N} \sum_{n=1}^{N} r^l(n) \tag{4.2}$$

Here, N is the total duration of measurements in terms of number of time slots. The ergodic secrecy rate for UAV 1's signal for different UAV 1's locations in case of configurations 1 and 2 are shown in Tables 4.5 and 4.7, respectively and the ergodic secrecy rate for UAV 2's signal for different UAV 2's locations in case of configurations 1 and 2 are shown in Tables 4.6 and 4.8, respectively [2]. It can be observed that the ergodic secrecy rate for a given user i is impacted by UAV i to users i and j distances as well as the factors that determine the shadowing effect on these channels, *e.g.*, carrier frequency and the orientation of each user. As shown in Tables 4.5-4.8, the ergodic secrecy rate of user i is low when UAV i is behind or above the user i while user j is facing UAV i, and the ergodic secrecy rate of user i is high when user i is facing UAV i while the UAV is behind the user j. The reason is that the shadowing effect on a UAV-to-user channel is less when the user is facing the UAV as compared the scenario in which the UAV is behind or above it. If the UAV-to-user channel is assumed to follow a free-space path-loss model[3] *i.e.*, with channel gain between UAV i to user j modeled as $g_{i,j} = \frac{\beta}{d_{i,j}^2}$ (assuming the probability of a LoS channel as 1 for rural area [61]), where β is the channel power gain at the reference distance 1 m, and $d_{i,j}$ is the link distance, the sum ergodic secrecy rate for configuration 1 or 2 is maximum if UAVs 1 and 2 are positioned at $(10, 60)$ and $(10, 100)$, respectively. However, positioning the UAVs 1 and 2 at $(10, 60)$ and $(10, 100)$, respectively, would result in a poor ergodic secrecy rate for users 1 and 2, as shown in Tables 4.5-4.8. It can be observed from Tables 4.5 and 4.6 that the optimal locations of UAVs 1 and 2 for configuration 1 that maximizes the sum ergodic secrecy rate are $(10, 80)$ m and $(30, 20)$ m, respectively, for which the sum ergodic rate is 16.38 bps/Hz. It can be observed from Tables 4.7 and 4.8 that the optimal locations of UAVs 1 and 2 for configuration 2 are $(10, 20)$ m and $(20, 60)$ m, respectively, for which sum ergodic rate is 9.9 bps/Hz. The change in the optimal location of both UAVs due to the discussed human-induced effects are shown in Fig. 4.16(c). We then conclude that positioning UAVs using the knowledge of human body orientation and human body

[2]We assume that RSS measurements for each UAV-to-user channel can be obtained at the UAV since both users are part of the communication system. Therefore, the UAVs can determine users' orientations and locations using machine learning methods, such as [58] or using an optical camera if available. Using this information and (4.2), the ergodic rate lookup tables, such as Tables 4.5-4.8, can be generated.

[3]Free-space path-loss models have been commonly adopted by the UAV research community to model the UAV-to-user channel [61–63].

Table 4.5: Secrecy Performance of UAV 1's signal at different locations of the UAV 1 when UE 1 Faces East and UE 2 Faces West

Alt. \ Dist.	0 m	20 m	40 m	60 m	80 m	100 m	120
10 m	0	0	0	0	8.75	3.12	5.61
20 m	0	0	0	0	8.72	5.13	6.37
30 m	0	0	0	0	7.88	4.70	5.04

Table 4.6: Secrecy Performance of UAV 2's signal at different locations of the UAV 2 when UE 1 Faces East and UE 2 Faces West

Alt. \ Dist.	0 m	20 m	40 m	60 m	80 m	100 m	120
10 m	4.14	1.72	4.10	0	0	0	0
20 m	6.04	6.76	4.98	0	0	0	0
30 m	6.97	7.63	6.33	0	0	0	0

effects on wireless channels when UAVs are flying at low altitudes results in a significantly higher ergodic secrecy rate compared to the UAVs' location optimization strategies that are employed without considering the human-induced effects.

Table 4.7: Secrecy Performance of UAV 1's signal at different locations of the UAV 1 when Both UEs Face West

Alt. \ Dist.	0 m	20 m	40 m	60 m	80 m	100 m	120
10 m	2.34	3.30	0	0	1.25	0.29	0.41
20 m	1.85	0.68	0	0	1.14	0.17	0.92
30 m	0.41	0.17	0	0	2.73	0.63	0.16

Table 4.8: Secrecy Performance of UAV 2's signal at different locations of the UAV 2 when Both UEs Face West

Alt. \ Dist.	0 m	20 m	40 m	60 m	80 m	100 m	120
10 m	0.16	0	4.10	5.08	0.91	2.98	1.54
20 m	0.09	0.46	4.98	6.60	2.12	0.20	1.23
30 m	1.13	1.96	6.33	5.67	0.68	0.46	0.33

Chapter 5

Leveraging UAV Rotation to Increase Phase Coherency in Distributed Beamforming Systems

Research has been recently exploring distributed beamforming from a UAV swarm to achieve extended range and limited interference [65]. In the previous chapters of this work we showed that the UAV body can increase polarization mixing and result in significant reductions in cross-polarization discrimination (XPD). This finding meant that the UAV alters the phase of the incident electromagnetic wave. In this chapter, we study the impact of this effect on phase coherency in distributed transmit beamforming systems under the context of UAV swarms.

The use of UAV-based distributed transmit beamforming (DTBF) is motivated via the search and rescue example illustrated in Fig. 5.1. In this scenario, a drone swarm covers a large search area to look for missing persons/soldiers. The swarm hovers over the large area while an anchor UAV, near the base camp, acts a relay. We are interested in the swarm-to-anchor link. Due to the long distance separating the swarm and the anchor drone, the UAV swarm is tasked to beamform the common message signal (*e.g.,* target found) to the anchor drone which in turn will relay back the information to the base. As is the case with any wireless system, there are many challenges to overcome (*e.g.*, carrier frequency offset, timing errors, channel reciprocity). However, there are two challenges that are unique to achieving transmit beamforming from a UAV swarm:

1. Phase errors due to local oscillator (LO)/phased locked loop (PLL): each UAV will have its own independent radio equipment with its own local oscillator (LO), resulting in a phase offset from a certain reference (*e.g.*, zero degrees).

2. Phase offsets due to drone hovering position error: changes in the phase of the incoming or departing wave due to position deviation could be significant, depending on the

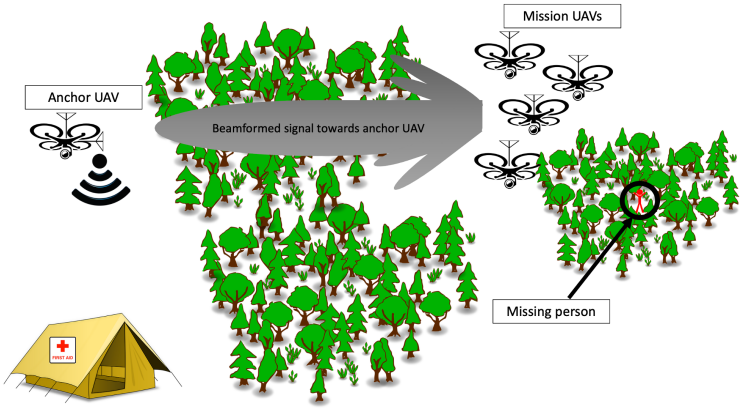

Figure 5.1: A scenario where DTBF could help search and rescue missions.

wavelength and the amount of displacement.

It is well documented that phase coherency among the transmitters is critical to the success of beamforming [66]. Even if the system were to implement perfect channel state information (CSI) feedback for conjugate beamforming (which would require significant overhead), the phase incoherent LOs and UAV hovering would result in a reduction of the beamforming gain. An additional factor, which we will use to our advantage in this work, is that the particular placement of the antenna on the body of a drone can significantly alter the antenna's radiation pattern and cause local scattering, which further disrupts the phase of the signals.

In this chapter, we characterize the two sources of phase incoherency listed above, analyze their potential impact on a distributed beamforming system, and then demonstrate experimentally how local rotations at the receiver can counteract some of the impact of phase incoherency at the transmitter.

5.1 Related Work

Many works have addressed the issue of distributed transmit beamforming in the past two decades. Stemming from the idea of cooperation between distributed sensors, the work in [67] addressed how the beam pattern of a distributed set of sensors could affect beamforming gains, while [68] addressed issues related to synchronization and phase errors. In [69],

a distributed transmit beamforming (DTBF) approach that utilizes 3 bits for feedback is proposed. One-bit feedback schemes, such as [70], have also been proposed to achieve beamforming gains in DTBF scenarios. In [71], a fully-wireless implementation of DTBF with one-bit feedback was demonstrated. Other methods that also rely on some sort of feedback, such as SNR [72], have been proposed. In [73], a time slot was continuously allocated for phase synchronization followed by a beamforming time slot; the process resulted in low spectral efficiency but good overall beamforming gains.

Works that investigate UAV-based beamforming have been emerging recently. For example, in their AirBeam prototype, the work in [65] has experimentally demonstrated distributed beamforming in an air-to-ground channel with the clocking solution achieved via an OctoClock cable that was connected to UAVs. In [74], tilted antennas were proposed to form beams in certain directions. Event-triggered DTBF has been proposed in [75] as a solution to reduce the overhead of channel estimation and feedback. A model-free DTBF system has been simulated and studied in [76]. An adaptive positioning algorithm for the distributed Tx nodes, which required feedback from the receiver nodes, was proposed in [77] to improve beamforming performance. Other works, such as [78], have analytically investigated the impact of phase offset between the distributed nodes on beamforming gains. The work in [79] has studied the minimization of probability of outage in a drone-based data collection system with distributed beamforming from the sensor nodes. Moreover, governments have started focusing on DTBF in drone swarms. For example, the U.S. Air Force is currently looking at the automation of a drone swarm for distributed beamforming [80].

Many of the above mentioned works have produced algorithms and system design considerations that help in understanding and solving some problems related to DTBF systems. However, none of these works have considered leveraging the heterogeneous structure of the UAV by rotation at the receiver to offset the negative impact of the phase errors at the distributed transmitter side. With short coherence times and the continuous hovering/moving state of UAVs, channel estimation and feedback as a method of attempting to improve the received signal at the receive UAV, is computationally expensive. In addition, due to the short coherence times, it is highly likely that the obtained channel state information (CSI) will be outdated. Therefore, a local receiver method in which the channel can be improved

is highly desirable. Such a method will result in *significant reduction in channel feedback overhead* and more autonomy at the beamformee side. Hence, works that investigate the potential for such a UAV-based receiver method are necessary.

5.1.1 Contributions

In this chapter, we investigate how the UAV body and its rotation can improve the beamforming gain for various antenna positions. To this end, we conduct various controlled experiments at 2.48 GHz (IEE 802.11 Channel 14) that span different drone rotation angles, induced phase offset values at two distributed Tx nodes, and four antenna positions at the receiver UAV. We quantify what we term *rotational gain* and show that regardless of the antenna placement, the UAV's heterogeneous body structure can be used to increase the level of the beamformed Rx signal simply by rotating the receiver drone relative to the transmitters. Additionally, we show that as the different phase offsets between Tx nodes change, the optimal rotational angle for a given antenna position changes as well. Lastly, we explore the trade-offs of this rotation strategy, specifically that rotation angles that result in the strongest possible Rx signal do not always have the highest average Rx signal, depending on the distribution of the phase offset between the two transmitters.

We first start with the system model, then, we discuss the above-mentioned two sources of phase error. The experiments that characterize the UAV body effect on phase coherency are then presented, followed by conclusions and future work.

5.2 System Model

We will now present the model for a DTBF system, including the previously mentioned sources of error. Let mission drone i be at a distance of $d = d_o + d_{err}$ from the anchor drone (see Fig. 5.1). Here, d_o is the nominal distance and d_{err} is the error in distance resulting from location error due to hovering movement. If the anchor drone broadcasts a message signal $m(t)\cos(2\pi f_c t)$ to all mission drones, then, mission drone i will receive [68]:

$$r_i(t) = w_i m(t)\cos(2\pi f_c t + \phi_o(i) + \phi_{er}(i)) + n_i(t) \tag{5.1}$$

Here, w_i is the complex channel fading coefficient, $\phi_o(i) = \frac{2\pi d_o(i)}{\lambda}$ is the nominal phase

offset from the transmit carrier signal, and $\phi_{er}(i) = \frac{2\pi d_{err}(i)}{\lambda}$ is the phase error due to location error. Mission node i then demodulates the received signal by the carrier $\cos(2\pi(fc+\delta f_i)t+\phi_{lo}(i))$, where δf is the CFO between the anchor and mission drone, and $\phi_{lo}(i)$ is an arbitrary phase offset value created by its own LO. The complex baseband signal at mission node i will be:

$$r_i(t) = m(t)w_i e^{j(2\pi\delta f_i t+\gamma_i)} \tag{5.2}$$

where $\gamma_i = \phi_o(i) + \phi_{er}(i) + \phi_{lo}(i)$. The mission drones can estimate the channel $\hat{w}_i$ and use that estimate to beamform the common message signal $x(t)$ in the direction of the anchor drone using conjugate-based beamforming. That is, each node uses $\hat{w_i^*}$ multiplied by the message signal and modulated by the carrier. Hence, the transmitted signal from mission drone i is [81]:

$$q_i(t) = \Re(\hat{w_i^*}s(t-\tau_{syn}(i))e^{j(2\pi(f_c+\delta f_i)t-\tau_{syn}(i)-\gamma_i)} \tag{5.3}$$

Here, $s(t) = \sum_k p(t-kT)x_k$, where x_k is the stream of sent symbols, and $p(t)$ is the transmitted pulse with power p_s. We assume a narrow band fading model and henceforth disregard inter-symbol interference. The received baseband signal as a result of transmitting from N drones is: $r_k = \boldsymbol{w^H}\hat{\boldsymbol{w}}^* x_k + n_k$. Then, the received, beamformed power at the receiver (anchor UAV) will be:

$$P_r = ||\sum_{i=1}^{N} w_i e^{-j\Theta_i}||^2 \tag{5.4}$$

Here, we collect all phase error terms in Θ_i, *i.e.,* $\Theta_i = \phi_{er}(i) + \phi_{lo}(i) + \phi_o(i)$. We will first analyze experimental results pertaining to the two phase errors (LO phase offset and drone hovering position movement). Then, through controlled experiments, we will show how to combat the negative effects of these errors via local decisions by the UAV in the form of rotation and antenna selection.

5.3 Sources of Phase Error and Their Impact on Distributed Transmit Beamforming Gains

Here, we provide an experimental insight about the behavior and severity of phase errors caused by distributed LOs and UAV hovering position movement. Then, we discuss their joint impact on beamforming gains via a simulation example.

5.3.1 Phase Errors in Centralized and Distributed SDR Systems

To understand the behavior of phase offset between different radios, we conduct multiple experiments and measure the phase offset between daughterboards of the same SDR (centralized) and two spatially-distributed SDRs. The SDR explored in this study is the USRP N310 which is composed of two Analog Devices daughterboards. We leverage our facility, MuDDI (Multi-dimensional Drone Communications Infrastructure), to conduct the experiments. MuDDI is a distributed massive MIMO testbed for drone experimentation and it constitutes 72 distributed antennas/dedicated RF chains for 18 USRP N310s. We refer the reader to [82] for details about the facility and its architecture. The phase offset between two RF chains is calculated by unwrapping the phase of each received signal's phase and finding the difference. This difference is then analyzed over time and across different USRP daughterboards.

After conducting more than fifty experiments, we conclude the following:

(1) Over time, when no phase drifts occur, the phase offset follows a Normal distribution. Figs. 5.2(a) and 5.2(b) show the phase offset over time and its histogram of an experiment which lasted for about three minutes. The normal distribution result is true for many tested time durations (1 s, 16 s, 160 s, and 300 s). We can also see that the offset is stable over time and its standard deviation is small (0.022 rad).

(2) Phase drifts occur frequently when phase offset is measured across distributed USRPs. When the phase offset drifts, its distribution will be characterized by multiple normal distributions with their mean being uniformly distributed. An example of this drift, which causes a jump in the phase difference between the signals, is shown in Figs. 5.2(c) and 5.2(d). About 40% of the conducted experiments with different and spatially distributed SDRs exhibit phase drifts. In a distributed UAV swarm, each UAV radio will likely experience a different phase noise and temperature, consequently experiencing drifts and/or phase jumps relative to the other radios.

5.3.2 Position Error in Hovering UAVs

There are two modes of error in the positioning of a hovering UAV. The first is an absolute deviation from the intended location due to errors in GPS coordinates or a lack of

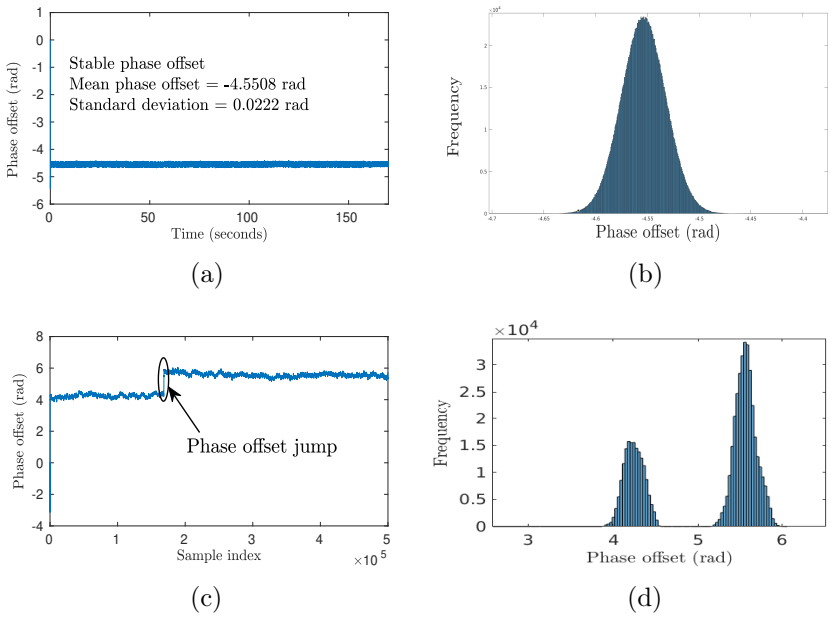

Figure 5.2: (a) and (b) show phase offset between two boards within the same USRP while (c) and (d) show phase offset between two distributed USRPs.

precision in the flight control software. The second is random fluctuations in the position of the UAV, both small (*e.g.*, flight vibrations) and large (*e.g.*, wind). Both of these errors can be mitigated by improved GPS sensing and flight control systems, but will always exist to some degree. With this in mind, we have measured the positioning error in hovering UAVs as part of several in-field measurement campaigns in [83].

Specifically, we have measured d_{err}, which is defined as the deviation (in meters) from the intended hovering position, for more than a hundred flying locations. Refer to [83] for details regarding the experimental setup. The measured error for a fixed hovering period of 7 minutes for one trial is shown in Fig. 5.3(a). There is an offset of approximately 30 cm, around which the error changes rapidly. Fig. 5.3(b) shows violin plots for eight different trials of the same fixed hovering location. The shape of each violin represents an estimation of the distribution of the instantaneous measurements using kernel density estimation. The true mean of the measurements is shown by the black lines. In our experiments, the maximum instantaneous position error for this fixed, hovering UAV was 1 m across all trials. Together, these figures show that the displacement error can change over time and that its distribution

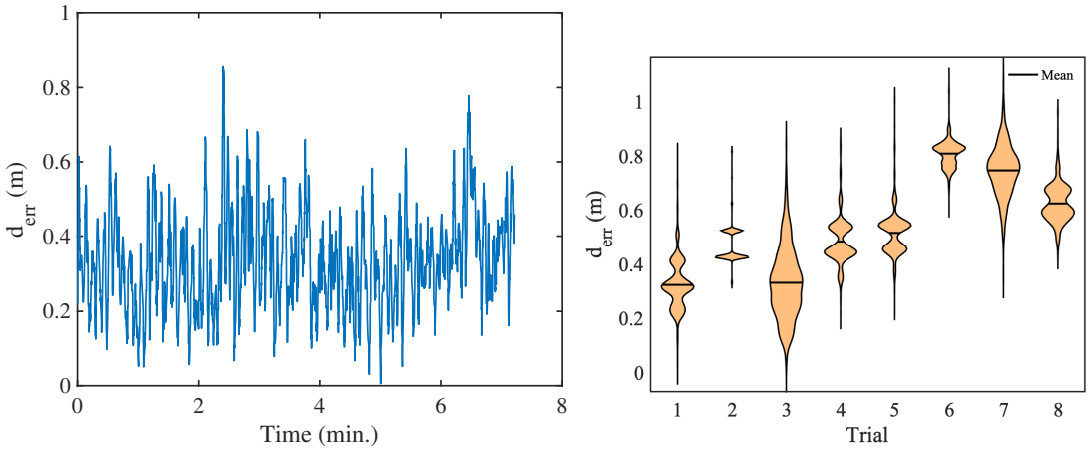

(a) (b)

Figure 5.3: (a) Instantaneous position error for a single hovering UAV. (b) Violin plots showing the estimated distributions of position error for repeated trials of a fixed UAV hovering location.

is unlikely to be a uniform one, which is the assumption made in many related works, such as [81]. The nature of the distribution of the hovering movement varies from flight to flight and depends on many factors, including the environmental conditions and the performance of the flight control system. This situational variation is unique to UAV-based DTBF. The severity of the impact of this placement error on the phase of the arriving/departing wave depends on its carrier frequency. Low frequencies (*i.e.*, large wavelengths) have looser constraints on this placement error compared to high frequencies.

5.3.3 Impact of LO and Hovering Phase Errors on DTBF Gains

In this section, using (5.4), we simulate the impact of the above discussed sources of phase errors on beamforming gain in a 2×1 distributed beamforming system. Note that the UAV body and its rotation impact is not considered. The purpose is to motivate receiver-based strategies to counteract the impact of phase incoherence from the transmitters and potentially reduce the overhead needed for channel estimation and feedback. Let us assume that the two channel fading coefficients have the same unit magnitude, *i.e.*, $w_1 = w_2 = 1$. Also, let the time synchronization error be negligibly small compared to the message time duration. Lastly, we can assume that CFO is the same across the nodes or has been accounted

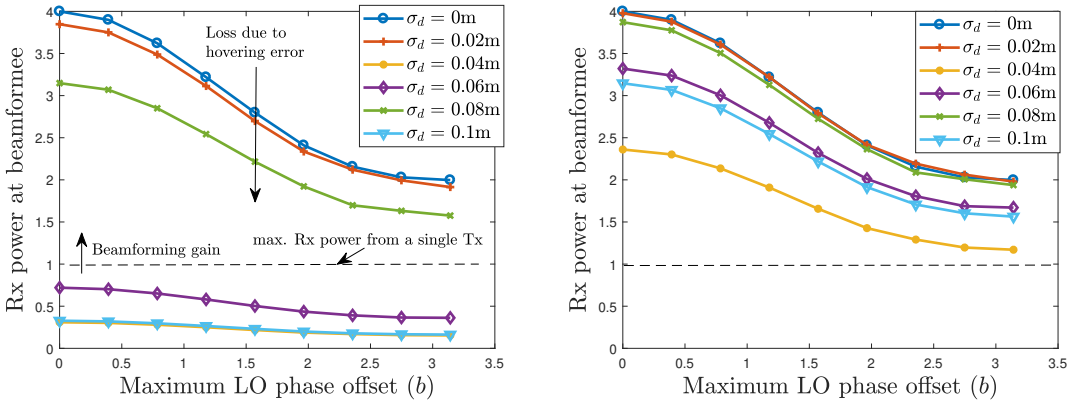

(a) (b)

Figure 5.4: The joint impact of UAV position and LO phase errors on beamforming for a 2×1 DTBF system at (a) 2.4 GHz ($\lambda = 12.5$ cm) and (b) 900 MHz ($\lambda = 33.3$ cm).

for. With these assumptions, we focus solely on the two sources of phase errors and their impact on beamforming gain.

The LO phase offset is assumed to be uniformly distributed in a range of $2b$, *i.e.* $\phi_{lo} \sim \mathcal{U}[-b, +b]$, where b changes from 0 to π in $\frac{\pi}{8}$ intervals. For the sake of simplicity, let us assume that the UAV hovering error is normally-distributed with some intended mean, which is zero in the following analysis, and a standard deviation of σ_d. For each hovering error standard deviation, we generate 1-by-N normally distributed random variables representing hovering errors, which is d_{err}. The values of these random variables are then translated to phase errors and then added to another 1-by-N uniformly distributed random variables, representing the LO phase offsets. The received power is averaged over 1000 trials of different random instances per hovering and LO phase errors.

The results of the mean received power for two carrier frequencies 2.4 GHz and 900 MHz are plotted in Fig. 5.4. Let us first inspect the 2.4 GHz results (Fig. 5.4(a)). If we look at the case of no hovering error (*i.e.*, $\sigma_d = 0$ m) we can see that the result follows intuition. That is, as the amount of b increases, beamforming gain decreases. Beamforming gain is the amount of increase in received power as a result of beamforming compared to the single Tx case (dashed line in the figure). For any hovering error standard deviation, the increase in LO phase offset would result in a reduction in the received power level. If we now look at

the case of zero LO phase offset, we can observe that the received power could dramatically change according to the hovering error standard deviation. For example, while we can reach an almost ideal beamforming gain level ($N^2 = 2^2 = 4$) at a $\sigma_d = 0.02$ m with received power levels of 3.84 (96.2% of ideal gain), the beamformed power could drop to 3.15 (about 78% of the ideal beamforming gain), as the error standard deviation increases to 0.08 m. At $\sigma_d = 0.1$ m, destructive interference results in received power levels that are below the beamforming gain threshold (dashed line in the figures), rendering beamforming useless. This discrepancy in beamformed power at various combined phase error values demonstrates how crucial the position error of the UAV can be on beamformed power.

To show the impact of frequency choice on the sensitivity of beamforming gains to hovering and LO phase errors, we compare the obtained results at 2.4 GHz to those at 900 MHz (Fig. 5.4(b)). This comparison is performed for the same simulation run (*i.e.,* same randomly-generated numbers). We can see that the 900 MHz system can tolerate hovering error standard deviations of up to 10 cm. This result is evident by how all the received power levels are above the beamforming gain threshold. This result is a direct consequence of the approximately 2.7 times longer wavelength at 900 MHz compared to 2.4 GHz. It is worth mentioning that the impact of phase error on DTBF has been studied in many works before, such as [69, 73, 76, 81]. However, these studies either did not consider the potential impact of hovering errors or simply assumed a uniform or normal distribution for phase offsets without a measurement-based justification.

5.4 Improving Beamforming Gain Through UAV Body Rotation: Experimental Results

Here, we investigate how UAV rotation can help counteract the impact of phase offsets experienced by the distributed transmit nodes. Four different antenna positions on the UAV body are analyzed to further emphasize its role.

5.4.1 Experimental Setup

We use two USRP E312s for the experiments: one USRP, which acts as the transmitter is connected to two spatially-distributed Tx antennas that are 10 inches apart; while the other USRP is mounted on the drone body and connected to four antennas. The Rx drone is

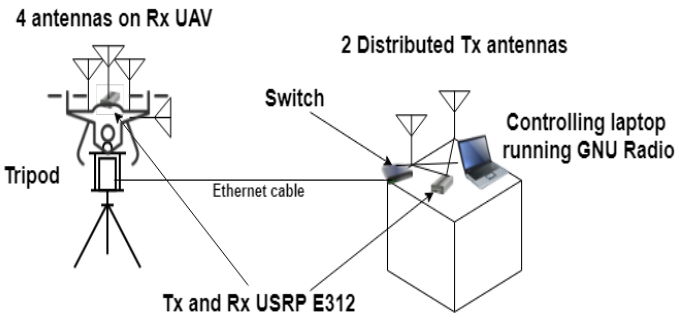

(a)

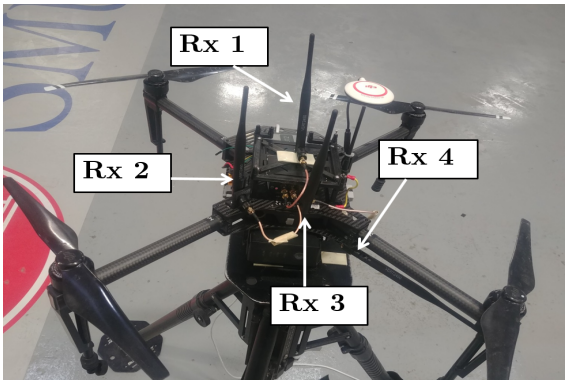

(b)

Figure 5.5: (a) Experiment setup illustration. (b) The four UAV-mounted antennas.

attached to a tripod which is adjusted to approximately the same height of the distributed transmit antennas. Fig. 5.5(a) illustrates the experiment setup, and Fig. 5.5(b) shows the Rx UAV with the four antenna positions.

GNU Radio is used to create a flow graph that does the following: creates two sinusoids $m_1(t)$ and $m_2(t)$; $m_2(t) = e^{j\phi_{ind}} m_1(t)$ where ϕ_{ind} is the artificially-induced and controlled phase offset, which we use to emulate a real distributed system that exhibits such offset. The message signal is used to modulate a carrier at a frequency of 2.48 GHz (channel 14 in IEEE 802.11), which is transmitted using two identical VERT2450 omnidirectional dipole antennas. With the same antenna types at the receiver, the four Rx antennas receive the transmitted signal in two turns: first, Rx1 and Rx2, then Rx3 and Rx4. Measurements are taken in turns because USRP E312 is limited to two receive RF chains. The process is automated and controlled via GNU Radio. The collection of measurements lasts for 3 seconds per Rx combination. The induced phase offset values are done in $\pi/9$ intervals and span $-\pi$ to $+\pi$.

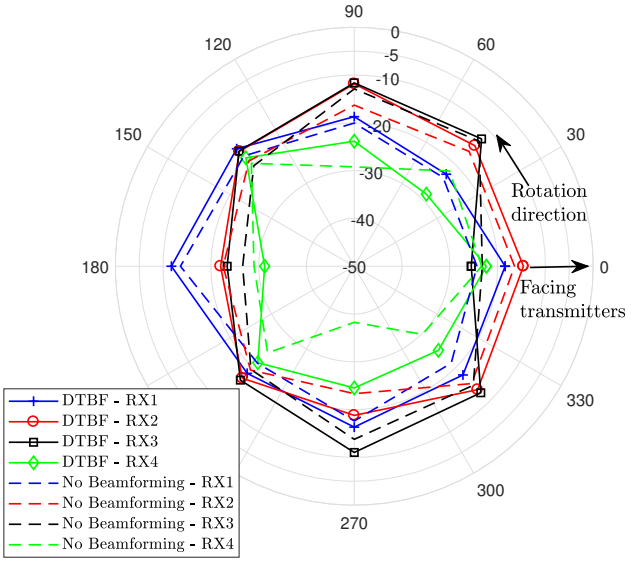

Figure 5.6: Measured receive power at the four UAV-mounted receive antennas across all rotation angles and 0° induced phase offset. Solid lines indicate Rx power when DTBF and dashed lines indicate no beamforming.

For comparison, a measurement is also taken for a transmission from a single antenna (no beamforming). For each induced phase offset, the drone is rotated in 45° increments from 0° to 360°.

5.4.2 Results

The results of the received power at the four UAV-mounted receive antennas for a fixed induced phase offset of 0° and for both, beamforming and non-beamforming scenarios, are given in Fig. 5.6. We make the following observations:

5.4.2.1 UAV Rotation gain

For a fixed antenna position, rotation of the drone can result in an increase in received power. This rotation gain can offset the decrease in beamforming gains that might be experienced due to phase offset at the distributed Tx nodes. This rotation gain, compared to 0° (no rotation), can reach up to 6.6 dB for Rx1, 7.4 dB for Rx2, 14.5 dB for Rx3, and 13.9 dB for Rx4. This result shows that by performing local, Rx-based rotation, the received signal power could be significantly improved, and the reductions experienced by phase offsets

Table 5.1: Rotation Gain Standard Deviation (in dB)

Rx Antenna	**Standard Deviation**
Rx 1	2.980
Rx 2	3.060
Rx 3	6.060
Rx 4	3.940

at the Tx side could be alleviated. We can also observe that, for a fixed rotational angle and an induced phase offset, different antenna positions can provide substantial improvements in received power levels (Fig. 5.6). For example, at 90° rotation, the received power at Rx3 is about 7 dB stronger than that of Rx1. At 45°, the beamformed signal power is 7.5 dB stronger at Rx2 than that of Rx1. Lastly, and due to polarization mismatch, the horizontal Rx antenna (Rx4 in Fig. 5.6) is performing the worst in most cases, regardless of whether DTBF is performed or not. The standard deviation of this rotation gain at 0°-induced phase offset for the four antennas is summarized in Table 5.1. We can see from the table that UAV rotation indeed results in variations in the beamformed power level with the least standard deviation belonging to Rx1 (antenna mounted on top of the UAV), and the maximum standard deviation belonging to Rx4, which is the horizontal antenna attached to the leg of the drone.

5.4.2.2 Joint impact of phase offset and drone rotation

In the previous discussion, we fixed the induced phase offset between the distributed Tx nodes and investigated how drone rotation and antenna position affect the beamformed receive power. Here, we analyze how beamforming can be influenced by the joint variation in phase offset and drone rotation. To do so, we visually inspect Fig. 5.7, where the beamformed receive power for the three vertical antennas at all induced phase offsets and rotation angles is plotted. First, we see that the beamformed signal power changes not only with rotation but also with the (controlled) induced phase offset for a fixed rotation angle. Second, we see that the antenna mounted on top of the drone body (Rx1) exhibits one peak concentrated around 0° phase offset around 180° rotation (Fig. 5.7(c)), while the other two vertical antennas (Rx2

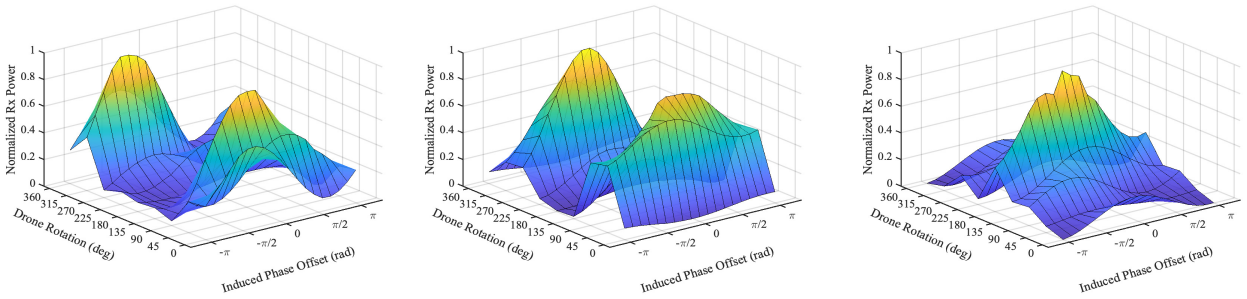

(a) (b) (c)

Figure 5.7: Received power in a DTBF system for three antennas at different rotation and induced phase-offset angles. Values are normalized to the maximum received power across all antennas measurements. (a) Vertical antenna mounted to the left (Rx2), (b) Vertical antenna mounted in the middle (Rx3), and (c) Vertical antenna mounted at the top of the drone body (Rx1).

and Rx3) exhibit two peaks that alternate depending on the UAV rotation angle (Figs. 5.7(a) and 5.7(b)).

5.4.2.3 Trade-offs in Rotational Gain

Rotation is found to also alter the statistics of the beamformed signal power across different induced phase offsets. For example, in Fig. 5.7(b) while at 45°, the average of the received signal's power across all phase offsets is higher than the average received power at 270°, the maximum power at 270° is higher (around 0.8) than that at 45°, which is only 0.6. The minimum received signal power at 45° is around 0.4, while at 270°, it is 0.1 – a significant reduction solely due to the change in UAV rotation angle and the resultant local reflection/scattering. Depending on the required performance (higher average and lower minimum vs. higher maximum value for example) intelligent rotation by the UAV can be designed according to these needs.

Fig. 5.8 depicts a cross-section of the surface plot of Rx power for the antenna mounted in the middle of the front of the drone (Rx3). This cross-section shows the Rx power as a function of the phase offset, parameterized by the drone rotation angle. This figure makes the trade-off between rotation angles clear. To experience the highest possible Rx power, the receiver drone should rotate to an angle of 270°. However, in achieving a high peak power, the receiver sacrifices stability–the Rx power is much more sensitive to changes in the net

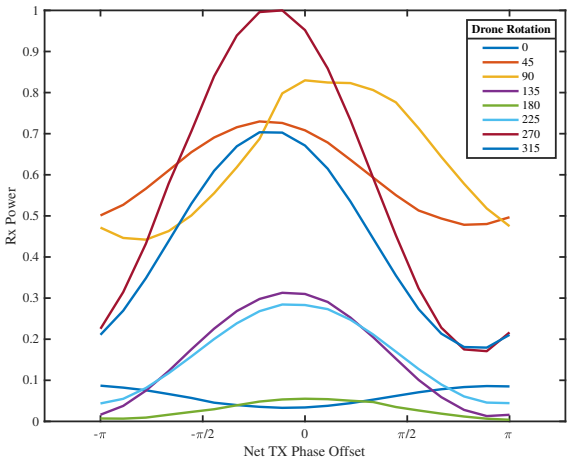

Figure 5.8: Cross-section for the received power by Rx3.

phase offset of the system. On the other hand, if the receiver wishes to maximize the lowest possible Rx power, it should rotate to 45°, but in doing so, it sacrifices peak power. These statistical trade-offs are summarized in Table 5.2. Per column, maximums/minimums are written in **bold**/*italics*, respectively.

Lastly, it is worth noting that the rotation impact can change according to the distributed transmitters topology. For instance, if the transmitters are spatially distributed in a way that spans more than one side of the UAV, then, rotation might be more beneficial to certain transmitters than others. An interesting issue arises where the optimal topology of distributed transmitters can change according to the relative UAV direction. We leave this problem for future work.

Table 5.2: Rx Power Statistics per Drone Rotation

Rotation	**Max**	**Min**	**Mean**
0	0.087	0.033	0.061
45	0.730	**0.478**	0.597
90	0.830	0.442	**0.630**
135	0.313	0.013	0.156
180	*0.055*	*0.004*	*0.029*
225	0.284	0.044	0.158
270	**1.000**	0.171	0.565
315	0.703	0.180	0.429
360	0.087	0.033	0.061

Chapter 6

Conclusions and Future Work

In this work, we showed that the UAV body can affect the radiation pattern of its mounted antennas and act as a local source of scattering altering the polarization of the arriving/departing electromagnetic wave. Significant reductions in the cross-polarization discrimination (XPD) are measured solely due to the UAV body. As a result, UAVs in a swarm could potentially seek optimizing their heading direction and antenna selection decisions based on our findings.

We also investigated how the human body affects UAV-to-ground channels for various drone hovering positions, frequencies, and use cases. We quantified and analyzed the user's impact on the channel, and demonstrated that as a result of the quantified body-induced effects, the optimal UAV hovering position is significantly different from theoretical models that excludes the human-induced effects on the channel.

Finally, we demonstrated that by leveraging the heterogeneous structure of the UAV body, rotation can provide significant improvements in the level of beamformed signal power when transmit nodes are performing distributed beamforming. We also showed that there exists an optimal combination of a UAV rotation angle and an antenna position that yield highest beamforming gains.

The latter findings are true for a scenario where the distributed transmitters exist at one side of the UAV. However, when the distributed transmitters are at geographically different locations that span different sides of the UAV, body rotation, we hypothesise, could be optimal for only a subset of the transmitters. Therefore, the effectiveness of this rotation-based method when distributed transmit UAVs exists in 3D space that span all sides of the receiver UAV is still an open question.

Bibliography

[1] D. Martin, V. Singh, M. A. Latheef, and M. Bagavathiannan, "Spray deposition on weeds (palmer amaranth and morningglory) from a remotely piloted aerial application system and backpack sprayer," *Drones*, vol. 4, 2020. 1

[2] K. Montgomery, J. B. Henry, M. C. Vann, B. E. Whipker, A. S. Huseth, and H. Mitasova, "Measures of canopy structure from low-cost uas for monitoring crop nutrient status," *Drones*, vol. 4, 2020. 1

[3] "{NIH} Delivery of Automated External Defibrillators via Drones in Simulated Cardiac Arrest: Users' Experiences and the Human-Drone Interaction {} -," https://www.ncbi.nlm.nih.gov/pmc/articles/PMC7769863/. 1

[4] A. Al-Hourani and K. Gomez, "Modeling Cellular-to-UAV Path-Loss for Suburban Environments," *IEEE Wireless Communications Letters*, vol. 7, no. 1, pp. 82–85, Feb. 2018. [Online]. Available: http://ieeexplore.ieee.org/document/8048502/ 3, 14, 15, 22, 31, 39

[5] Z. Cui, C. Briso-Rodriguez, K. Guan, C. Calvo-Ramirez, B. Ai, and Z. Zhong, "Measurement-Based Modeling and Analysis of UAV Air-Ground Channels at 1 and 4 GHz," *IEEE Antennas and Wireless Propagation Letters*, vol. 18, no. 9, pp. 1804–1808, Sep. 2019. [Online]. Available: https://ieeexplore.ieee.org/document/8770066/ 3, 56

[6] E. Yanmaz, R. Kuschnig, and C. Bettstetter, "Achieving air-ground communications in 802.11 networks with three-dimensional aerial mobility," in *2013 Proceedings IEEE INFOCOM*. Turin, Italy: IEEE, Apr. 2013, pp. 120–124. [Online]. Available: http://ieeexplore.ieee.org/document/6566747/ 3, 21, 22, 31, 43

[7] P. A. Catherwood, B. Black, E. Bedeer Mohamed, A. A. Cheema, J. Rafferty, and J. A. D. Mclaughlin, "Radio Channel Characterization of Mid-Band 5G Service Delivery for Ultra-Low Altitude Aerial Base Stations," *IEEE Access*, vol. 7, pp. 8283–8299, 2019. [Online]. Available: https://ieeexplore.ieee.org/document/8606910/ 3, 21, 22, 51, 56

[8] C. Balanis, *Antenna Theory: Analysis and Design*, 4th ed. Wiley, 2016. 6, 7, 8, 14, 69

[9] "VERT2456 antenna radiation pattern datasheet and anechoic chamber results = https://smu.box.com/s/wnmq2xf8fiefd5pwse88w60an8vy7jmm, note = ." 6, 7

[10] M. Shafi, Min Zhang, A. Moustakas, P. Smith, A. Molisch, F. Tufvesson, and S. Simon, "Polarized MIMO channels in 3-D: models, measurements and mutual information," *IEEE Journal on Selected Areas in Communications*, vol. 24, no. 3, pp. 514–527, Mar. 2006. [Online]. Available: http://ieeexplore.ieee.org/document/1603707/ 8, 26, 27

[11] M. Badi, J. Wensowitch, D. Rajan, and J. Camp, "Experimental Evaluation of Antenna Polarization and Elevation Effects on Drone Communications," in *Proc. of ACM MSWiM*, 2019. 8, 26, 27, 38

[12] A. Goldsmith, *Wireless Communications*, 2005. 9, 10, 12, 13, 38, 39

[13] M. Simunek, F. P. Fontan, and P. Pechac, "The UAV Low Elevation Propagation Channel in Urban Areas: Statistical Analysis and Time-Series Generator," *IEEE Transactions on Antennas and Propagation*, vol. 61, no. 7, pp. 3850–3858, Jul. 2013. [Online]. Available: http://ieeexplore.ieee.org/document/6492100/ 14, 15, 73

[14] F. Jiang and A. L. Swindlehurst, "Optimization of UAV Heading for the Ground-to-Air Uplink," *IEEE Journal on Selected Areas in Communications*, vol. 30, no. 5, pp. 993–1005, Jun. 2012. [Online]. Available: http://ieeexplore.ieee.org/document/6214709/ 21

[15] M. Mozaffari, W. Saad, M. Bennis, and M. Debbah, "Drone-Based Antenna Array for Service Time Minimization in Wireless Networks," in *2018 IEEE International*

Conference on Communications (ICC). Kansas City, MO: IEEE, May 2018, pp. 1–6. [Online]. Available: https://ieeexplore.ieee.org/document/8422374/ 21

[16] Q. Wu, J. Xu, and R. Zhang, "Capacity Characterization of UAV-Enabled Two-User Broadcast Channel," *IEEE Journal on Selected Areas in Communications*, vol. 36, no. 9, pp. 1955–1971, Sep. 2018. [Online]. Available: https://ieeexplore.ieee.org/document/8432474/ 21, 57

[17] W. Khawaja, O. Ozdemir, and I. Guvenc, "UAV Air-to-Ground Channel Characterization for mmWave Systems," *arXiv:1707.04621 [cs, math]*, Oct. 2017, arXiv: 1707.04621. [Online]. Available: http://arxiv.org/abs/1707.04621 21, 56

[18] W. Khawaja, I. Guvenc, and D. Matolak, "UWB Channel Sounding and Modeling for UAV Air-to-Ground Propagation Channels," in *2016 IEEE Global Communications Conference (GLOBECOM)*. Washington, DC, USA: IEEE, Dec. 2016, pp. 1–7. [Online]. Available: http://ieeexplore.ieee.org/document/7842372/ 21, 43

[19] E. Yanmaz, S. Hayat, J. Scherer, and C. Bettstetter, "Experimental performance analysis of two-hop aerial 802.11 networks," in *2014 IEEE Wireless Communications and Networking Conference (WCNC)*. Istanbul, Turkey: IEEE, Apr. 2014, pp. 3118–3123. [Online]. Available: http://ieeexplore.ieee.org/document/6953010/ 21, 22

[20] T. J. Willink, C. C. Squires, G. W. K. Colman, and M. T. Muccio, "Measurement and Characterization of Low-Altitude Air-to-Ground MIMO Channels," *IEEE Transactions on Vehicular Technology*, vol. 65, no. 4, pp. 2637–2648, Apr. 2016. [Online]. Available: http://ieeexplore.ieee.org/document/7079507/ 21

[21] Y. Shi, R. Enami, J. Wensowitch, and J. Camp, "Measurement-based characterization of los and nlos drone-to-ground channels," in *Proc. of IEEE WCNC*, 2018. 21, 56

[22] Z. Cui, C. Briso-Rodriguez, K. Guan, Z. Zhong, and F. Quitin, "Multi-Frequency Air-to-Ground Channel Measurements and Analysis for UAV Communication Systems," *IEEE Access*, vol. 8, pp. 110 565–110 574, 2020. [Online]. Available: https://ieeexplore.ieee.org/document/9107106/ 21, 56

[23] K. Morioka, J. Naganawa, N. Kanada, S. Futatsumori, A. Kohmura, N. Yonemoto, and Y. Sumiya, "5GHz ground-to-air communication link by AeroMACS in high-speed movement scenarios," in *2017 23rd Asia-Pacific Conference on Communications (APCC)*. Perth, WA: IEEE, Dec. 2017, pp. 1–6. [Online]. Available: http://ieeexplore.ieee.org/document/8304031/ 21

[24] H. T. Kung, C.-K. Lin, T.-H. Lin, S. J. Tarsa, and D. Vlah, "Measuring diversity on a low-altitude UAV in a ground-to-air wireless 802.11 mesh network," in *2010 IEEE Globecom Workshops*. Miami, FL, USA: IEEE, Dec. 2010, pp. 1799–1804. [Online]. Available: http://ieeexplore.ieee.org/document/5700251/ 22

[25] P. Laly, D. Gaillot, M. Lienard, J. M. Floch, R. Mazari, P. Degauque, and G. Grunfelder, "Polarimetrie ground-to-ground and ground-to-air channel characterization in forest environment," in *2017 11th European Conference on Antennas and Propagation (EUCAP)*. Paris, France: IEEE, Mar. 2017, pp. 2431–2434. [Online]. Available: http://ieeexplore.ieee.org/document/7928261/ 22

[26] N. Goddemeier and C. Wietfeld, "Investigation of Air-to-Air Channel Characteristics and a UAV Specific Extension to the Rice Model," in *2015 IEEE Globecom Workshops (GC Wkshps)*. San Diego, CA, USA: IEEE, Dec. 2015, pp. 1–5. [Online]. Available: http://ieeexplore.ieee.org/document/7414180/ 22, 39, 49, 72

[27] J. Rodriguez-Pineiro, T. Dominguez-Bolano, X. Cai, Z. Huang, and X. Yin, "Air-to-Ground Channel Characterization for Low-Height UAVs in Realistic Network Deployments," *IEEE Transactions on Antennas and Propagation*, vol. 69, no. 2, pp. 992–1006, Feb. 2021. [Online]. Available: https://ieeexplore.ieee.org/document/9170768/ 22, 56, 62, 73

[28] S.-C. Kwon and G. L. Stuber, "Geometrical Theory of Channel Depolarization," *IEEE Transactions on Vehicular Technology*, vol. 60, no. 8, pp. 3542–3556, Oct. 2011. [Online]. Available: http://ieeexplore.ieee.org/document/5962379/ 26

[29] W. Xu, X. Wu, X. Dong, H. Zhang, and X. You, "Dual-Polarized Massive MIMO Systems Under Multi-Cell Pilot Contamination," *IEEE Access*, vol. 4, pp. 5998–6013, 2016. [Online]. Available: http://ieeexplore.ieee.org/document/7572891/ 26

[30] Y. Xing, O. Kanhere, S. Ju, T. S. Rappaport, and G. R. MacCartney, "Verification and Calibration of Antenna Cross-Polarization Discrimination and Penetration Loss for Millimeter Wave Communications," in *2018 IEEE 88th Vehicular Technology Conference (VTC-Fall)*. Chicago, IL, USA: IEEE, Aug. 2018, pp. 1–6. [Online]. Available: https://ieeexplore.ieee.org/document/8690683/ 26, 27

[31] T. Neubauer and P. Eggers, "Simultaneous characterization of polarization matrix components in pico cells," in *Gateway to 21st Century Communications Village. VTC 1999-Fall. IEEE VTS 50th Vehicular Technology Conference (Cat. No.99CH36324)*, vol. 3. Amsterdam, Netherlands: IEEE, 1999, pp. 1361–1365. [Online]. Available: http://ieeexplore.ieee.org/document/801485/ 26

[32] J. S.-C. A. Umeyama and C. Fulton, "Uav-based antenna measurements for polarimetric weather radars: Probe analysis," *IEEE Access*, Nov. 2020. 26

[33] J. F. Valenzuela-valdes, M. A. Garcia-fernandez, A. M. Martinez-gonzalez, and D. Sanchez-Hernandez, "The Role of Polarization Diversity for MIMO Systems Under Rayleigh-Fading Environments," *IEEE Antennas and Wireless Propagation Letters*, vol. 5, pp. 534–536, 2006. [Online]. Available: https://ieeexplore.ieee.org/document/4052593/ 26

[34] Yuan Yao, Jianfeng Zheng, and Zhenghe Feng, "Diversity Measurements for On-Body Channels Using a Tri-Polarization Antenna at 2.45 GHz," *IEEE Antennas and Wireless Propagation Letters*, vol. 11, pp. 1285–1288, 2012. [Online]. Available: http://ieeexplore.ieee.org/document/6341038/ 26, 28, 32

[35] I. G. L. R. Grünblatt and O. Simonin, "Leveraging Antenna Orientation to Optimize Network Performance of Fleets of UAVs," in *Proc. of ACM MSWiM*, 2020. 26

[36] S. Baidya, Z. Shaikh, and M. Levorato, "FlyNetSim: An Open Source Synchronized UAV Network Simulator based on ns-3 and Ardupilot," in *Proc. of ACM MSWiM*, 2018. 26

[37] 3GPP, "Telecommunication management; Key Performance Indicators (KPI) for UMTS and GSM," 3rd Generation Partnership Project (3GPP), TS 32.410, Dec. 2015. [Online]. Available: http://www.3gpp.org/ftp/Specs/html-info/32410.htm 28

[38] Jue Wang, Jianing Zhao, and Xiqi Gao, "Modeling and analysis of polarized MIMO channels in 3D propagation environment," in *21st Annual IEEE International Symposium on Personal, Indoor and Mobile Radio Communications*. Istanbul, Turkey: IEEE, Sep. 2010, pp. 319–323. [Online]. Available: http://ieeexplore.ieee.org/document/5671850/ 28

[39] P. Chandhar, D. Danev, and E. G. Larsson, "Massive MIMO as enabler for communications with drone swarms," in *2016 International Conference on Unmanned Aircraft Systems (ICUAS)*. Arlington, VA, USA: IEEE, Jun. 2016, pp. 347–354. [Online]. Available: http://ieeexplore.ieee.org/document/7502655/ 28

[40] R. Gangula, O. Esrafilian, D. Gesbert, C. Roux, F. Kaltenberger, and R. Knopp, "Flying Rebots: First Results on an Autonomous UAV-Based LTE Relay Using Open Airinterface," in *2018 IEEE 19th International Workshop on Signal Processing Advances in Wireless Communications (SPAWC)*. Kalamata: IEEE, Jun. 2018, pp. 1–5. [Online]. Available: https://ieeexplore.ieee.org/document/8445947/ 31, 56

[41] R. Vaughan, "Polarization diversity in mobile communications," *IEEE Transactions on Vehicular Technology*, vol. 39, no. 3, pp. 177–186, Aug. 1990. [Online]. Available: http://ieeexplore.ieee.org/document/130998/ 31

[42] J. Holis and P. Pechac, "Elevation Dependent Shadowing Model for Mobile Communications via High Altitude Platforms in Built-Up Areas," *IEEE Transactions on Antennas and Propagation*, vol. 56, no. 4, pp. 1078–1084, Apr. 2008. [Online]. Available: http://ieeexplore.ieee.org/document/4483593/ 39

[43] Z. Qiu, X. Chu, C. Calvo-Ramirez, C. Briso, and X. Yin, "Low Altitude UAV Air-to-Ground Channel Measurement and Modeling in Semiurban Environments," *Wireless Communications and Mobile Computing*, vol. 2017, pp. 1–11, 2017. [Online]. Available: https://www.hindawi.com/journals/wcmc/2017/1587412/ 49

[44] P. Mattheijssen, M. Herben, G. Dolmans, and L. Leyten, "Antenna-Pattern Diversity Versus Space Diversity for Use at Handhelds," *IEEE Transactions on Vehicular Technology*, vol. 53, no. 4, pp. 1035–1042, Jul. 2004. [Online]. Available: http://ieeexplore.ieee.org/document/1317207/ 50

[45] V. Plicanic, B. K. Lau, A. Derneryd, and Z. Ying, "Actual Diversity Performance of a Multiband Diversity Antenna With Hand and Head Effects," *IEEE Transactions on Antennas and Propagation*, vol. 57, no. 5, pp. 1547–1556, May 2009. [Online]. Available: http://ieeexplore.ieee.org/document/4909459/ 51, 55

[46] Y. Shi, J. Wensowitch, E. Johnson, and J. Camp, "A measurement study of user-induced propagation effects for uhf frequency bands," in *Proc. of IEEE SECON*, 2017. 51, 55, 61, 64

[47] M. Badi, J. Wensowitch, D. Rajan, and J. Camp, "Experimentally analyzing diverse antenna placements and orientations for UAV communications," *IEEE Transactions on Vehicular Technology*, vol. 69, no. 12, pp. 14 989–15 004, May 2020. 51

[48] N. Amani, V. Dehghanian, and J. Nielsen, "User-induced antenna variation and its impact on the performance of RSS-based indoor positioning," in *2016 IEEE Canadian Conference on Electrical and Computer Engineering (CCECE)*. Vancouver, BC, Canada: IEEE, May 2016, pp. 1–5. [Online]. Available: http://ieeexplore.ieee.org/document/7726781/ 51, 55

[49] M. Heino, "Self-user shadowing effects of millimeter-wave mobile phone antennas in a browsing mode," p. 5, 2019. 51, 55, 64, 66

[50] L. Ferranti, L. Bonati, S. D'Oro, and T. Melodia, "SkyCell: A Prototyping Platform for 5G Aerial Base Stations," in *2020 IEEE 21st International Symposium on "A World of*

Wireless, Mobile and Multimedia Networks" (WoWMoM). Cork, Ireland: IEEE, Aug. 2020, pp. 329–334. [Online]. Available: https://ieeexplore.ieee.org/document/9217782/ 52, 56

[51] Chee Wee Kim and T. S. P. See, "RF transmission power loss variation with abdominal tissues thicknesses for ingestible source," in *2011 IEEE 13th International Conference on e-Health Networking, Applications and Services*. Columbia, MO, USA: IEEE, Jun. 2011, pp. 282–287. [Online]. Available: http://ieeexplore.ieee.org/document/6026766/ 54, 55, 64

[52] Y. Ma, Z. Luo, C. Steiger, C. G. Traverso, and F. Adib, "Methods and apparatus for multi-frequency beamforming," Jun. 2020. 54, 55

[53] E. Cabot and M. Capstick, "The Effect of the Human Body on Wireless Microphone Transmission," p. 110. 54, 55, 64

[54] B. Kibret, A. K. Teshome, and D. T. H. Lai, "Characterizing the Human Body as a Monopole Antenna," *IEEE Transactions on Antennas and Propagation*, vol. 63, no. 10, pp. 4384–4392, Oct. 2015. [Online]. Available: http://ieeexplore.ieee.org/document/7160710/ 55

[55] G. Cohn, D. Morris, S. N. Patel, and D. S. Tan, "Your noise is my command: sensing gestures using the body as an antenna," in *Proceedings of the SIGCHI Conference on Human Factors in Computing Systems*. Vancouver BC Canada: ACM, May 2011, pp. 791–800. [Online]. Available: https://dl.acm.org/doi/10.1145/1978942.1979058 55

[56] L. Januszkiewicz, "Analysis of Human Body Shadowing Effect on Wireless Sensor Networks Operating in the 2.4 GHz Band," *Sensors*, vol. 18, no. 10, p. 3412, Oct. 2018. [Online]. Available: http://www.mdpi.com/1424-8220/18/10/3412 55, 65, 66

[57] A. Thielens, R. Benarrouch, S. Wielandt, M. Anderson, A. Moin, A. Cathelin, and J. Rabaey, "A Comparative Study of On-Body Radio-Frequency Links in the 420 MHz–2.4 GHz Range," *Sensors*, vol. 18, no. 12, p. 4165, Nov. 2018. [Online]. Available: http://www.mdpi.com/1424-8220/18/12/4165 55, 66

[58] L. Zhang, Y. Hua, S. L. Cotton, S. K. Yoo, C. R. C. M. Da Silva, and W. G. Scanlon, "An RSS-Based Classification of User Equipment Usage in Indoor Millimeter Wave Wireless Networks Using Machine Learning," *IEEE Access*, vol. 8, pp. 14 928–14 943, 2020. [Online]. Available: https://ieeexplore.ieee.org/document/8957118/ 56, 80

[59] Z. Wang, L. Duan, and R. Zhang, "Adaptive Deployment for UAV-Aided Communication Networks," *IEEE Transactions on Wireless Communications*, vol. 18, no. 9, pp. 4531–4543, Sep. 2019. [Online]. Available: https://ieeexplore.ieee.org/document/8760267/ 57

[60] Y. Ma, N. Selby, and F. Adib, "Drone Relays for Battery-Free Networks," in *Proceedings of the Conference of the ACM Special Interest Group on Data Communication*. Los Angeles CA USA: ACM, Aug. 2017, pp. 335–347. [Online]. Available: https://dl.acm.org/doi/10.1145/3098822.3098847 73

[61] L. Xiao, Y. Xu, D. Yang, and Y. Zeng, "Secrecy energy efficiency maximization for uav-enabled mobile relaying," *Trans. Green Commun. Netw.*, vol. 4, no. 1, Mar. 2020. 79, 80

[62] B. Duo, Q. Wu, X. Yuan, and R. Zhang, "Energy efficiency maximization for full-duplex uav secrecy communication," *IEEE Trans. Veh. Technol.*, vol. 69, no. 4, Apr. 2020. 79, 80

[63] Y. Zhou, C. Pan, P. L. Yeoh, K. Elkashlan, B. Vucetic, and Y. Li, "Secure communications for uav-enabled mobile edge computing systems," *IEEE Trans. Commun.*, vol. 68, no. 1, Jan. 2020. 79, 80

[64] P. K. Gopala, L. Lai, and H. E. Gamal, "On the secrecy capacity of fading channels," *IEEE Trans. Inf. Theory*, vol. 54, no. 10, Oct. 2008. 79

[65] S. Mohanti, C. Bocanegra, J. Meyer, G. Secinti, M. Diddi, H. Singh, and K. Chowdhury, "AirBeam: Experimental Demonstration of Distributed Beamforming by a Swarm of UAVs," in *2019 IEEE 16th International Conference on Mobile Ad Hoc and Sensor*

Systems (MASS). Monterey, CA, USA: IEEE, Nov. 2019, pp. 162–170. [Online]. Available: https://ieeexplore.ieee.org/document/9077393/ 83, 85

[66] R. Mudumbai, G. Barriac, and U. Madhow, "On the Feasibility of Distributed Beamforming in Wireless Networks," *IEEE Transactions on Wireless Communications*, vol. 6, no. 5, pp. 1754–1763, May 2007. [Online]. Available: http://ieeexplore.ieee.org/document/4202181/ 84

[67] H. Ochiai, P. Mitran, H. V. Poor, and V. Tarokh, "Collaborative beamforming for distributed wireless adhoc sensor networks," *IEEE Trans. on Signal Processing.*, vol. 53, pp. 4110–4124, Nov. 2005. [Online]. Available: https://ieeexplore.ieee.org/document/1519680 84

[68] R. Mudumbai, G. Barriac, and U. Madhow, "Distributed beamforming for information transfer in sensor networks," in *Proceedings of the 3rd International Symposium on Information Processing in Sensor Networks*, Apr. 2004. 84, 86

[69] W. Tushar and D. B. Smith, "Distributed transmit beamforming based on a 3-bit feedback system," in *2010 IEEE 11th International Workshop on Signal Processing Advances in Wireless Communications (SPAWC)*. Marrakech, Morocco: IEEE, Jun. 2010, pp. 1–5. [Online]. Available: http://ieeexplore.ieee.org/document/5670903/ 84, 92

[70] A. F. Hanif, H. Tembine, M. Assaad, and D. Zeghlache, "Distributed transmit beamforming with 1-bit feedback for LoS-MISO channels," in *2013 IEEE 14th Workshop on Signal Processing Advances in Wireless Communications (SPAWC)*. Darmstadt, Germany: IEEE, Jun. 2013, pp. 455–459. [Online]. Available: http://ieeexplore.ieee.org/document/6612091/ 85

[71] M. M. Rahman, H. E. Baidoo-Williams, R. Mudumbai, and S. Dasgupta, "Fully wireless implementation of distributed beamforming on a software-defined radio platform," in *2012 ACM/IEEE 11th International Conference on Information Processing in Sensor Networks (IPSN)*. Beijing, China: IEEE, Apr. 2012, pp. 305–315. [Online]. Available: https://ieeexplore.ieee.org/document/6920945/ 85

[72] J. Hou, Z. Lin, W. Xu, and G. Yan, "Distributed Transmit Beamforming with Autonomous and Self-Organizing Mobile Antennas," in *2010 IEEE Global Telecommunications Conference GLOBECOM 2010*. Miami, FL, USA: IEEE, Dec. 2010, pp. 1–5. [Online]. Available: http://ieeexplore.ieee.org/document/5683432/ 85

[73] C. Wang, Q. Yin, J. Zhang, B. Hao, and W. Li, "Distributed Transmit Beamforming without Phase Feedback," *EURASIP Journal on Wireless Communications and Networking*, vol. 2010, no. 1, p. 270894, Dec. 2010. [Online]. Available: https://jwcn-eurasipjournals.springeropen.com/articles/10.1155/2010/270894 85, 92

[74] R. Amer, W. Saad, and N. Marchetti, "Toward a Connected Sky: Performance of Beamforming With Down-Tilted Antennas for Ground and UAV User Co-Existence," *IEEE Communications Letters*, vol. 23, no. 10, pp. 1840–1844, Oct. 2019. [Online]. Available: https://ieeexplore.ieee.org/document/8756296/ 85

[75] D. Kramarev, I. Ahmad, K. Layton, M. Lavenant, H. Soetiyono, G. Lechner, H. Suzuki, I. Grivell, and S. Leak, "Event-Triggered Synchronization for Mobile Distributed Transmit Beamforming," in *MILCOM 2019 - 2019 IEEE Military Communications Conference (MILCOM)*. Norfolk, VA, USA: IEEE, Nov. 2019, pp. 343–348. [Online]. Available: https://ieeexplore.ieee.org/document/9020779/ 85

[76] J. George, C. T. Yilmaz, A. Parayil, and A. Chakrabortty, "A Model-Free Approach to Distributed Transmit Beamforming," in *ICASSP 2020 - 2020 IEEE International Conference on Acoustics, Speech and Signal Processing (ICASSP)*. Barcelona, Spain: IEEE, May 2020, pp. 5170–5174. [Online]. Available: https://ieeexplore.ieee.org/document/9054727/ 85, 92

[77] S. Farazi, K. Chinkidjakarn, and D. R. Brown, "Simultaneous distributed beamforming and nullforming with adaptive positioning," in *IEEE Global Conference on Signal and Information Processing (GlobalSIP)*. IEEE, Dec. 2016, pp. 343–348. [Online]. Available: https://ieeexplore.ieee.org/document/7905817 85

[78] J. Kong, T. F. Dagefu, and B. M. Sadler, "Performance analysis of distributed beamforming with random phase offsets," in *IEEE Wireless Communications*

and Networking Conference (WCNC). IEEE, May 2020. [Online]. Available: https://ieeexplore.ieee.org/abstract/document/9120634 85

[79] T. Feng, L. Xie, J. Yao, and J. Xu, "Outage Probability Minimization for UAV-Enabled Data Collection with Distributed Beamforming," in *2020 IEEE International Conference on Communications Workshops (ICC Workshops)*. Dublin, Ireland: IEEE, Jun. 2020, pp. 1–6. [Online]. Available: https://ieeexplore.ieee.org/document/9145169/ 85

[80] J. Keller, "Air Force looks to Intelligent Automation for tactical beamforming antennas in future swarming drones," May 2019, library Catalog: www.militaryaerospace.com. [Online]. Available: https://www.militaryaerospace.com/unmanned/article/14033583/swarming-drones-antennas-tactical-beamforming 85

[81] R. Mudumbai, D. Brown, U. Madhow, and H. Poor, "Distributed transmit beamforming: challenges and recent progress," *IEEE Communications Magazine*, vol. 47, no. 2, pp. 102–110, Feb. 2009. [Online]. Available: http://ieeexplore.ieee.org/document/4785387/ 87, 90, 92

[82] J. Wensowitch, M. Badi, D. Rajan, and J. Camp, "Building and Simulating Multi-Dimensional Drone Topologies," in *Proc. of ACM MSWiM*, 2020. 88

[83] N. M. Cameron, S. M. Hashir, S. Song, D. Rajan, and J. Camp, "Effect of antenna orientation on the air-to-air channel in arbitrary 3d space," in *3rd IEEE WoWMoM Workshop on Wireless Networking, Planning, and Computing for UAV Swarms*, Jun. 2021. 89